LATE-STAGE TRANSFORMATIONS OF CYCLOPARAPHENYLENES

by

TARA CLAYTON

A dissertation accepted and approved in partial fulfillment of the

requirements for the degree of

Doctor of Philosophy

in Chemistry

Dissertation Committee:

Darren Johnson, Chair

Ramesh Jasti, Advisor

Victoria DeRose, Core Member

Judith Shine, Institutional Representative

University of Oregon

Winter 2025

DISSERTATION ABSTRACT

Tara Danielle Clayton

Doctor of Philosophy in Chemistry

Title: Late-Stage Transformations of Cycloparaphenylenes

Exploring the synthesis and properties of non-planar aromatics is an important endeavor, as technology is often advanced when new structures and materials are realized. The Jasti lab specializes in making cycloparaphenylene (CPP) derivatives, which are highly strained aromatic macrocycles with valuable properties accessible via precise synthetic control. This dissertation focuses on late-stage transformations of CPPs decorated with versatile functional groups. Late-stage transformations allow for efficient synthesis of a wide variety of derivatized CPPs. Herein we focus on utilizing fluorinated and alkyne-containing CPPs to make novel extended structures. Structures of interest include metalated CPPs, redox-active CPPs, novel guest-host CPP-fullerene complexes, and trimeric CPPs. This work applies well-studied reactions that have been investigated on planar aromatics to the growing field of CPP chemistry.

This dissertation includes previously published, unpublished, and coauthored material.

PUBLICATIONS:

A. Kamin, A.; D. Clayton, T.; E. Otteson, C.; M. Gannon, P.; Krajewski, S.; Kaminsky, W.; Jasti, R.; J. Xiao, D. Synthesis and Metalation of Polycatechol Nanohoops Derived from Fluorocycloparaphenylenes. *Chem. Sci.* **2023**, *14* (36), 9724–9732.

Clayton, T. D.; Fehr, J. M.; Price, T. W.; Zakharov, L. N.; Jasti, R. Pinwheel-like Curved Aromatics from the Cyclotrimerization of Strained Alkyne Cycloparaphenylenes. *J. Am. Chem. Soc.* **2024**.

ACKNOWLEDGMENTS

I would like to acknowledge the funding that made this research possible: NSF-CHE-2102567, NSF-CHE-2400147, and NSF CHE-2204123.

I would like to thank Professor Ramesh Jasti for believing in me, mentoring me, and supporting me as I grew into the chemist that I am today. I can think of no better advisor to have done a Ph.D. with. Ramesh encouraged me to ask the research questions that I wanted to answer, and the skills I gained along the way will allow me to ask deeper questions in the future. Ramesh's leadership style fosters a community of self-motivated and creative scientists. It has been an honor to be a part of that community.

The people in the Jasti lab, past and present, are some of the strongest and most positive shaping forces in my life. I was lucky enough to spend a summer as an undergraduate researcher in the Jasti lab in 2018, and that directed the trajectory of my scientific career. Dr. Curtis Colwell was an amazing mentor and role-model, and everyone in the lab at that time motivated me to pursue a Ph.D. To my current lab-mates, I could never thank you all enough for the years of friendship, support, and soul-healing laughter. The Jasti lab hoopsters are some of the coolest people in the world and they shine brighter than my words can convey (opposite to linear counterparts).

To my wonderful Fiancé Colin Hawkinson, I cannot thank you enough for all the love and friendship you have shown me over the ten years I have known you. You have been instrumental in not only helping me get through this Ph.D., but in helping me create a life that I would do anything to protect and nourish. You inspire me and you give me hope.

I would like to thank my family for encouraging me to be my most authentic self and loving me no matter what I decided that was going to look like. I never had to deal with the pressure or stress of feeling like I might let them down if I changed my mind about what I wanted to do,

because they always made it clear that they only wanted me to be happy. Now that this significant chapter of my life is written, I can say I am, truly.

Finally, I would like to thank my incredible friends. I am who I am because of you all. The Great Falls Girls knew me as I was becoming myself, and they loved every version of me the entire time. Some of my most treasured memories are shared with friends I have had since I was very young, and I know we will keep making precious memories until we are very old. The friends I made at Taft, Reed, University of Oregon, and everywhere in between saw me through some of the most challenging, fun, and formative times. The bonds we created in a short time make me feel like we must have found each other previously in another life. You all are the only evidence I need to suggest that I am incredibly lucky in multiple different realities.

DEDICATION

Dedicated in honor of my mom, Crickett Ghee Clayton, who taught me more about love in a short time than I could hope to learn in a lifetime. I find her in every beautiful thing.

TABLE OF CONTENTS

Chapter Page

I. INTRODUCTION…….. 15

1.1 Carbon Nanomaterials and Cycloparaphenylenes (CPPs)……... 15

1.2 Quantum Bits (Qubits)……. 18

1.3 Molecular Qubits…….. 20

1.31 Fullerene and Carbon Nanotube Qubits…….. 22

1.4 Realized/Potential Applications of CPPs in Qubit Architectures…….. 26

1.5 Conclusion…….. 29

1.6 Bridge to Chapter II…… 29

1.7 References…….. 31

II. SYNTHESIS AND METALATION OF POLYCATECHOL NANOHOOPS DERIVED FROM FLUOROCYCLOPARAPHENYLENES…… 36

2.1 Introduction…… 36

2.2 Results and Discussion…….. 38

2.2.1 Alkoxylation and Thiolation of Polyfluorinated Arenes…… 38

2.2.2 Late-Stage Modification of Polyfluorinated [12]CPP…… 40

2.2.3 Coordination Chemistry of Polycatechol CPP Ligands……. 46

2.2.4 DFT Structural Analysis……. 51

2.3 Conclusion……. 52

2.4 Experimental Section……. 53

2.4.1 General Experimental Details……. 53

2.4.2 Synthesis……. 54

2.5 Bridge to Chapter III……. 65

2.6 References……. 66

III. LATE-STAGE SYNTHESIS AND CHARACTERIZATION OF REDOX-ACTIVE THIANTHRENE-CONTAINING CYCLOPARAPHENYLENES…… 70

3.1 Introduction…… 70

3.2 Results and Discussion…….. 74

3.2.1 Synthesis……. 74

3.2.2 X-ray Crystallographic Analysis…… 76

3.2.3 Photophysical Properties…… 77

3.2.4 Binding Studies with Fullerene……. 78

3.2.5 Redox Properties…… 80

3.3 Conclusion…… 80

3.4 Experimental Section…… 81

3.4.1 General Experimental Details……. 81

3.4.2 Synthesis……. 82

3.4.3. X-ray Crystallographic Analysis…… 83

3.4.4. Photophysical Characterization…….. 85

3.4.5. C_{60} Binding Studies……. 86

3.4.7 Computational Details…….. 89

3.5 Bridge to Chapter IV…… 97

3.6 References…… 98

IV. PINWHEEL-LIKE CURVED AROMATICS FROM THE CYCLOTRIMERIZATION OF STRAINED-ALKYNE CYCLOPARAPHENYLENES…… 102

4.1 Introduction…… 102

4.2 Results and Discussion…….. 105

4.2.1 Synthesis……. 105

4.2.2 X-ray Crystallographic Analysis……. 108

4.2.3 StrainViz Analysis…….. 111

4.2.4 Photophysical Analysis…….. 112

4.3 Conclusion……. 116

4.4 Experimental Section…… 117

4.4.1 General Experimental Details……. 117

4.4.2 Synthesis……. 118

4.4.3 Metal screening for cyclotrimerization with fluor[9+1]CPP……. 125

4.4.4. Treatment of diphenylacetylene with $Pd_2(dba)_3$……. 127

4.4.5. Photophysical characterization…….. 129

4.4.6. StrainViz calculations…… 138

4.5 References……. 139

V. CONCLUDING REMARKS……. 144

LIST OF FIGURES

Figure Page

1.1 Cartoon depictions of a fullerene, armchair carbon nanotube, and graphene…… 16

1.2 Cartoons of qubit platforms discussed in this article…… 23

2.1 Fluorine-substituted CPPs previously reported in the literature 39

2.2 Synthesis of the dicatechol-substituted [12]CPP 42

2.3 Synthesis of methoxy and 2-propanethiol-substituted [12]CPPs..... 45

2.4 Synthesis of the diruthenium complex $Ru_2(Ph_2dhbq)$ 48

2.5 Average C–O and Ru–O bond lengths observed in the single crystal 49

3.1 Oxidation-induced planarization of thianthrene 72

3.2 X-ray crystallographic data for 4 77

3.3 Scaled absorbance (solid lines) and emission (dashed lines)..... 78

3.4 DFT space-filling models of CPPs 2 (top) and 4 (bottom) 79

3.5 Cyclic voltammetry scan of 4 showing two reversible oxidations. 80

3.6 UV-Vis and fluorescence profiles of 2 in DCM. 85

3.7 UV-Vis and fluorescence profiles of 4 in DCM. 85

3.8 Scaled absorbance and fluorescence of 4 in various solvents..... 86

3.9 1:1 binding constant for 2 and C60 calculated using BindFit. 87

3.10 2:1 binding constant for 2 and C60 calculated using BindFit. 88

3.11 1:1 binding constant for 4 and C60 calculated using BindFit. 88

3.12 2:1 binding constant for 2 and C60 calculated using BindFit. 89

3.13 HOMO-LUMO orbital distribution of 2.. 93

3.14 HOMO-LUMO orbital distribution of 4. 95

3.15 Host, guest, and host-guest complexes of 2, 4, and C_{60}..... 96

3.16 DFT calculated binding favorability of fullerene complexed with [10]CPP..... 97

3.17 DFT calculated space-filling models of 2 and 4 complexing with C_{60}..... 97

4.1 Representative examples of multi-pore nanohoop like structures.. 103

4.2 X-ray crystal structure unit cells of 3 (a) and 5 (b).. 109

4.3 Diagnostic ^{1}H NMR shifts for trimers and associated [*n*+1]CPPs 110

4.4 StrainViz structures for each trimer and its respective [*n*+1]CPP 112

4.5 Photophysical characterization for the new molecules described herein..... 113

S20 Stacked spectra of starting material (fluor[9+1]CPP) and product 127

S21 Comparison of ^{1}H NMR spectra of diphenylacetylene. 128

S22 Overlay of top spectrum of Figure S21 (black) with $Pd_2(dba)_3$..... 129

S23 Extinction coefficient plot for fluor[9+1]CPP in DCM..... 130

S24 Extinction coefficient plot for fluor[9+1] trimer in DCM. 130

S25 Extinction coefficient plot for fluor-*m*[9+1] trimer in DCM.. 130

S26 Extinction coefficient plot for [9+1] trimer in DCM.. 131

S27 Extinction coefficient plot for [11+1] trimer in DCM.. 131

S28 Quantum yield plot for fluor[9+1]CPP..... 132

S29 Quantum yield plot for fluor[9+1] trimer.. 133

S30 Quantum yield plot for m-fluor[9+1]trimer..... 134

S31 Quantum yield plot for [9+1] trimer.. 135

S32 Quantum yield plot for [11+1] trimer.. 136

S33 Calculated excited state orbital distribution. 137

LIST OF TABLES

Table Page

3.1 Optical absorption transitions for 2..... 90

3.2 Optical absorption transitions for 4..... 93

3.3 DFT calculated binding favorability of CPP-fullerene complexes..... 96

4.1 Metal screening results for conversion of 4 to 5..... 107

4.2 Quantitative strain data as determined by StrainViz..... 111

4.3 Tabulated photophysical data for trimers 113

S1 Stock solution makeup for metal screening experiment..... 125

S2 Integrations of starting material and product peaks..... 126

S3 Compound integration ranges in DMSO and DCM. 132

S4 Quantum yield data for fluor[9+1]CPP. 132

S5 Quantum yield data for fluor[9+1] trimer..... 133

S6 Quantum yield data for m-fluor[9+1]trimer.. 134

S7 Quantum yield data for [9+1] trimer..... 135

S8 Quantum yield data for [11+1] trimer..... 136

S9 Calculated absorption transitions for 5 137

LIST OF SCHEMES

Scheme Page

2.1 Synthesis of the tetrafluorinated [12]CPP, 4F-CPP. 39

3.1 Synthesis of multi-thianthrene-containing CPPs 73

4.1 Conversion of [*n*+1]CPPs to trimers. 103

S2 Overview of the synthesis of fluor-*m*[9+1] trimer. 117

CHAPTER 1

INTRODUCTION

This chapter is adapted from a manuscript in preparation for an ACS Central Science Outlook article with the topic *Nanohoops: today and tomorrow,* and focuses on cycloparaphenylenes as components in quantum technologies. It was written by me with editorial assistance from Professor Ramesh Jasti.

1.1 Carbon Nanomaterials and Cycloparaphenylenes (CPPs)

Carbon nanomaterials are a class of carbon allotropes with at least one dimension on the nanometer scale. The nanometer size of these materials results in a structure-function relationship wherein subtle changes in the size, geometry, and chemical functionality can significantly alter physical properties. The large amount of diverse research on fullerenes (0D), carbon nanotubes (1D), and graphene (2D) since their isolation in 1985[1], 1991[2], and 2004[3] (respectively) is a testament to the far-reaching potential of carbon materials. Recently, carbon nanomaterials have been investigated as platforms for quantum technologies, as the nanometer scale is where quantum properties persist.[4] Somewhat antithetical to their delicate structure-function relationship is the fact that curved carbon nanomaterials, such as CNTs and fullerenes, typically require synthesis by high-energy techniques such as arc-discharge, laser ablation, and chemical vapor deposition.[5,6] These methods do not afford the level of synthetic control over the precise geometry and chemical composition of the nanomaterial that is afforded to smaller nanomaterial fragments made via standard synthetic chemistry techniques.

Fragments of these prototypical carbon nanomaterials such as corannulenes, cycloparaphenylenes (CPPs), and graphene nanoribbons are also very promising candidates for a

diverse range of molecular technologies. These nanomaterial fragments not only exhibit the rich structure-function tunability that makes nanomaterials so diversely applicable, but they also benefit from the synthetic control of bottom-up synthesis.

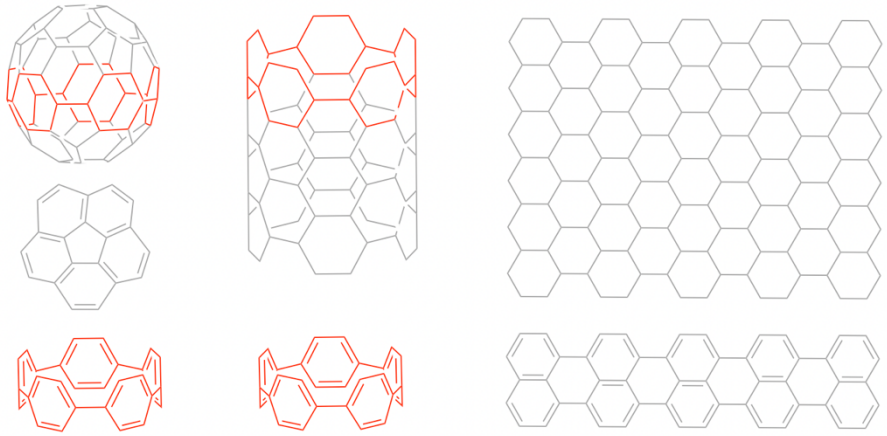

Figure 1.1: Cartoon depictions of a fullerene, armchair carbon nanotube, and graphene sheet and molecular fragments corannulene, [5]cycloparaphenylene, and graphene nanoribbon. Double bonds and/or hydrogens are removed for clarity.

Cycloparaphenylenes (also called [*n*]CPPs or carbon nanohoops) are macrocycles composed of para-linked phenylene rings where *n* is equal to the number of phenylene rings in the nanohoop. Despite being proposed in 1934, CPPs were first synthesized in 2008.[7] The seventy-four-year difference between their conception and realization reflects the inherent difficulty in bending paraphenylene from its preferred planar geometry into a strained macrocycle. The strained geometry of these aromatic macrocycles with radially oriented pi-orbitals is in large part responsible for their unique physiochemical characteristics. Features such as the CPPs supramolecular capabilities, the stabilities of certain functional groups on the CPP backbone, and the HOMO-LUMO and higher-order energy gaps of CPPs, are tunable via changes in diameter,

dimensionality, and functionality. Several synthetic strategies have now been reported for making CPPs and CPP derivatives.[8–13]

Functional CPP derivatives are promising materials to study in part due to their increased solubility and processibility compared to linear systems, which undergo strong insolubilizing pi-pi stacking. The geometrically imparted solubility of the curved CPP facilitates late-stage pi-extending transformations of CPP derivatives. For example, polymerizable units allow for the incorporation of CPP monomers into polymeric systems[14–17], metal-chelating units allow for the incorporation of CPPs into organometallic complexes[18–21] and metal organic frameworks (MOFs)[22], and fluorinated units allow for self-assembly into nanotube-mimics.[23] The curved, radially oriented pi-system allows CPPs the ability to form peapod structures with fullerenes[24], much like single-walled carbon nanotube (SWCNT) fullerene peapods.[25] These host-guest peapod complexes based on both SWCNTs and CPPs with fullerenes have shown potential as components in molecular technologies.

CPP derivatization is often accomplished with early-stage synthetic approaches wherein certain functionality and/or nanoarchitecture is installed in the molecule early on, and the derivatization of the molecule is complete upon formation of the CPP. Carrying functionality and extended pi-systems throughout the multi-step bottom-up CPP synthetic pathway can sometimes diminish yields. Early-stage synthetic techniques can restrict the variety of easily accessible families of derivatives, which are crucial when studying the structure-function effects in nanomaterials. Synthetic approaches that focus on late-stage modification of CPPs offer synthetic freedoms unavailable to more restrictive early-stage functionalization. In late-stage approaches, transformable functional groups that can undergo a variety of reactions are built into the CPP. Unlike early-stage approaches, in late-stage methods the derivatization of the CPP doesn't end

with formation of the CPP. The derivatized CPP is further expanded and decorated with amenable functionalities. This strategy, if successful, can produce families of diverse structures wherein the physiochemical features of the CPP derivative can be studied and then late-stage reactions can afford other related CPP-containing derivatives for comparison. Late-stage synthetic approaches are particularly important for the development of molecular quantum technologies, which require precise tunability of atomic structures and their interaction with the environment.

1.2 Quantum Bits (Qubits)

Quantum information science is a rapidly developing field that combines principles of quantum mechanics with information science, resulting in a powerful platform to usher in quantum technologies.[26] Quantum technologies harness the quantum properties of matter and energy at the nanoscale, such as entanglement, superposition, and tunneling, to accomplish tasks in areas such as computing, sensing, optics, and communication unavailable to classical analogues.[27] Strategies for ushering in diverse quantum technologies are becoming increasingly interdisciplinary, and there is developing interest in creating and implementing quantum technologies with molecular and carbon nanomaterial-based components.

The basic unit of information for quantum technology is the quantum bit, or qubit. Symbolically comparing classical bits with qubits is a straightforward way to get a sense of the inherent information processing differences and technological advantages quantum systems may have compared to classical ones. While classical bits only have the states 0 and 1 available to them, which is a state-space that can be conceptualized two nodes on a line, the state-space of qubits can be conceptualized as a vector pointing anywhere inside of a sphere (known as a Bloch sphere). The vector pointing along opposite poles, such as the north or south poles of the sphere, corresponds to the qubit in the 0 or 1 state. The vector pointing anywhere else in the sphere

represents the ability of the qubit to be in a coherent superposition of the 0 and 1 states. Other features of quantum objects, including the ability of their states to be entangled together, also separate them from classical analogues. Although qubits collapse into either the 0 or 1 state upon measurement, the use of quantum gates and algorithms allows for the extra information contained in the superposition to be used, significantly diversifying the potential applications of qubits compared to classical systems. Constructing quantum gates requires control over the coherence lifetime of the qubit (which is the amount of time the superposition survives and can be used for information processing) and inter-qubit interactions (which influences the implementation of quantum gates and algorithms). Controllable coherence lifetimes and inter-qubit interactions are crucial requirements for quantum technologies, and qubits based on tunable organic molecules and carbon nanomaterials have shown promise in helping address them.

The development and implementation of tailored qubits and multi-qubit arrays is a fundamental challenge of applied quantum information science. The development in exploiting the qubit potential of molecular systems has created an opportunity for synthetic chemists to explore molecular systems that function as qubit components. The basic requirement of a qubit is that it possesses at least two well-defined quantum states, such as the up and down states of electron and nuclear spins, the horizontal and vertical polarization of photons, or the ground and excited energy levels of trapped ions. The five more challenging requirements of viable qubits were outlined by DiVincenzo in 2000 and include: (1) control over the coherence or lifetime of the quantum property (superposition, entanglement, etc.) being exploited for the application, (2) the qubit must be well defined and scalable, (3) the qubit must have the ability to be initialized in a specific quantum state, (4) the response of the qubit must be measurable, and (5) the qubit must be able to devise universal quantum gates (necessitating control over inter-qubit interactions).[28]

Each current qubit system has merits and drawbacks. For example, superconducting circuits are scalable, benefit from well-developed circuit design, and demonstrate fast operation times for computations. However, superconducting qubits typically do not have long coherence times and require extremely low temperatures for operation (tens of millikelvin).[29] Therefore, while superconducting qubits are leading in the construction of large quantum computers, their operational constraints hamper their usage for accessible personal quantum technologies and specific high temperature applications, such as quantum sensing applications in biological systems. Developing new hybrid approaches to implement tunable qubits and optimize features that enhance benefits and mitigate drawbacks is very desirable. This is one of the many reasons why exploiting highly tunable molecular systems for use in quantum technologies has garnered interdisciplinary interest.

1.3 Molecular Qubits

Synthetic control is a powerful tool for developing viable molecule-based qubits with diverse applications in quantum technology. Advancements in preparing supramolecular assemblies, polymers, covalent organic frameworks (COFs), metal organic frameworks (MOFs), and other extended hybrid systems provide complex platforms wherein the chemist can make fine adjustments to the two-level quantum system that defines the qubit, along with the spatial orientation and interactions of multiple qubits. For example, chemists can control the choice of metal ions in organometallic complexes, the degree of stabilization of organic radicals, the energy separation of high oscillator strength transitions in chromophores, and supramolecular interactions of quantum systems. The chemist can also tune the extension of these qubit hosting platforms by, for example, making 3D arrays of stable organic radicals in MOFs or stabilizing metal ion qubits in MOFs with appropriate organic linkers, by changing molecular structure to influence the strong-

coupling of chromophores in optical microcavities, or by tuning the nature of host-guest interactions with qubits on 2D surfaces. This level of control provides valuable tools for addressing the five requirements of viable qubits mentioned prior.

Carbon-based qubits that utilize the up and down spins of electrons in stable organic radicals or paramagnetic organometallic complexes to encode quantum information are rapidly becoming more well studied.[30–32] Carbon-based spin-qubits show promise as components that can display long coherence times, in part due to being composed of light elements (C,H,N,O,P,S, etc.) that have low spin-orbit coupling, a source of decoherence.[33] Molecular qubits have the potential to extend to form one-, two-, and three-dimensional architectures, and interface with other qubits, such as superconducting circuits, to mitigate drawbacks. Developing molecular systems that can still maintain long coherence times upon integration into quantum devices, which typically necessitates formation of thin films, ordered layers on surfaces, etc., is an ongoing challenge.

Curved carbon nanomaterials such as fullerenes and carbon nanotubes are promising qubit components to address the challenges of hosting long-lived spin-qubits while also being amenable to device integration. Their curved geometry provides energetic and morphological features unattainable in linear systems. Cycloparaphenylenes have also recently shown promise as qubit hosts. However, research in this area is very limited compared to that of fullerenes and CNTs. Below we discuss some relevant studies of fullerene and/or CNT based qubits and their integration into hybrid platforms, such as SWCNT-fullerene host-guest complexes, MOFs, and cavity quantum electrodynamic (cQED) systems. Later we discuss the limited but extremely promising work that has been done using CPPs as qubit components to shield quantum information in fullerenes, which has afforded complexes with exceptionally long coherence times. Some

suggestions for future areas of study are made with a focus on novel CPP architectures and hybrid cQED platforms.

1.31 Fullerene and Carbon Nanotube Qubits

Endohedral fullerenes are host-guest complexes wherein the hollow center of fullerene hosts an atom, ion, or atomic cluster guest. (Fig 1.2 a)In some cases, this hosted guest can behave as a qubit, benefiting both from the shielding provided by the fullerene skeleton and the inter-qubit control provided by the supramolecular characteristics of fullerene. For example, an endohedral fullerene qubit with a well-shielded electron spin is possible with N@C60, which is a complex with atomic nitrogen inside of C60. N@C60 can behave as a robust spin-qubit with a remarkably long lifetimes for electron spin coherence under certain conditions.[34,35]

In 2006, researchers observed a coherence time of 0.25 milliseconds (ms) at 170 K for N@C60 in a liquid CS2 solution, which at the time was the longest coherence time reported for any molecular electron spin qubit.[36] Importantly, they found that the coherence time of the system was long enough to allow for sufficient quantum gate operations to be enacted, which is required for quantum processing applications. In addition to liquid state, N@C60 qubits have also been probed in their crystalline powder form and hosted in solid-state SWCNT peapod platforms. Researchers found that at room temperature the crystalline powder and SWCNT-N@C60 peapods displayed 20 microsecond (μs) and 13 μs coherence lifetimes respectively.[37,38] Although in this case complexation with SWCNTs decreased the electron spin coherence lifetime of N@C60, the N@C60 molecule itself was more stable to high temperatures when protected by the SWCNT host. This added stability is an important feature for device fabrication strategies with high temperature steps. Multi-qubit arrays formed from fullerenes in SWCNTs are promising quasi-1D platforms (Fig 1.2 c).

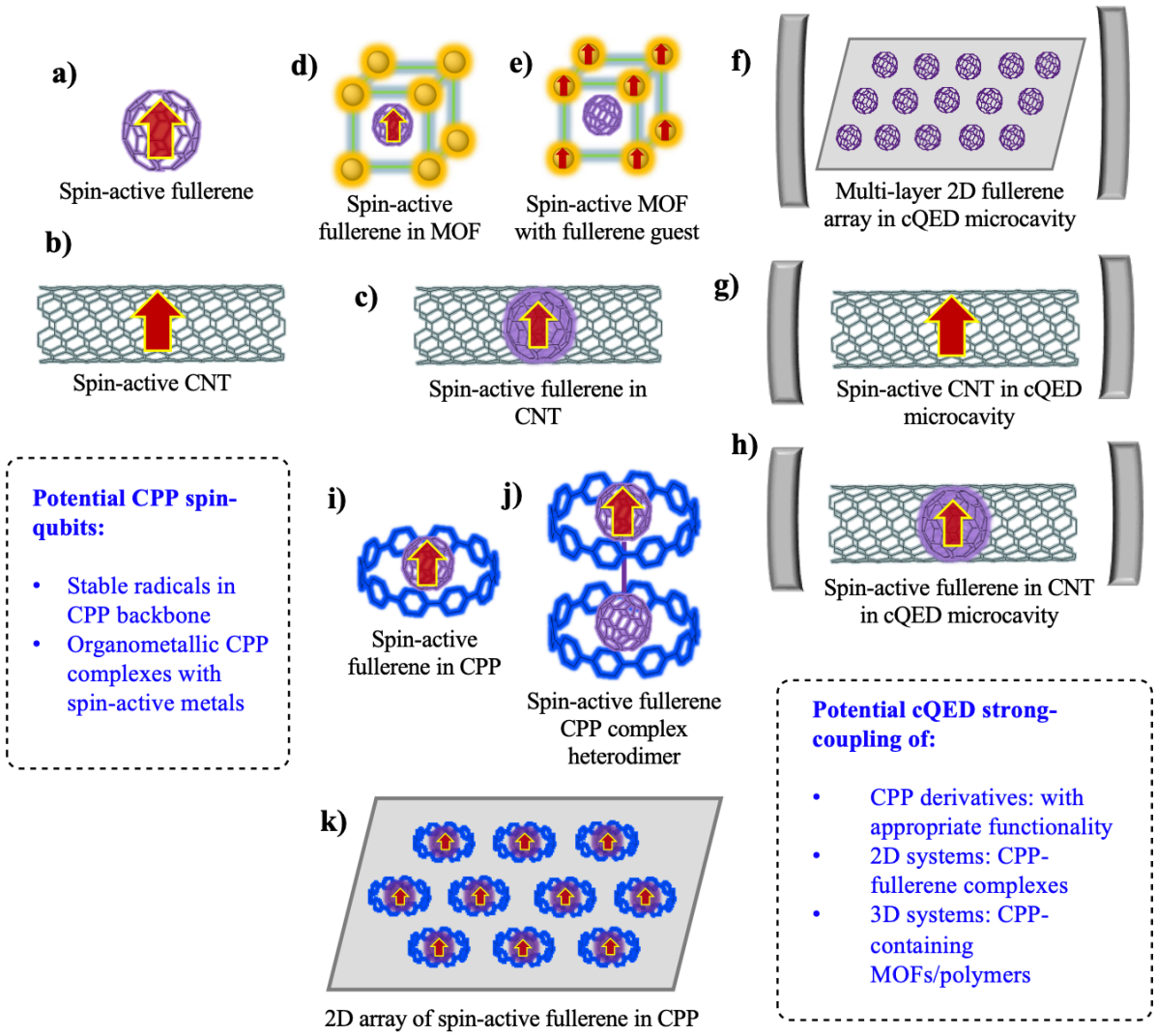

Figure 1.2: Cartoons of qubit platforms discussed in this article. These cartoons do not accurately represent the actual device configurations or structure of the fullerene, MOF, or CNT reported.

Other strategies such as extending endohedral fullerene qubits into 3D arrays via their incorporation into 3D MOFs are being explored (Fig. 1.2 d). In 2015, researchers reported a spin-active solid-state system based on the paramagnetic metallofullerene Y2@C79N hosted in the pores of MOF-177.[39] They posit that the system displayed potential use as a qubit for data storage or as a sensor for appropriately labeled biomolecules. In 2024, researchers investigated the assembly of N@C60 spin-qubits also into MOF-177.[40] They proposed that the system studied was

a feasible platform for spin-based quantum sensing. They were able to prepare and manipulate coherent spin superpositions in the extended system, which displayed a coherence time of 4 μs at 100 K. The potential for making 3D arrays of spin-active materials with appropriately long spin coherence times makes endofullerene based qubits promising. Alternatively, instead of using endohedral fullerenes as the spin-qubit host-guest complexes further hosted in MOFs, unfunctionalized fullerenes can be used as components in hybrid systems with other spin-active qubits (Fig. 1.2 e). In 2023, researchers reported that unfunctionalized C60 guests in zirconium MOF composites with copper(II) porphyrin spin-active qubits can serve as nuclear-spin free components reducing environmental spin pollution from solvents and increasing the rigidity of the framework.[41] This incorporation of C60 led to an increase in the spin coherence lifetime of the system with increasing amounts of C60. The system with the most C60 had the longest coherence time (800 nanoseconds (ns) at 5 K) and the system without C60 had the shortest (540 ns).

The last hybrid molecular-qubit platform strategy discussed here involves principles of cavity quantum electrodynamics (cQED) as a handle to create and manipulate coherent quantum platforms based on fullerene and CNT components. Cavity quantum electrodynamics allows for the coherent strong coupling between two-level systems (such as the up and down spin of electrons or the ground and excited states of optical transitions) and the electromagnetic field confined by the cavity.[42] If strong enough coupling between the matter (two-level system) and energy (the electromagnetic field) components occur, then new hybrid bosonic quasiparticles called polaritons are created.[43] These quasiparticles are characterized by the rapid emission and reabsorption of energy (ex: a trapped photon) by the confined two-level system (ex: exciton tuned to the cavity resonance). Polaritons are superpositions between light and matter that have shown important potential as advanced qubit platform components.[44–49]

In 2022, researchers uncovered that polariton formation was possible with multiple 2D layers of C60 in microcavities (Fig. 1.2 f).[50] These polaritons are formed by repeated exchanges of energy between the excitons in layers of C60 and the confined photons in the microcavity. Importantly, the system studied displayed a controllable shift from the weak coupling regime (energy lost to the environment faster than reabsorption) into the strong coupling polariton regime (hybridization of energy and matter) by increasing the number of layers of C60 from 1 to 60 respectively. This is an important result, as many device platforms necessitate extended 2D arrays of qubits, and polaritons in the strong coupling regime are potential viable qubits.

Single-walled carbon nanotubes are also well-studied hosts for spin-qubits. Recent developments have focused on the fabrication of spin-based CNT systems in cQED platforms, as the strong-coupling regime can afford a means to interact with and manipulate the qubit (Fig. 1.2 g). In 2019, researchers reported the strong coupling of spin states in SWCNTs coupled to microwave cavity confined photons.[51] With this cQED setup, they were able to harness the cavity photons and use them to coherently control the state of a single electron spin qubit confined in the nanotube. They found that their device setup had a low decoherence rate, providing quantum coherence lifetimes (637 ns) over 100 times longer than previous work on CNT qubits. This coherence lifetime has been surpassed in a 2024 study that also exploits confined quantum-dot spin-states in SWCNTs coupled to microcavities.[52] The cQED system implemented in this study affords an impressive coherence lifetime of 1.3 μs, which they reported as a value higher than any other quantum dots in cavities of any material. Finally, although there are no experimental studies reported thus far, highly hybridized systems with spin-active doped fullerenes hosted inside of SWCNTs further hosted inside of cQED microcavities have been proposed for advanced quantum information processing applications (Fig. 1.2 h).[53] This hybrid approach and other like it highlights

the need for and benefit of highly tailored quantum platforms with tunable curved carbon nanomaterial components.

1.4 Realized/Potential Applications of CPPs in Qubit Architectures

In this section we highlight promising studies that suggest CPPs as candidates for viable hybrid qubit systems. We also discuss future areas of study focused on cQED treatments of CPPs and their hybrid systems. Thus far, CPP-based qubit research has focused on using CPPs as shields to protect fullerene-based spin qubits from decoherence. This approach is reminiscent of the protection of spin-qubits in fullerenes, CNTs, and fullerene-CNT peapods, as CPPs can be thought of structurally as fundamental units of these curved carbon nanomaterials. Important results from the multi-layer shielding CPP-based approach were reported in 2021 when researchers found that azafullerene radicals (typically unstable at room temperature) when complexed with [10]CPP in the solid-state are chemically stable for several years at room temperature (Fig. 1.2 i).[54] Importantly, they were also able to measure long room temperature spin-lattice coherence times of 210 μs, surpassing the spin-lattice coherence time of 120 μs for N@C60 crystalline powders measured at -83 C. When cooled to -83 C, the [10]CPP azafullerene radical complex displayed a spin-lattice coherence lifetime (2.9 ms), over 20 times longer than N@C60 powder. In 2023, the same group reported the longest room temperature coherence time (440 μs) of any fullerene radical species by utilizing the [10]CPP hosts.[55] They showed that coherence lifetimes could be increased in the [10]CPP azafullerene radical complexes via the incorporation of C60 into the system, leading to stable [10]CPP⊃C_{59}N-C_{60}•⊂[10]CPP heterodimer radical qubits (Fig. 1.2 j). These promising studies have inspired further investigation into the amenability of CPP-shielded fullerene qubits into 2D device architectures.

A more recent study reported in 2025 uncovered that azafullerene radicals stabilized by [10]CPP hosts are in fact amenable to 2D extension via self-assembly on gold surfaces (Fig. 1.2 k).[56] Researchers found that vacuum deposition of azafullerene radicals on a layer of [10]CPP on a gold surface afforded a dense 2D network of stable spins. Importantly, the $C_{59}N^{\bullet}\subset$[10]CPP system prevents the radical from dimerizing (as in the unprotected azafullerene radical) and prevents the coupling of the azafullerene radical to the gold surface even after annealing at 340 C. The demonstrated ability of CPPs to increase the coherence lifetimes of hosted qubits in room temperature environments while also providing a platform for efficient self-assembly into 2D spin-active architectures is very promising.

Although there are a handful of studies suggesting the applicability of CPPs to qubit platforms, much more research is needed to realize the potential of these systems. Nearly all the work done on CPP-containing qubit platforms involve an unfunctionalized or slightly derivatized CPP hosting a fullerene-based qubit. Considering the impressive strides that have been made in expanding and functionalizing CPP derivatives, future work could focus on exploring these derivatives in quantum technologies. For example, the tunability of the organization and interaction of spin carriers on a mono or multi-layered 2D sheet could be explored using extended CPP systems with multiple pores and/or tailored functionalities. The previously mentioned results that show the longest fullerene-based coherence time with the [10]CPP$\supset C_{59}N$-$C_{60}^{\bullet}\subset$[10]CPP heterodimer radical qubits paired with the results that show the amenability of azafullerene radical CPP complexes to be extended in 2D could inspire a multi-layered 2D heterodimer radical qubit system. Taking further inspiration from non-CPP-containing studies of multi-layer 2D fullerene arrays in cQED microcavities and combining that approach with strategies that include CPP shields could inform the development of coherent qubit systems that are addressable by light and amenable

to device integration. To our knowledge there are no current reports of CPPs or CPP-containing systems being investigated via cQED techniques, however we believe that these tunable and highly soluble fluorophores are unique species to study.

Future work could also focus on employing synthetic strategies to exploit the CPP itself as an addressable two-level system. CPPs have been shown to stabilize organic radicals due to favorable delocalization around the ring[57], so there is potential to introduce appropriate radical-qubit forming groups in the CPP backbone. An exciting result was reported in 2022 when researchers reported the first MOF with CPPs in the framework.[22] They found that the incorporation of [8]CPP into a MOF FDM-1001 followed by radical generating oxidation in the solid state afforded an extended array of radicals with increased air-stability compared to the free [8]CPP radical. Importantly, they found that the CPPs orient themselves in a directional manner and have available pore space for hosting guests. This affords a complex and highly organized 3D arrangement of stable-guest available CPPs or CPP radicals. While this study did not probe the ability of the system as a qubit platform, the results are a promising confirmation of the extendibility of CPPs and CPP-based radicals. Radical CPP systems could potentially be further shielded and addressable via integration into cQED platforms that may inform the development of CPP-based spin-polaritons. There are promising studies wherein MOFs in cQED microcavities have shown the formation of guest responsive polaritons.[58] Considering the ability of both CPPs and MOFs to host fullerenes, and the work that has been done on improving MOF-based qubits via fullerene complexation, CPP-containing extended hybrid systems will be promising qubit candidates to investigate.

1.5 Conclusion

Researchers in the growing field of quantum technology have found that the tunability of single molecules and their extended systems provides a platform for addressing the five requirements for viable qubits mentioned prior. Specifically, molecular qubits show promise as components that can display long coherence times (even at elevated temperatures), can be expanded into large quantum architectures to realize quantum gates, and can be interfaced with other promising quantum platforms (such as superconducting systems) to mitigate drawbacks. CPPs have tunable features that afford control over their energy levels (e.g.: electronic transitions, vibrational transitions of appended functional groups, stability of unpaired electron-containing groups, etc.) that may be useful as qubits under the right conditions. The ability of unfunctionalized CPPs to shield and stabilize potential qubits such as radicals and ions is very promising especially when considering the ever-expanding CPP architectures. The amenability of CPPs to derivatization, extension, and supramolecular interactions may allow for controlled qubit environments. Interdisciplinary research is needed to fully exploit the potential of these tunable curved carbon nanomaterials.

1.6 Bridge to Chapter II

Chapter I begins with a broad overview of carbon nanomaterials, quantum information science, and the role that synthetic organic chemists may play in developing new types of quantum bits. It then narrows to discuss molecular qubits based on curved carbon allotropes namely, fullerene, SWCNTs, and CNT-fullerene host-guest systems. Some of the key studies that investigate the use of CPP hybrid systems as components in quantum technologies are discussed along with potential future directions for researchers in this highly interdisciplinary field. There is a large emphasis on the need for highly tailored and atomically precise materials in the field of

quantum technology, making highly tunable CPP based nanomaterials very attractive candidates to help deepen our understanding of molecular based qubits. Increased means of efficient functionalization and extension of the CPP scaffold help inform the science and application of curved carbon allotropes. Chapter II focuses on the use of nucleophilic aromatic substitution as a late-stage method to convert fluorinated CPPs into organic ligands which are then metalated.

1.7 References

(1) Kroto, H. W.; Heath, J. R.; O'Brien, S. C.; Curl, R. F.; Smalley, R. E. C60: Buckminsterfullerene. *Nature* **1985**, *318* (6042), 162–163. https://doi.org/10.1038/318162a0.

(2) Iijima, S. Helical Microtubules of Graphitic Carbon. *Nature* **1991**, *354* (6348), 56. https://doi.org/10.1038/354056a0.

(3) Novoselov, K. S.; Geim, A. K.; Morozov, S. V.; Jiang, D.; Zhang, Y.; Dubonos, S. V.; Grigorieva, I. V.; Firsov, A. A. Electric Field Effect in Atomically Thin Carbon Films. *Science* **2004**, *306* (5696), 666–669. https://doi.org/10.1126/science.1102896.

(4) Alfieri, A.; Anantharaman, S. B.; Zhang, H.; Jariwala, D. Nanomaterials for Quantum Information Science and Engineering. *Adv. Mater.* **2023**, *35* (27), 2109621. https://doi.org/10.1002/adma.202109621.

(5) Szabó, A.; Perri, C.; Csató, A.; Giordano, G.; Vuono, D.; Nagy, J. B. Synthesis Methods of Carbon Nanotubes and Related Materials. *Materials* **2010**, *3* (5), 3092–3140. https://doi.org/10.3390/ma3053092.

(6) Prasek, J.; Drbohlavova, J.; Chomoucka, J.; Hubalek, J.; Jasek, O.; Adam, V.; Kizek, R. Methods for Carbon Nanotubes Synthesis—Review. *J. Mater. Chem.* **2011**, *21* (40), 15872. https://doi.org/10.1039/c1jm12254a.

(7) Jasti, R.; Bhattacharjee, J.; Neaton, J. B.; Bertozzi, C. R. Synthesis, Characterization, and Theory of [9]-, [12]-, and [18]Cycloparaphenylene: Carbon Nanohoop Structures. *J. Am. Chem. Soc.* **2008**, *130* (52), 17646–17647. https://doi.org/10.1021/ja807126u.

(8) Li, Y.; Kono, H.; Maekawa, T.; Segawa, Y.; Yagi, A.; Itami, K. Chemical Synthesis of Carbon Nanorings and Nanobelts. *Acc. Mater. Res.* **2021**, *2* (8), 681–691. https://doi.org/10.1021/accountsmr.1c00105.

(9) Wu, D.; Cheng, W.; Ban, X.; Xia, J. Cycloparaphenylenes (CPPs): An Overview of Synthesis, Properties, and Potential Applications. *Asian J. Org. Chem.* **2018**, *7* (11), 2161–2181. https://doi.org/10.1002/ajoc.201800397.

(10) E. Lewis, S. Cycloparaphenylenes and Related Nanohoops. *Chem. Soc. Rev.* **2015**, *44* (8), 2221–2304. https://doi.org/10.1039/C4CS00366G.

(11) Lu, D.; Huang, Q.; Wang, S.; Wang, J.; Huang, P.; Du, P. The Supramolecular Chemistry of Cycloparaphenylenes and Their Analogs. *Front. Chem.* **2019**, *7*.

(12) Darzi, E. R.; Jasti, R. The Dynamic, Size-Dependent Properties of [5]–[12]Cycloparaphenylenes. *Chem. Soc. Rev.* **2015**, *44* (18), 6401–6410. https://doi.org/10.1039/C5CS00143A.

(13) Omachi, H.; Segawa, Y.; Itami, K. Synthesis of Cycloparaphenylenes and Related Carbon Nanorings: A Step toward the Controlled Synthesis of Carbon Nanotubes. *Acc. Chem. Res.* **2012**, *45* (8), 1378–1389. https://doi.org/10.1021/ar300055x.

(14) Zhang, J.; Cheng, H.; Meng, Z.; Zhang, H.; Luo, Z.; Muddassir, M.; Li, X.; Sha, Y. Side-Chain Meta [6]Cycloparaphenylene-Based Nanoring-Containing Polymers. *Polym. Chem.* **2023**, *14* (45), 5029–5033. https://doi.org/10.1039/D3PY01058A.

(15) Peters, G. M.; Grover, G.; Maust, R. L.; Colwell, C. E.; Bates, H.; Edgell, W. A.; Jasti, R.; Kertesz, M.; Tovar, J. D. Linear and Radial Conjugation in Extended π-Electron Systems. *J. Am. Chem. Soc.* **2020**, *142* (5), 2293–2300. https://doi.org/10.1021/jacs.9b10785.

(16) Peterson, E.; Maust, R. L.; Jasti, R.; Kertesz, M.; Tovar, J. D. Splitting the Ring: Impact of Ortho and Meta Pi Conjugation Pathways through Disjointed [8]Cycloparaphenylene

Electronic Materials. *J. Am. Chem. Soc.* **2022**, *144* (10), 4611–4622. https://doi.org/10.1021/jacs.2c00419.
(17) Huang, Q.; Zhuang, G.; Zhang, M.; Wang, J.; Wang, S.; Wu, Y.; Yang, S.; Du, P. A Long π-Conjugated Poly(Para-Phenylene)-Based Polymeric Segment of Single-Walled Carbon Nanotubes. *J. Am. Chem. Soc.* **2019**, *141* (48), 18938–18943. https://doi.org/10.1021/jacs.9b10358.
(18) Heras Ojea, M. J.; Van Raden, J. M.; Louie, S.; Collins, R.; Pividori, D.; Cirera, J.; Meyer, K.; Jasti, R.; Layfield, R. A. Spin-Crossover Properties of an Iron(II) Coordination Nanohoop. *Angew. Chem. Int. Ed.* **2021**, *60* (7), 3515–3518. https://doi.org/10.1002/anie.202013374.
(19) Van Raden, J. M.; Louie, S.; Zakharov, L. N.; Jasti, R. 2,2′-Bipyridyl-Embedded Cycloparaphenylenes as a General Strategy To Investigate Nanohoop-Based Coordination Complexes. *J. Am. Chem. Soc.* **2017**, *139* (8), 2936–2939. https://doi.org/10.1021/jacs.7b00359.
(20) A. Kamin, A.; D. Clayton, T.; E. Otteson, C.; M. Gannon, P.; Krajewski, S.; Kaminsky, W.; Jasti, R.; J. Xiao, D. Synthesis and Metalation of Polycatechol Nanohoops Derived from Fluorocycloparaphenylenes. *Chem. Sci.* **2023**, *14* (36), 9724–9732. https://doi.org/10.1039/D3SC03561A.
(21) Kayahara, E.; Patel, V. K.; Mercier, A.; Kündig, E. P.; Yamago, S. Regioselective Synthesis and Characterization of Multinuclear Convex-Bound Ruthenium-[n]Cycloparaphenylene (N=5 and 6) Complexes. *Angew. Chem. Int. Ed.* **2016**, *55* (1), 302–306. https://doi.org/10.1002/anie.201508003.
(22) Jiang, Z.; Duan, W.; Lin, W.; Yang, L.; Wu, Z.; Wang, J.; Wang, S.; Du, P.; Li, Q. Cycloparaphenylene and Their Radicals Anchored to a Metal−organic Framework. *Mater. Today Chem.* **2022**, *25*, 100973. https://doi.org/10.1016/j.mtchem.2022.100973.
(23) Van Raden, J. M.; Leonhardt, E. J.; Zakharov, L. N.; Pérez-Guardiola, A.; Pérez-Jiménez, A. J.; Marshall, C. R.; Brozek, C. K.; Sancho-García, J. C.; Jasti, R. Precision Nanotube Mimics via Self-Assembly of Programmed Carbon Nanohoops. *J. Org. Chem.* **2020**, *85* (1), 129–141. https://doi.org/10.1021/acs.joc.9b02340.
(24) Iwamoto, T.; Watanabe, Y.; Sadahiro, T.; Haino, T.; Yamago, S. Size-Selective Encapsulation of C60 by [10]Cycloparaphenylene: Formation of the Shortest Fullerene-Peapod. *Angew. Chem. Int. Ed.* **2011**, *50* (36), 8342–8344. https://doi.org/10.1002/anie.201102302.
(25) Smith, B. W.; Monthioux, M.; Luzzi, D. E. Encapsulated C60 in Carbon Nanotubes. *Nature* **1998**, *396* (6709), 323–324. https://doi.org/10.1038/24521.
(26) Hayashi, M.; Ishizaka, S.; Kawachi, A.; Kimura, G.; Ogawa, T. *Introduction to Quantum Information Science*; Springer, 2014.
(27) MacFarlane, A. G. J.; Dowling, J. P.; Milburn, G. J. Quantum Technology: The Second Quantum Revolution. *Philos. Trans. R. Soc. Lond. Ser. Math. Phys. Eng. Sci.* **2003**, *361* (1809), 1655–1674. https://doi.org/10.1098/rsta.2003.1227.
(28) DiVincenzo, D. P. The Physical Implementation of Quantum Computation. *Fortschritte Phys.* **2000**, *48* (9–11), 771–783. https://doi.org/10.1002/1521-3978(200009)48:9/11<771::AID-PROP771>3.0.CO;2-E.
(29) Chohan, A. A Comparative Review of Quantum Bits: Superconducting, Topological, Spin, and Emerging Qubit Technologies.

(30) Zhou, A.; Sun, Z.; Sun, L. Stable Organic Radical Qubits and Their Applications in Quantum Information Science. *The Innovation* **2024**, *5* (5), 100662. https://doi.org/10.1016/j.xinn.2024.100662.
(31) Náfrádi, B.; Choucair, M.; Dinse, K.-P.; Forró, L. Room Temperature Manipulation of Long Lifetime Spins in Metallic-like Carbon Nanospheres. *Nat. Commun.* **2016**, *7*, 12232. https://doi.org/10.1038/ncomms12232.
(32) Zadrozny, J. M.; Niklas, J.; Poluektov, O. G.; Freedman, D. E. Millisecond Coherence Time in a Tunable Molecular Electronic Spin Qubit. *ACS Cent. Sci.* **2015**, *1* (9), 488–492. https://doi.org/10.1021/acscentsci.5b00338.
(33) Datta, S. N.; Pal, A. K.; Panda, A. Design of Magnetic Organic Molecules and Organic Magnets: Experiment, Theory and Computation with Application and Recent Advances. *Chem. Phys. Impact* **2023**, *7*, 100379. https://doi.org/10.1016/j.chphi.2023.100379.
(34) Knapp, C.; Dinse, K.-P.; Pietzak, B.; Waiblinger, M.; Weidinger, A. Fourier Transform EPR Study of N@C60 in Solution. *Chem. Phys. Lett.* **1997**, *272* (5), 433–437. https://doi.org/10.1016/S0009-2614(97)00577-0.
(35) Morton, J. J. L.; Tyryshkin, A. M.; Ardavan, A.; Porfyrakis, K.; Lyon, S. A.; Briggs, G. A. D. Environmental Effects on Electron Spin Relaxation in $\mathrm{N}@{\mathrm{C}}_{60}$. *Phys. Rev. B* **2007**, *76* (8), 085418. https://doi.org/10.1103/PhysRevB.76.085418.
(36) Morton, J. J. L.; Tyryshkin, A. M.; Ardavan, A.; Porfyrakis, K.; Lyon, S. A.; Andrew D. Briggs, G. Electron Spin Relaxation of N@C60 in CS2. *J. Chem. Phys.* **2006**, *124* (1), 014508. https://doi.org/10.1063/1.2147262.
(37) Harneit, W. Fullerene-Based Electron-Spin Quantum Computer. *Phys. Rev. A* **2002**, *65* (3), 032322. https://doi.org/10.1103/PhysRevA.65.032322.
(38) Tóth, S.; Quintavalle, D.; Náfrádi, B.; Korecz, L.; Forró, L.; Simon, F. Enhanced Thermal Stability and Spin-Lattice Relaxation Rate of N@${\text{C}}_{60}$ inside Carbon Nanotubes. *Phys. Rev. B* **2008**, *77* (21), 214409. https://doi.org/10.1103/PhysRevB.77.214409.
(39) Feng, Y.; Wang, T.; Li, Y.; Li, J.; Wu, J.; Wu, B.; Jiang, L.; Wang, C. Steering Metallofullerene Electron Spin in Porous Metal–Organic Framework. *J. Am. Chem. Soc.* **2015**, *137* (47), 15055–15060. https://doi.org/10.1021/jacs.5b10796.
(40) Hui, X.-Y.; Zhang, Y.-S.; Xiong, Q.; Wu, Z.-R.; Gao, S.; Zhou, S.; Jiang, S.-D. A 3D-Assembled Endohedral Nitrogen Fullerene in a Metal–Organic Framework toward Spin Qubit and Quantum Sensors. *Inorg. Chem. Front.* **2024**, *11* (21), 7340–7345. https://doi.org/10.1039/D4QI01782J.
(41) Vujević, L.; Karadeniz, B.; Cindro, N.; Krajnc, A.; Mali, G.; Mazaj, M.; M. Avdoshenko, S.; A. Popov, A.; Žilić, D.; Užarević, K.; Kveder, M. Improving the Molecular Spin Qubit Performance in Zirconium MOF Composites by Mechanochemical Dilution and Fullerene Encapsulation. *Chem. Sci.* **2023**, *14* (35), 9389–9399. https://doi.org/10.1039/D3SC03089J.
(42) Haroche, S.; Kleppner, D. Cavity Quantum Electrodynamics. *Phys. Today* **1989**, *42* (1), 24–30. https://doi.org/10.1063/1.881201.
(43) Herrera, F.; Owrutsky, J. Molecular Polaritons for Controlling Chemistry with Quantum Optics. *J. Chem. Phys.* **2020**, *152* (10), 100902. https://doi.org/10.1063/1.5136320.
(44) Samkharadze, N.; Zheng, G.; Kalhor, N.; Brousse, D.; Sammak, A.; Mendes, U. C.; Blais, A.; Scappucci, G.; Vandersypen, L. M. K. Strong Spin-Photon Coupling in Silicon. *Science* **2018**, *359* (6380), 1123–1127. https://doi.org/10.1126/science.aar4054.

(45) Yu, C. X.; Zihlmann, S.; Abadillo-Uriel, J. C.; Michal, V. P.; Rambal, N.; Niebojewski, H.; Bedecarrats, T.; Vinet, M.; Dumur, É.; Filippone, M.; Bertrand, B.; De Franceschi, S.; Niquet, Y.-M.; Maurand, R. Strong Coupling between a Photon and a Hole Spin in Silicon. *Nat. Nanotechnol.* **2023**, *18* (7), 741–746. https://doi.org/10.1038/s41565-023-01332-3.
(46) Noiri, A.; Takeda, K.; Nakajima, T.; Kobayashi, T.; Sammak, A.; Scappucci, G.; Tarucha, S. A Shuttling-Based Two-Qubit Logic Gate for Linking Distant Silicon Quantum Processors. *Nat. Commun.* **2022**, *13* (1), 5740. https://doi.org/10.1038/s41467-022-33453-z.
(47) Burkard, G.; Ladd, T. D.; Pan, A.; Nichol, J. M.; Petta, J. R. Semiconductor Spin Qubits. *Rev. Mod. Phys.* **2023**, *95* (2), 025003. https://doi.org/10.1103/RevModPhys.95.025003.
(48) Ricco, L. S.; Shelykh, I. A.; Kavokin, A. Qubit Gate Operations in Elliptically Trapped Polariton Condensates. *Sci. Rep.* **2024**, *14* (1), 4211. https://doi.org/10.1038/s41598-024-54543-6.
(49) Demirchyan, S. S.; Chestnov, I. Yu.; Alodjants, A. P.; Glazov, M. M.; Kavokin, A. V. Qubits Based on Polariton Rabi Oscillators. *Phys. Rev. Lett.* **2014**, *112* (19), 196403. https://doi.org/10.1103/PhysRevLett.112.196403.
(50) Despoja, V.; Novko, D. Transition from Weak to Strong Light-Molecule Coupling: Application to Fullerene ${\mathrm{C}}_{60}$ Multilayers in Metallic Cavity. *Phys. Rev. B* **2022**, *106* (20), 205401. https://doi.org/10.1103/PhysRevB.106.205401.
(51) Cubaynes, T.; Delbecq, M. R.; Dartiailh, M. C.; Assouly, R.; Desjardins, M. M.; Contamin, L. C.; Bruhat, L. E.; Leghtas, Z.; Mallet, F.; Cottet, A.; Kontos, T. Highly Coherent Spin States in Carbon Nanotubes Coupled to Cavity Photons. *Npj Quantum Inf.* **2019**, *5* (1), 1–5. https://doi.org/10.1038/s41534-019-0169-4.
(52) Neukelmance, B.; Hue, B.; Schaeverbeke, Q.; Jarjat, L.; Théry, A.; Craquelin, J.; Legrand, W.; Cubaynes, T.; Abulizi, G.; Becdelievre, J.; Abbassi, M. E.; Larrouy, A.; Ourak, K. F.; Stefani, D.; Sulpizio, J. A.; Cottet, A.; Desjardins, M. M.; Kontos, T.; Delbecq, M. R. Microsecond-Lived Quantum States in a Carbon-Based Circuit Driven by Cavity Photons. arXiv October 25, 2024. https://doi.org/10.48550/arXiv.2410.19477.
(53) Hu, Y. M.; Yang, W. L.; Feng, M.; Du, J. F. Distributed Quantum-Information Processing with Fullerene-Caged Electron Spins in Distant Nanotubes. *Phys. Rev. A* **2009**, *80* (2), 022322. https://doi.org/10.1103/PhysRevA.80.022322.
(54) Tanuma, Y.; Stergiou, A.; Bobnar, A. B.; Gaboardi, M.; Rio, J.; Volkmann, J.; Wegner, H. A.; Tagmatarchis, N.; Ewels, C. P.; Arčon, D. Robust Coherent Spin Centers from Stable Azafullerene Radicals Entrapped in Cycloparaphenylene Rings. *Nanoscale* **2021**, *13* (47), 19946–19955. https://doi.org/10.1039/D1NR06393F.
(55) Tanuma, Y.; Knaflič, T.; Anézo, B.; Stangel, C.; Volkmann, J.; Tagmatarchis, N.; Wegner, H. A.; Arčon, D.; Ewels, C. P. Long Spin Coherence Times on C59N-C60 Heterodimer Radicals Entrapped in Cycloparaphenylene Rings. *J. Phys. Chem. C* **2023**, *127* (13), 6552–6561. https://doi.org/10.1021/acs.jpcc.2c09049.
(56) Kladnik, G.; Schio, L.; Bavdek, G.; Tanuma, Y.; van Midden Mavrič, M.; Zupanič, E.; Anézo, B.; Sideri, I. K.; Tagmatarchis, N.; Volkmann, J.; Wegner, H. A.; Goldoni, A.; Ewels, C. P.; Morgante, A.; Floreano, L.; Arčon, D.; Cvetko, D. Engineering 2D Spin Networks by On-Surface Encapsulation of Azafullerene Radicals in Nanotemplates. *Nat. Commun.* **2025**, *16* (1), 193. https://doi.org/10.1038/s41467-024-55521-2.
(57) Toriumi, N.; Muranaka, A.; Kayahara, E.; Yamago, S.; Uchiyama, M. In-Plane Aromaticity in Cycloparaphenylene Dications: A Magnetic Circular Dichroism and Theoretical Study. *J. Am. Chem. Soc.* **2015**, *137* (1), 82–85. https://doi.org/10.1021/ja511320f.

(58) Haldar, R.; Fu, Z.; Joseph, R.; Herrero, D.; Martín-Gomis, L.; Richards, B. S.; Howard, I. A.; Sastre-Santos, A.; Wöll, C. Guest-Responsive Polaritons in a Porous Framework: Chromophoric Sponges in Optical QED Cavities. *Chem. Sci.* **2020**, *11* (30), 7972–7978. https://doi.org/10.1039/D0SC02436H.

Chapter II

SYNTHESIS AND METALATION OF POLYCATECHOL NANOHOOPS DERIVED FROM FLUOROCYCLOPARAPHENYLENES

Chapter II is adapted from a study published in Chemical Science entitled "Synthesis and Metalation of Polycatechol Nanohoops Derived from Fluorocycloparaphenylenes."

The fluorinated CPPs described herein were synthesized and characterized by me, and all the substitution and metalation products were synthesized and characterized by Ashlyn A. Kamin. Ashlyn A. Kamin and Dianne J. Xiao designed the research and wrote the manuscript; Paige M. Gannon, Sebastian Krajewski, and Werner Kaminsky collected and refined the crystallographic data; Ashlyn A. Kamin performed the DFT calculations. All authors interpreted the results and contributed to reviewing and editing the manuscript.

2.1 Introduction

Cycloparaphenylenes ([*n*]CPPs, where *n* is the number of phenylene units) are a class of highly strained macrocyclic molecules with radially oriented π systems and unique optoelectronic properties.[1–5] Ever since their initial synthesis in 2008,[6] the potential to elongate these "carbon nanohoops" into homochiral carbon nanotubes and other extended materials has captivated the imagination of researchers.[1,7] In 2013, [*n*]CPP templates (*n* = 9, 12) were shown to be competent seeds for the growth of carbon nanotubes with tunable diameters.[8] Recently, spurred by new advances in the synthetic chemistry of CPPs,[4,9–11] functionalized CPPs have also been explored as monomers for the synthesis of novel polymers via cross-coupling[12,13] and ring-opening metathesis polymerization strategies.[14] However, despite tremendous strides in CPP-based materials

chemistry, the initial vision of using CPPs for the bottom-up synthesis of well-defined nanotubular structures has yet to be fully realized. For example, CPP-templated carbon nanotubes still display a distribution of diameters, chiralities, and wall thicknesses.[8] Similarly, CPP-based polymers are conformationally disordered and amorphous.

An alternative and less-explored approach to the construction of extended materials from CPPs is *via* their employment as polytopic ligands. The installation of metal-binding substituents on the CPP backbone would enable coordination chemistry approaches to CPP elongation and polymerization, leading to novel CPP-based metal complexes and extended metal–organic materials. Furthermore, through the appropriate choice of metal and ligand, it should be possible to preserve the extended π-conjugation observed in carbon nanotubes.[15,16] Ultimately, such a route may enable the construction of atomically precise metal–organic analogues of single-walled carbon nanotubes.

While the use of CPPs as topologically unique ligands is a tantalizing prospect, our current understanding of CPP-based coordination chemistry remains relatively limited. Thus far, only two metal-coordinating motifs have been established in CPPs: (1) the η^6-coordination of metals to CPP phenylene rings, and (2) the chelation of metal cations to CPP-embedded 2,2′-bipyridyl groups. Organometallic fragments such as $M(CO)_3$ (M = Cr, Mo, W)[17] and $[M(Cp)]^+$ (M = Ru)[18,19] have been shown to bind CPP phenylene rings in a face-on fashion, generating η^6-complexes. In addition, 2,2′-bipyridyl-embedded CPPs have been shown to chelate first- and second-row transition metals ($M = Fe^{2+}$, Pd^{2+}).[20,21] In the case of Pd^{2+}, a nanohoop dimer was crystallized, with each Pd^{2+} center bound by two separate bipyridyl-embedded CPP rings.[20] Due to steric clash between the *ortho*-hydrogens of the coordinated bipyridine ligands, the Pd^{2+} center displays a distorted square-planar geometry and the CPP rings adopt a trans conformation. This steric strain

may make it difficult to achieve extended tubular structures with bipyridine-based CPP motifs alone.

Taken together, these prior examples have established CPPs and their substituted derivatives as competent ligands. However, the continued exploration of new polytopic ligand designs is needed to realize the full promise of CPP-based metal–organic materials. Here, we illustrate how nucleophilic aromatic substitution (S_NAr) reactions can be leveraged to rapidly introduce donor atoms (–OR, –SR) onto polyfluorinated [12]CPP rings. A simple two-step S_NAr alkoxylation–deprotection sequence produces polytopic, catechol-based nanohoop ligands in excellent overall yields (67–79 %). Finally, we show that catechol-containing CPPs readily bind transition metals such as ruthenium, generating discrete di- and hexa-ruthenium CPP complexes. The new chemistry reported here represents an important step towards realizing the longstanding goal of forming well-defined extended structures from CPPs.

2.2 Results and Discussion

2.2.1 Alkoxylation and Thiolation of Polyfluorinated Arenes

Established methods for the late-stage modification of unfunctionalized CPPs are rare, and often suffer from limited scope and low yields.[17,22] We hypothesized that a nucleophilic aromatic substitution strategy to derivatize fluorinated CPPs may be more effective, as it circumvents the site-selectivity challenges associated with the modification of unfunctionalized CPPs. Such a route is particularly attractive given the plethora of polyfluorinated CPPs available. Cycloparaphenylenes bearing fluorine substituents are one of the most widely reported classes of functionalized CPPs (**Fig. 2.1a**).[23–27] This is largely due to the chemical inertness of the C–F bonds, which provide minimal complications during the challenging macrocycle formation and

aromatization stages of CPP synthesis. Fluorine substituents have proven amenable to both the reductive aromatization[24–26] and metal-mediated reductive elimination routes[23,27] for synthesizing CPPs, the latter of which has been demonstrated with both Ni- and Au-based macrocyclic precursors.

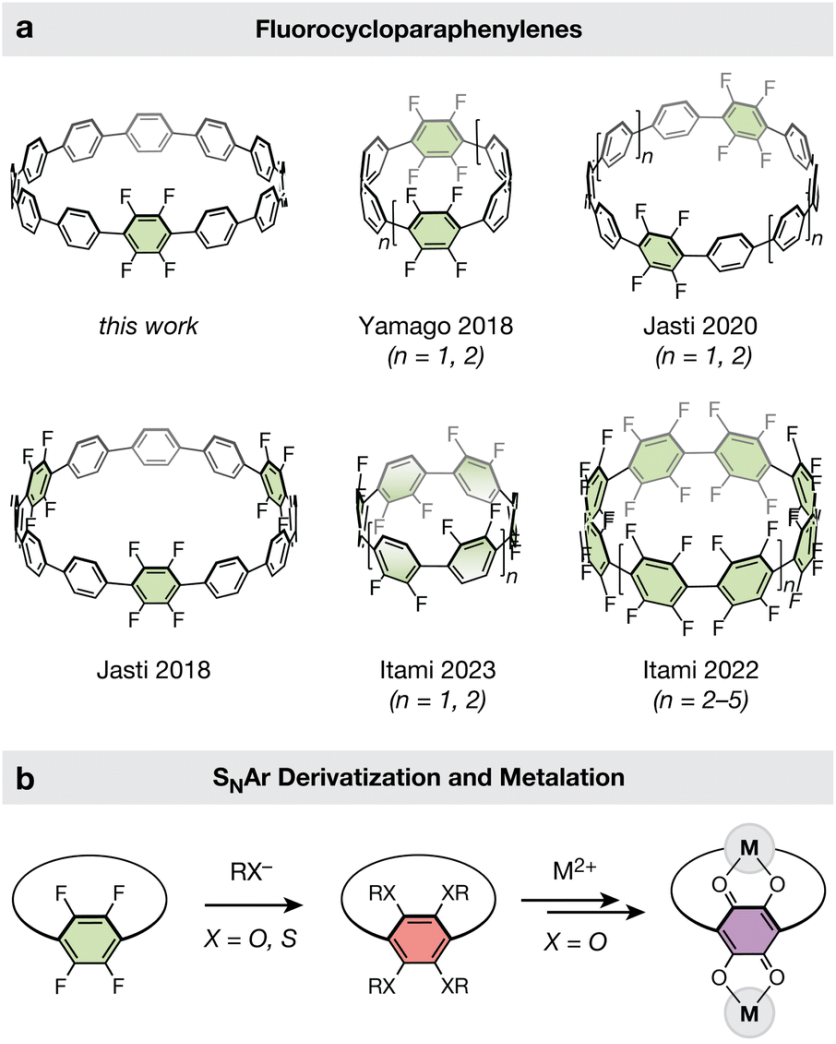

Figure 2.1. (a) Fluorine-substituted CPPs previously reported in the literature alongside the tetrafluorinated [12]CPP reported in this work. **(b)** Cartoon representation of the late-state modification of a fluorinated CPP via nucleophilic aromatic substitution with O-, S-, and N-based nucleophiles.

Itami and coworkers recently demonstrated that S_NAr can be an effective tool for the late-stage modification of half-fluorinated CPPs using pyrrolide nucleophiles.[23] We hypothesized that fluorinated CPPs could be similarly functionalized with oxygen and sulfur-based nucleophiles (**Fig. 2.1b**), affording rapid access to a diversity of new CPPs bearing alkoxy and alkylthiol substituents. Alkoxy-functionalized CPPs are poorly represented in the literature due to the challenge of *de-novo* synthesis with alkoxy-containing precursors,[28–30] and no sulfur-bearing CPPs have been reported to date.

To achieve high overall yields in polysubstitution reactions, near-quantitative yield must be observed for each individual substitution event. Because there are only a few literature reports of the exhaustive substitution of polyfluoroarenes with methoxide nucleophiles,[31–34] we first optimized our synthetic conditions on a model tetrafluorinated terphenyl substrate. The tetramethoxylation of 1,2,4,5-tetrafluoro-3,6-diphenylbenzene using sodium methoxide was carefully optimized to minimize the presence of partially substituted intermediates and reaction byproducts. While both *N,N'*-dimethyl-2-imidazolidinone (DMI) and *N*-methyl-2-pyrrolidone (NMP) were found to be acceptable solvents for this reaction, solvent mixtures containing MeOH severely hindered reaction progress. Aliquots of this reaction collected over 48 h and monitored by GC-MS showed that the percentage of the desired tetramethoyxylated product in the reaction mixture reached a maximum at 16 h at 80 °C. At higher temperatures, we observed partial *in situ* demethylation of the methoxy substituents, resulting in reaction byproducts containing one hydroxyl group. With our final optimized conditions (16 equiv NaOMe, 80 °C, 16 h, neat NMP or DMI), the desired 1,2,4,5-tetramethoxy-3,6-diphenylbenzene could be obtained in 86% yield.

2.2.2 Late-Stage Modification of Polyfluorinated [12]CPP

To test whether our optimized S_NAr conditions would translate to a cyclic system, we first synthesized a new tetrafluorinated [12]CPP, **4F-CPP**, which bears all four fluorine substituents on a single phenylene unit (**Scheme 2.1**).

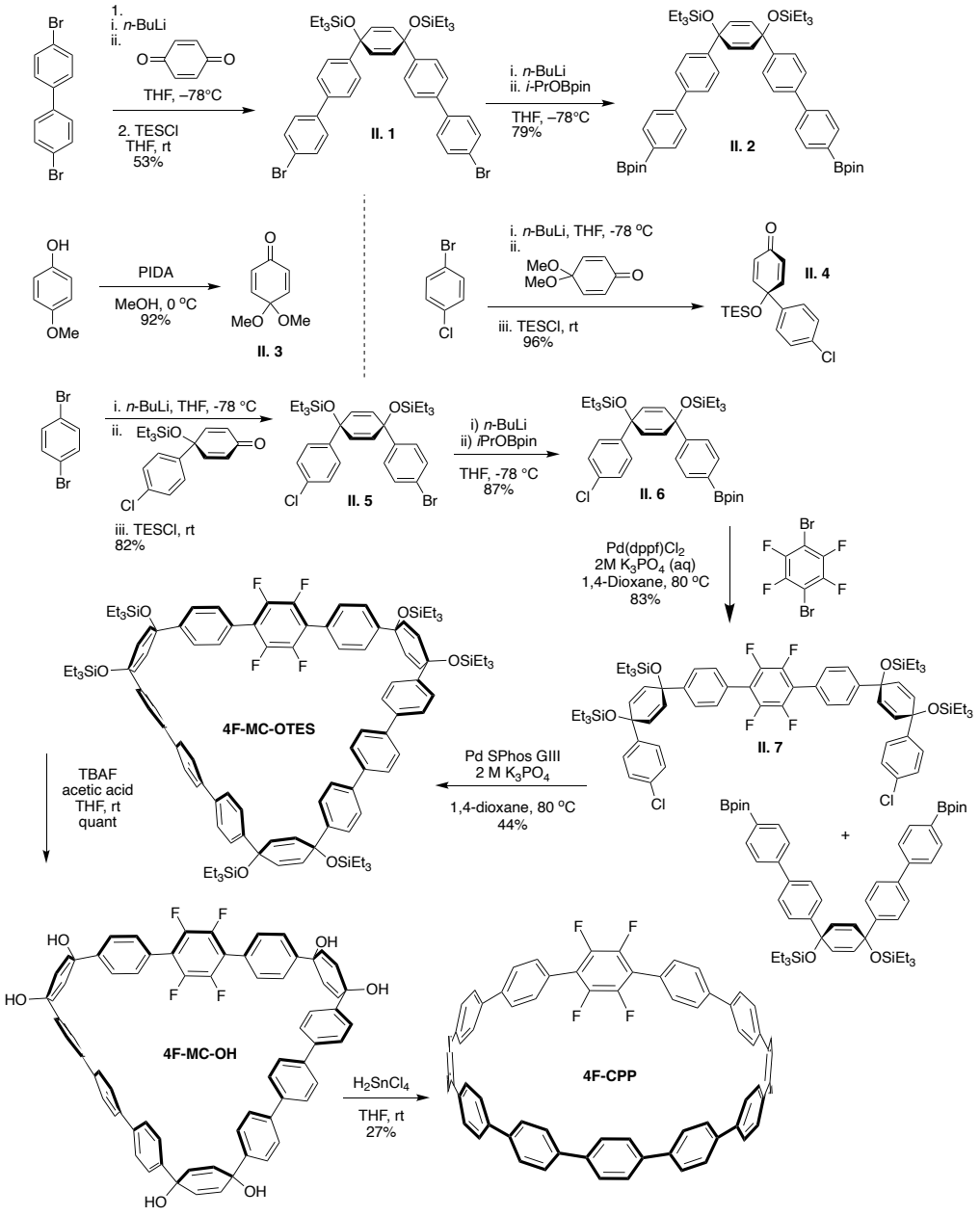

Scheme 2.1. Synthesis of the tetrafluorinated [12]CPP, **4F-CPP**.

4F-CPP was prepared using the same reductive aromatization approach employed by Jasti and coworkers in the synthesis of prior fluorinated CPPs such as **12F-CPP**.[25,26] Suzuki-Miyaura cross-coupling between two curved precursors produced the intermediate fluorinated macrocycle, **4F-MC-OTES**, with a yield of 44%. Subsequent desilylation with tetrabutylammonium fluoride (TBAF) and acetic acid followed by reductive aromatization using H_2SnCl_4 gave the desired molecule, **4F-CPP** (27% yield over both steps).

Excitingly, treating a solution of **4F-CPP** in DMI with 16 equiv sodium methoxide at 80 ˚C in a nitrogen-filled glovebox produced the desired **4MeO-CPP** in 87% yield (**Fig. 2.2a**).

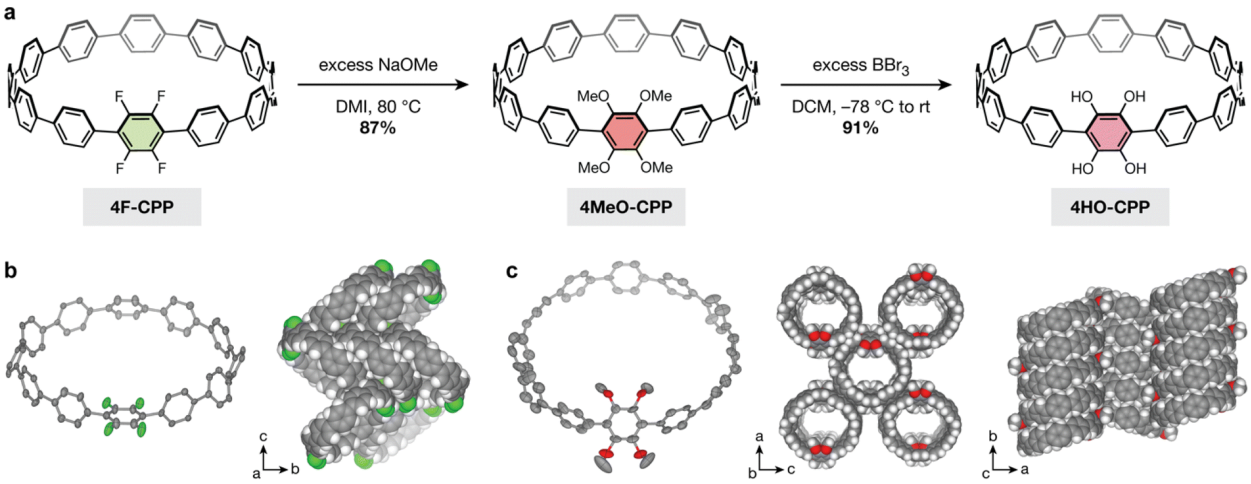

Figure 2.2. (a) Synthesis of the dicatechol-substituted [12]CPP, **4HO-CPP**, via nucleophilic aromatic substitution followed by demethylation. (b) Single crystal structure and packing of **4F-CPP;** the tetrafluorophenylene unit is disordered over two positions, as can be seen in the packing diagram. (c) Single crystal structure and packing of **4MeO-CPP**. For all structures, thermal ellipsoids are drawn at the 50% level. Solvent molecules and select protons are omitted for clarity. F, O, C and H atoms are represented by green, red, gray, and white, respectively.

Successful methoxylation was confirmed by ^{1}H NMR, ^{13}C NMR, and high-resolution mass spectrometry. In addition, single crystals of both **4F-CPP** and **4MeO-CPP** suitable for X-ray

crystallography were obtained by vapor diffusion of *n*-heptane into a solution of the CPP in trichloroethylene (**Fig. 2.2c**).

The single-crystal structure of **4F-CPP** reveals a herringbone packing structure with no individually resolved solvent molecules. The position of the tetrafluorophenylene unit within the CPP ring is disordered, giving rise to eight fluorinated positions, each with a 50% fluorine and proton site occupancy. While this herringbone packing matches the packing structure of unsubstituted [12]CPP,[35] it stands in contrast to the tubular packing observed in more heavily fluorinated CPPs, which can be driven by noncovalent C–H···F hydrogen bonding and arene–perfluoroarene interactions.[26]

Unexpectedly, and unlike **4F-CPP**, the single-crystal structure of **4MeO-CPP** reveals a nearly tubular packing structure with one trichloroethylene molecule per CPP. Additional solvent embedded within each ring is highly disordered and could not be individually resolved. To minimize steric interactions between *ortho* substituents, the dihedral angles between the tetramethoxyphenylene unit and the adjacent phenylene rings average 51(7)°.
This value is much larger than the values observed between the bare phenylenes ($\angle_{avg}$ = 28(14)˚) and between the phenylenes in unsubstituted [12]CPP ($\angle_{avg}$ = 28(15)˚).[35]

In order to employ our tetrasubstituted CPP as a ligand, it is necessary to remove the methyl groups to yield free catechol moieties. Deprotection of the aryl methyl ethers was successfully carried out by treating **4MeO-CPP** with excess boron tribromide, yielding the desired dicatechol-substituted [12]CPP, **4HO-CPP**, in 91% yield (79% over two steps from **4F-CPP**). Due to the redox-active nature of catechols, the workup for this reaction was performed inside a nitrogen-filled glovebox to prevent ligand oxidation. The removal of all methyl groups was confirmed by the disappearance of the resonance at 3.50 ppm in the ^{1}H NMR spectrum. Peaks at *m*/*z* = 975.3471

and 973.3321 were observed by high-resolution ESI-MS immediately following removal of **4HO-CPP** from the glovebox. The first of these peaks is consistent with **4HO-CPP** in the as-synthesized form (calculated m/z = 975.3469 for $[M-H]^-$), while the second peak corresponds to the oxidation of the dicatechol-substituted phenylene units to the corresponding 2,5-dihydroxy-1,4-benzoquinone form (calculated m/z = 973.3312 for $[M-H]^-$).

In order to demonstrate that our S_NAr method can be extended to more heavily fluorinated CPPs, we next carried out S_NAr on a dodecafluorinated [12]CPP, **12F-CPP** (**Fig. 2.3a**). The gram-scale synthesis of **12F-CPP** was previously reported by Jasti and coworkers.[25,26] The reaction of **12F-CPP** with excess sodium methoxide in NMP was carried out at 80 ˚C in a nitrogen-filled glovebox. The desired dodecamethoxy-substituted product, **12MeO-CPP**, was recovered in good yield (**Fig. 2.3a**) and fully characterized by ^{1}H NMR, ^{13}C NMR, and high-resolution mass spectrometry.

We note that, under the reaction conditions required to achieve complete methoxylation of the **12F-CPP** substrate, it is difficult to avoid partial demethylation of the methoxy groups into hydroxyl groups. This can be reversed by subsequent addition of methyl iodide to give pure **12MeO-CPP** in 86% yield. Because the fully deprotected **12HO-CPP** is our desired target, we typically proceeded forward without the addition of methyl iodide. In this case, if both **12MeO-CPP** as well as partially demethylated species are taken into account, then the overall yield increases to 97%. Diffraction-quality single crystals of **12MeO-CPP** were grown *via* slow evaporation out of a mixture of acetone and MeOH (Fig.2.3b). **12MeO-CPP** adopts a herringbone-type packing with two acetone molecules embedded within each CPP. The difference in CPP packing between **12MeO-CPP** and **4MeO-CPP** suggests that the tubular packing in **4MeO-CPP** is not a result of electronic effects from the methoxy groups, but may be a result of either the lower-

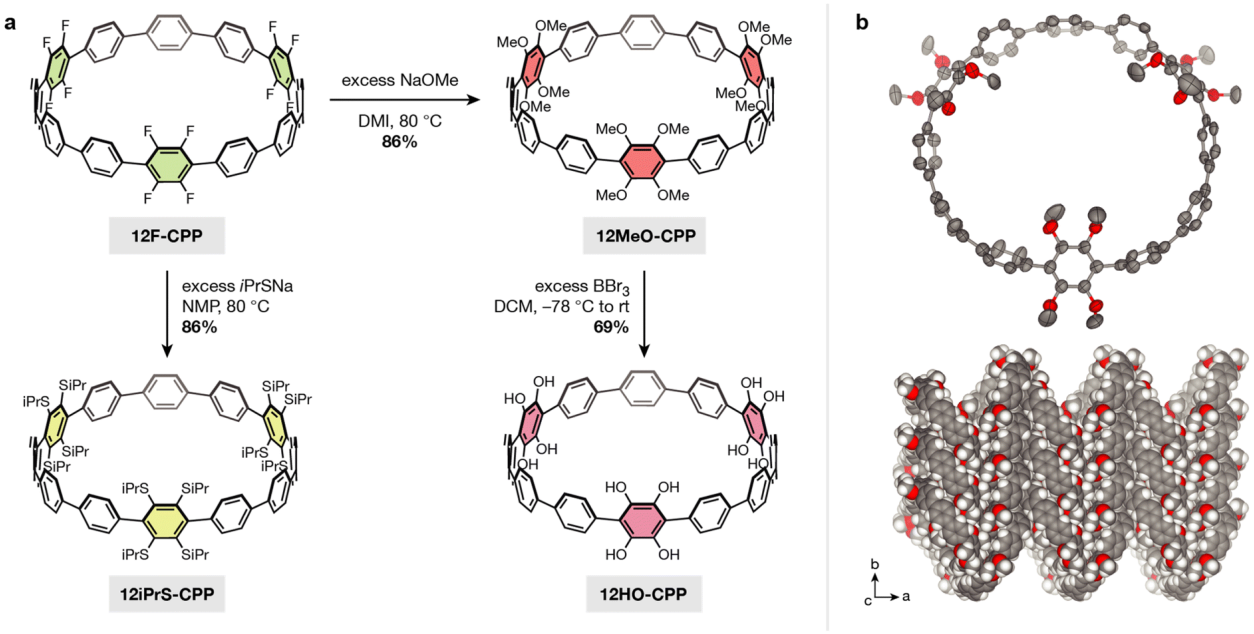

Figure 2.3. (a) Synthesis of methoxy and 2-propanethiol-substituted [12]CPPs via nucleophilic aromatic substitution. The methoxy substituents can be deprotected to yield the corresponding free catechols. (b) Single crystal structure and packing of **12MeO-CPP**. Thermal ellipsoids are drawn at the 50% level. Protons and solvent molecules are omitted for clarity. O and C atoms are represented by red and grey, respectively.

symmetry steric profile of the molecule or solvent-driven intermolecular interactions. Both the tubular and herringbone packing observed in **4MeO-CPP** and **12MeO-CPP**, respectively, differ from the brick-wall style packing observed in dodecamethoxy-substituted [6]CPP, which is the only other methoxy-substituted CPP with a reported crystal structure.[30] With regard to torsion in the CPP backbone, the three methoxy-substituted phenylenes in **12MeO-CPP** display a wide range of dihedral angles relative to the adjacent phenylenes, measuring 47(6)˚, 51(7)˚, and 69(9)˚, respectively. The remaining unsubstituted phenylene units display much smaller dihedral angles relative to each other ($\angle_{avg}$ = 29(4)˚), well within the range observed in unsubstituted [12]CPP.

Reacting **12MeO-CPP** with excess boron tribromide afforded **12HO-CPP**, a [12]CPP containing six catechol moieties, in 69% yield (67% over two steps from **12F-CPP**).The

compound is extremely sensitive to aerial oxidation, and partial oxidation was observed even when the workup was performed under a nitrogen atmosphere. As such, resolving the peak multiplicity in the ^{1}H NMR was not possible (see SI for details). However, the disappearance of the methoxy CH_3 protons at 3.53 ppm unequivocally confirms the removal of all methyl substituents. High-resolution ESI-MS of **12HO-CPP** immediately following removal from the glovebox showed prominent peaks at *m/z* = 1143.2779 and 1141.2622. The first of these peaks is consistent with the positively charged potassium adduct of **12HO-CPP** in the as-synthesized state (calculated *m/z* = 1143.2777 for $[M+K]^+$), while the second peak corresponds to the loss of two protons induced by the rapid oxidation of one of the dicatechol-substituted phenylene units (calculated *m/z* = 1141.2621 for $[M+K]^+$). Similar oxidation under ESI-MS conditions was observed with **4HO-CPP** .

Given the success of S_NAr on fluorinated CPPs with methoxide nucleophiles, we hypothesized that similar reactions could be replicated with stronger sulfur-based nucleophiles. Indeed, the reaction of **12F-CPP** with excess sodium 2-propanethiolate in DMI at 80 ˚C afforded the corresponding [12]CPP with twelve isopropylthiol substituents, **12iPrS-CPP** (**Fig. 2.3a**). The product was recovered in 86% yield and fully characterized by ^{1}H NMR, ^{13}C NMR, and high-resolution ESI-MS (see SI for details). To our knowledge, **12iPrS-CPP** represents the first CPP functionalized with alkylthiol substituents.

2.2.3 Coordination Chemistry of Polycatechol CPP Ligands

As prototypical "redox non-innocent" ligands, catecholates readily traverse multiple redox states (catecholate, *o*-semiquinone, and *o*-quinone) when bound to metal cations.[36] The rich redox behavior of metal–catecholates has been shown to confer attractive catalytic, magnetic, and electronic properties,[37–39] making them exciting building blocks for metal–organic materials. In

addition to unusual metal–organic architectures, the unique cyclic topology of polycatechol CPP ligands also provides an opportunity to study how strained, curved π-systems alter the redox behavior and metal-binding ability of catechol groups. Before investigating the more complex cyclic CPP systems, we first focused our attention on a simpler linear terphenyl model ligand, 1,2,4,5-tetrahydroxy-3,6-diphenylbenzene (H_4Ph_2dhbq) (**Fig. 2.4a**). The Xiao lab has previously studied the coordination chemistry of H_4Ph_2dhbq and its oxidized derivative, 2,5-dihydroxy-3,6-dipheny-1,4-benzoquinone (H_2Ph_2dhbq), in the context of 1D iron chains.[40] Here, we have focused our studies on ruthenium, as half-sandwich Ru(II) arene complexes are known to bind R_2dhbq^{2-} ligands to form stable and soluble diamagnetic complexes that are readily characterized by ^1H NMR.[41–44]

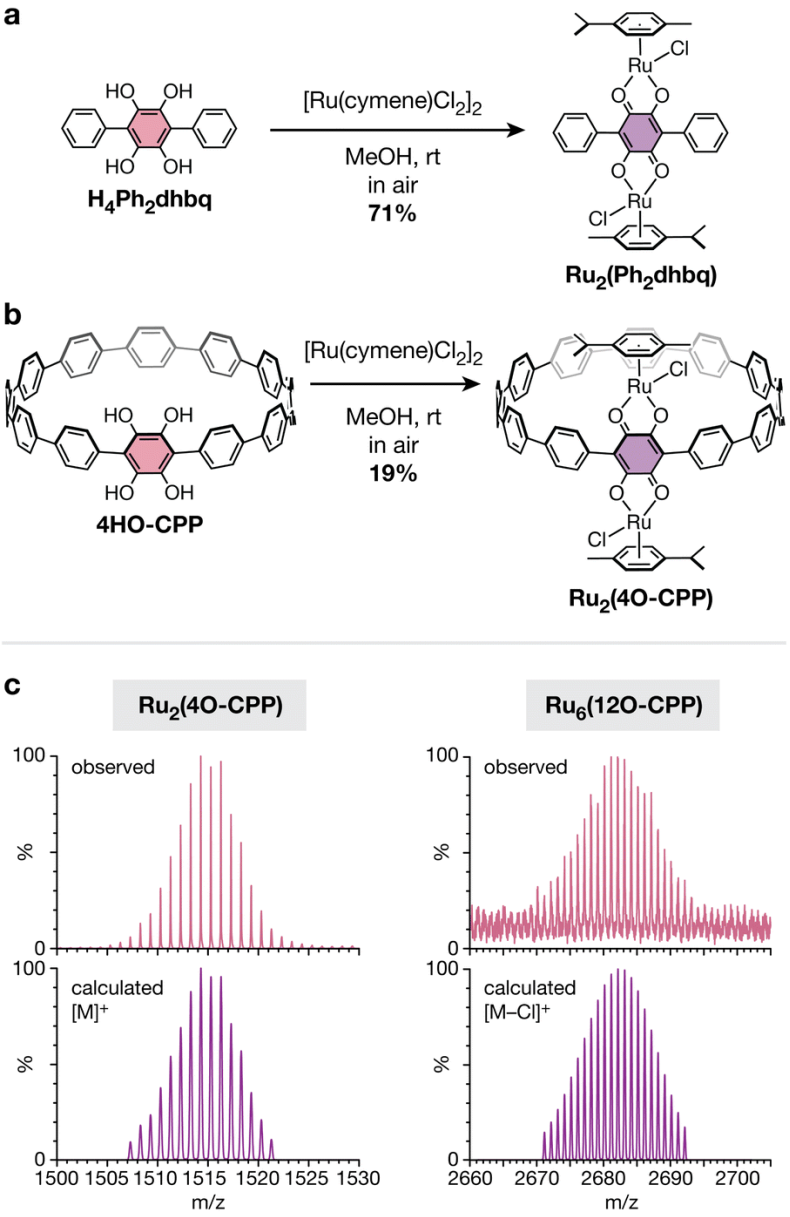

Figure 2.4. (a) Synthesis of the diruthenium complex **Ru_2(Ph$_2$dhbq)** from the reduced form of the model ligand, H_4Ph_2dhbq. (b) Synthesis of the diruthenium complex **Ru_2(4O-CPP)** from the ligand **4HO-CPP**. (**c**) Observed versus simulated high-resolution MALDI-TOF spectra of the polyruthenium complexes **Ru_2(4O-CPP)** and **Ru_6(12O-CPP)**.

While the reaction between Ru_2(*p*-cymene)$_2Cl_4$ and H_2Ph_2dhbq has been reported to yield the diruthenium complex Ru_2(*p*-cymene)$_2$(Ph$_2$dhbq)Cl_2 (**Ru_2(Ph$_2$dhbq)**),[44] it was not known if similar reactivity would be observed with the fully reduced, dicatechol form of the ligand.

Excitingly, we found that the reaction between H_4Ph_2dhbq and $Ru_2(p\text{-cymene})_2Cl_4$ in air produced the identical diruthenium complex in comparable yields (**Fig. 2.4a**). The ^1H NMR and ESI-MS spectra matched the previously reported data for this compound. In addition, single crystals suitable for X-ray diffraction were obtained for the first time through slow diffusion of MeOH into DCM, unambiguously confirming that the desired bimetallic product was obtained (**Fig. 2.5a**).

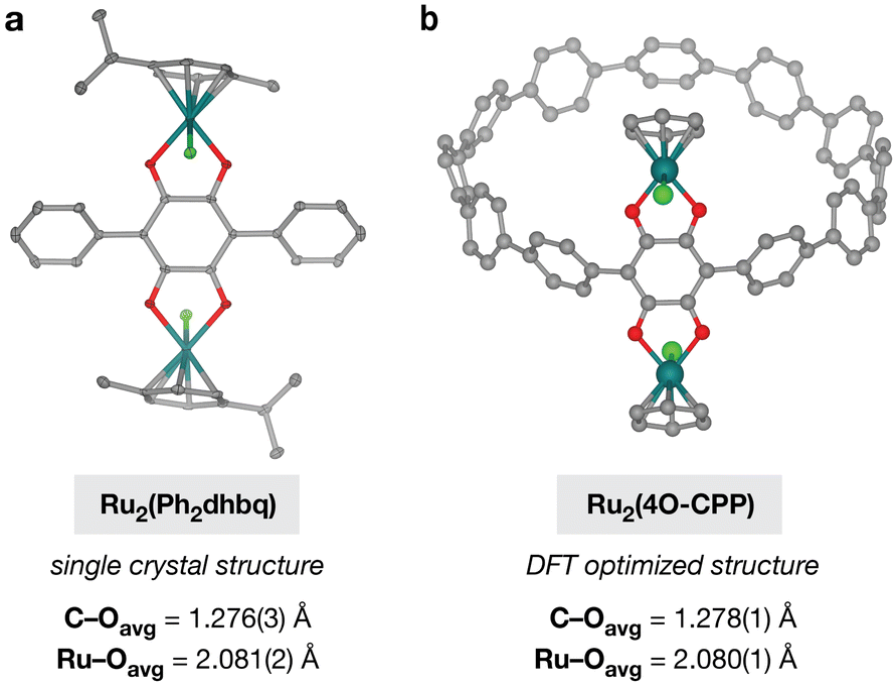

Figure. 2.5 (a) Average C–O and Ru–O bond lengths observed in the single crystal structure of **$Ru_2(Ph_2dhbq)$**. Thermal ellipsoids are rendered at the 50% probability level. (b) Average C–O and Ru–O bond lengths observed in the optimized structure of **Ru_2(4O-CPP)** obtained *via* DFT using the B3LYP hybrid functional with a split basis set of LANL2DZ for Ru and 6-31G* for all other atoms. η^6-Cymene ligands on Ru were modeled as η^6-benzene. For both parts, Ru, Cl, O, and C atoms are represented by dark green, light green, red, and gray, respectively, and protons are omitted for clarity.

After confirming that the linear H_4Ph_2dhbq ligand undergoes successful *in situ* oxidation and Ru(ii) metalation, we next turned our attention to the cyclic analogue, **4HO-CPP**. The slow

diffusion of air into methanolic solutions of **4HO-CPP** and excess [Ru(*p*-cymene)Cl_2]$_2$ produced a mixture of products from which the desired compound, Ru_2(*p*-cymene)$_2$(4O-CPP)Cl_2 (**Ru_2(4O-CPP)**,**Fig. 2.4b)** could be purified and isolated in 19% yield (see SI for details). The use of MeOH as the solvent appeared to be critical. Alternative solvent systems containing solvents such as dimethylformamide (DMF) and $CHCl_3$ led to either worse yields or no reaction. The lower yields observed with **4HO-CPP** relative to H_4Ph_2dhbq suggest that catechols in curved π-systems may have more complex redox behavior than their linear counterparts. However, this difference in yield may also be exacerbated by the smaller reaction scale and need for chromatographic purification of **Ru_2(4O-CPP)**. More work is needed to fully understand these differences, and studies along this vein are underway.

The ^{1}H NMR spectrum of **Ru_2(4O-CPP)** confirms its diamagnetic nature suggesting that, as in the model complex, the metals centers are in the +2 oxidation state and the **4HO-CPP** ligand is oxidized to the 2,5-dihydroxy-1,4-benzoquinone form and doubly deprotonated (4O-CPP^{2-}). The *m/z* value and corresponding isotopic envelope observed by high-resolution MALDI-TOF is 1514.2805, consistent with the predicted value (*m/z:* 1514.2925) and isotopic envelope for $[M]^+$ (**Fig. 2.4c**).

While exhaustive metalation studies with **12HO-CPP** were hindered by the poor solubility and oxidative sensitivity of the ligand, preliminary experiments suggest that **12HO-CPP** can be similarly metalated to achieve a hexaruthenium CPP complex. A mixture of **12HO-CPP** and excess [Ru(*p*-cymene)Cl_2]$_2$ was dissolved in 1 : 1 DMF : MeOH and stirred in air for 48 h at room temperature. After solvent removal and MeOH washing, a dark red solid with moderate solubility in chlorinated organic solvents was obtained in yields of up to 54%. The formation of the desired complex, Ru_6(*p*-cymene)$_6$(12O-CPP)Cl_6 (**Ru_6(12O-CPP)**), was confirmed *via* high-resolution

MALDI-TOF (Fig. 2.4c). The resonances in the ^{1}H NMR appear consistent with the formation of **Ru_6(12O-CPP)**. However, the peaks are broad and poorly resolved, preventing the accurate assessment of peak integrations and multiplicities. The observed peak broadness may be due to hindered rotation of the *p*-cymene ligands and CPP phenylene rings, as the hexaruthenium complex is significantly more sterically congested than **Ru_2(4O-CPP)**. Similar peak broadening has been observed in other CPPs that are densely decorated with bulky substituents.[23] Variable temperature ^{1}H NMR experiments in tetrachloroethane-d_2 show that peak shape improves significantly with increasing temperature, however the peaks and their multiplicities are still not fully resolved at 120 °C.

2.2.4 DFT Structural Analysis

As we were unable to isolate single crystals of the Ru–CPP complexes for structural analysis by X-ray crystallography, geometry optimizations of **Ru_2(4O-CPP)** and **Ru_6(12O-CPP)** were performed using density functional theory (DFT). All calculations were carried out at the B3LYP level of theory with the LANL2DZ basis set on Ru atoms and 6-31G* basis on all other atoms. For the ease of calculations, the η^6-cymene ligands were modeled as η^6-benzene.

Analysis of multiple structural isomers of **Ru_2(4O-CPP)** suggests that the lowest energy isomer contains two Cl atoms in a *trans* configuration on the Ru centers **(Fig. 2.5b).** This is consistent with the single crystal structure of **Ru_2(Ph_2dhbq)** where the two Cl atoms are also oriented in the *trans* configuration **(Fig. 2.5a).**

Comparison between the lowest-energy DFT optimized structure of **Ru_2(4O-CPP)** and the single crystal structure of **Ru_2(Ph_2dhbq)** shows that the bond lengths match closely. The average C–O bond lengths in the optimized structure of **Ru_2(4O-CPP)** are 1.278(1) Å, very similar to the C–O bond lengths of 1.274(3) and 1.278(3) Å observed in the single crystal structure

of **Ru_2(Ph$_2$dhbq)**. In addition, the optimized structure of **Ru_2(4O-CPP)** displays an average Ru–O bond length of 2.080(1) Å, very similar to the bond lengths of 2.070(2) and 2.092(2) Å observed in the single crystal structure of **Ru_2(Ph$_2$dhbq)**.

2.3 Conclusion

In conclusion, we have shown that nucleophilic aromatic substitution is a highly efficient strategy for the late-stage diversification of fluorinated CPPs and provides a route for the synthesis of new CPP-based ligand platforms. Both alkoxide and alkylthiolate nucleophiles can be used, providing rapid access to electron-rich, densely substituted CPP rings that cannot be easily obtained through existing methods. An important outcome of our S_NAr approach is the ability to convert the current repertoire of fluorinated CPPs into a diverse library of redox-active and topologically unique polycatechol ligands. The catechol-substituted CPPs reported here, **4HO-CPP** and **12HO-CPP**, can be readily synthesized from their fluorinated counterparts in just two steps with excellent overall yields (up to 79%). In addition to their interesting coordination chemistry, polycatechol nanohoops are also versatile partners for dynamic covalent chemistry, enabling the construction of new CPP-based organic polymers and covalent organic frameworks.

Both **4HO-CPP** and **12HO-CPP** can be metalated with half-sandwich Ru(II) arene fragments in the presence of air to produce well-defined dinuclear and hexanuclear compounds, respectively. In principle, it should be possible to replace the chloride bound to each Ru(II) center with other ligands.[45] As such, these compounds represent the first examples of multimetallic CPP complexes that are primed for further extension. Given the widespread use of dinuclear arene ruthenium complexes in the construction of metallacycles and metallaprisms,[41–43] we anticipate that these metalated CPP complexes will serve as an exciting new synthon in supramolecular chemistry.

Finally, the preliminary metalation studies outlined here have already revealed intriguing similarities and differences between linear and curved polycatechol ligands. The metalation of **4HO-CPP** proceeds in significantly lower yields than the linear analogue, suggesting that curvature may induce more complicated redox behavior and/or coordination chemistry. On the other hand, close analysis of DFT-optimized structures shows that the metal–dioxolene linkages in linear and curved systems display few, if any, structural differences. These structural studies are encouraging and suggest that cyclic polycatechol ligands may be amenable to forming extended structures, much like their more well-studied linear counterparts.[37] Further work to understand the coordination chemistry of polycatechol CPP ligands, particularly towards the construction of extended metal–organic architectures, is under way.

2.4 Experimental Section

2.4.1 General Experimental Details

Reagents and solvents were purchased from commercial vendors (Millipore Sigma, TCI America, Alfa Aesar, Fisher Scientific, Oakwood Chemical, Combi-Blocks) and used without further purification unless otherwise noted. Deuterated solvents were purchased from Cambridge Isotope Laboratories. Oxygen- and moisture-sensitive reactions were performed using standard Schlenk or glovebox procedures under a nitrogen atmosphere. Workups were performed in air unless otherwise specified. Silica column chromatography was conducted with Zeochem Zeoprep n60 Eco 40-63 μm silica gel. Alumina column chromatography was conducted with SorbTech basic alumina (pH 10), Act. II-III, 50-200 μm. Preparative TLC was performed using Millipore Sigma 200 μm silica gel 60 matrix F254 TLC plates. NMR spectra were acquired using 500 MHz Bruker spectrometers. 1H spectra were referenced to TMS (δ 0.00 ppm) or residual solvent peaks (CDCl3 δ 7.26 ppm, DMSO-d6 δ 2.50 ppm, and tetrachloroethane-d2 δ 6.00 ppm). 13C NMR

spectra were referenced to residual CDCl3 (δ 77.16 ppm). 19F NMR spectra were indirectly referenced to CFCl3 (δ 0.00 ppm) using a hexafluorobenzene standard (δ –164.9 ppm) or via the Bruker TopSpin 3.5 software suite. Solution-phase UV-vis spectra were collected on an Agilent Cary 100 UV-vis or Shimadzu UV3600i Plus UV-vis-NIR spectrophotometer using a 1 cm quartz cuvette. Standard ESI-MS data were collected on a Bruker Esquire Ion Trap mass spectrometer in positive ion mode. GC-MS data were collected on an Agilent 9573 mass spectrometer in positive ion mode. High-resolution ESI-MS data for 4MeO-CPP, 12MeO-CPP, 12iPrS-CPP, 12HO-CPP, Ru2(Ph2dhbq), and Ru2(4O-CPP) were collected on an LTQ-Orbitrap XL mass spectrometer in positive ion mode. High-resolution ESI-MS data for 4HO-CPP was collected on the same instrument in negative ion mode. High-resolution MALDI-TOF data for 4F-MC-OTES and 4F-CPP were collected on a Bruker Autoflex Speed LRF mass spectrometer in positive ion mode. High resolution MALDI-TOF data for Ru2(4O-CPP) and Ru6(12O-CPP) were collected on a Waters Synapt XS mass spectrometer in positive ion mode. All samples were prepared in DCM with trans-2-[3-(4-tert-butylphenyl)-2- methyl-2-propenylidene]malononitrile (DCTB) as a matrix.

2.4.2 Synthetic Procedures

The starting material, **12F-CPP**, was prepared according to published methods by Jasti and coworkers.[25,46] The intermediates used in the preparation of **4F-CPP**, **S1** and **S2**, were prepared according to previously published methods by Jasti and coworkers. The terphenyl model ligand, **H_4Ph_2dhbq**, was prepared according to published methods by Xiao and coworkers.[47]

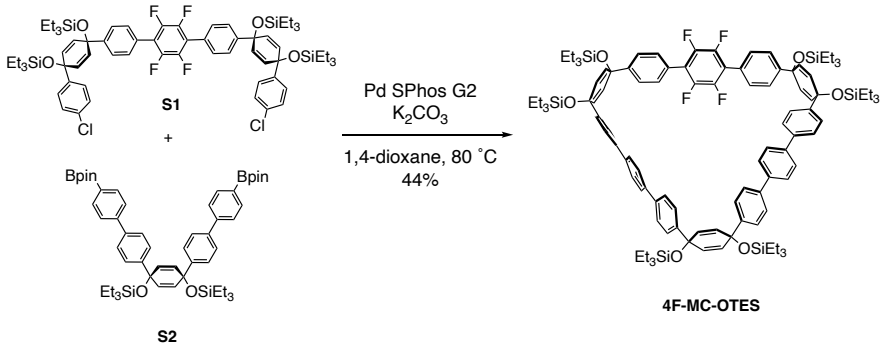

Synthesis of 4F-MC-OTES. To a flame-dried 1 L round-bottom flask equipped with a stir bar was added S1 (0.6 g, 0.5 mmol, 1.0 equiv), **S2** (0.493 g, 0.55 mmol, 1.1 equiv), and Pd SPhos G3 (78 mg, 0.1 mmol, 0.2 equiv). The flask was placed under high vac for one hour, and subsequently evacuated and backfilled with nitrogen three times. Starting materials were dissolved in 1,4-dioxane (333 mL) and the mixture was sparged with nitrogen for 30 minutes. The mixture was then lowered into a preheated oil bath at 80 ˚C and allowed to stir for 30 minutes. A 2M aqueous solution of K3PO4 (33 mL) that had been sparged for 30 minutes prior was added dropwise. The solution was allowed to stir at 80 ˚C overnight. In the morning, the solution was cooled to room temperature, poured over a fritted funnel filled with celite and sodium sulfate, and eluted with ethyl acetate. The eluent was collected, and the solvent was removed via rotary evaporation. The resulting brown oil was extracted with ethyl acetate (3 × 100 mL), washed with water (3 × 100 mL), brine (1 × 100 mL), and finally dried over sodium sulfate. After removal of sodium sulfate and solvent, the crude oil was dissolved in DCM, adsorbed onto silica, and purified via silica column chromatography from 0-100% DCM in hexanes. Concentration of fractions afforded **4FMC-OTES** as an off-white solid (0.28 g, 31%).

1H NMR (500 MHz, CDCl3) δ 7.67 (s, 8H), 7.58 (d, J = 8.4 Hz, 8H), 7.52 (d, J = 8.5 Hz, 4H), 7.49–7.41 (m, 12H), 6.09 (d, J = 10.2 Hz, 4H), 6.06–6.01 (m, 8H), 0.97 (td, J = 7.9, 3.8 Hz, 54H),

0.70-0.62 (m, 36H). 13C{ 1H} NMR (126 MHz, CDCl3) δ 139.66, 131.89, 130.13, 127.48, 126.86, 126.83, 126.52, 126.25, 7.24, 7.22, 7.21, 6.66, 6.62. 19F NMR (471 MHz, CDCl3) δ –144.37 (s). HRMS (MALDI) m/z: [M]+ calculated for C108H134F4O6Si6, 1770.8732; found, 1770.8672.

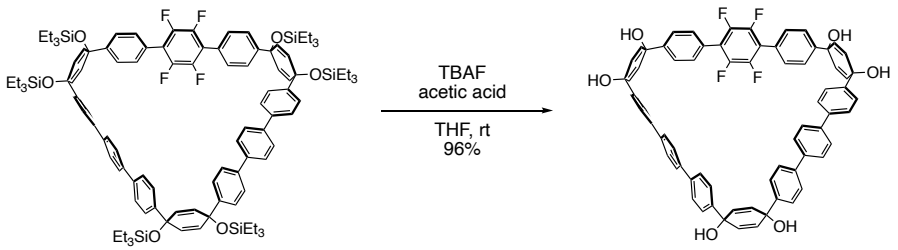

Synthesis of S4. To a flame-dried 250 mL round bottom flask equipped with a stir bar was added **4F-MC-OTES** (0.54 g, 0.305 mmol, 1.0 equiv). This was placed under high vac for an hour and subsequently dissolved in tetrahydrofuran (anhydrous/degassed; 101 mL), resulting in a clear solution. Glacial acetic acid (0.870 mL, 15.2 mmol, 50 equiv) was added quickly dropwise, followed by the slow dropwise addition of tetrabutylammonium fluoride (1M in THF, 7.62 mL, 7.62 mmol, 25 equiv). The colorless solution was allowed to stir under nitrogen overnight at room temperature. The next day, water (50 mL) was added to the reaction mixture, resulting in a white suspension, and THF was removed via rotary evaporation. The suspension was poured over a fritted vacuum funnel, resulting in **4F-MC** as a white powder that was washed with water, dried under high vac, and moved on without further purification (0.510 g, 96%).

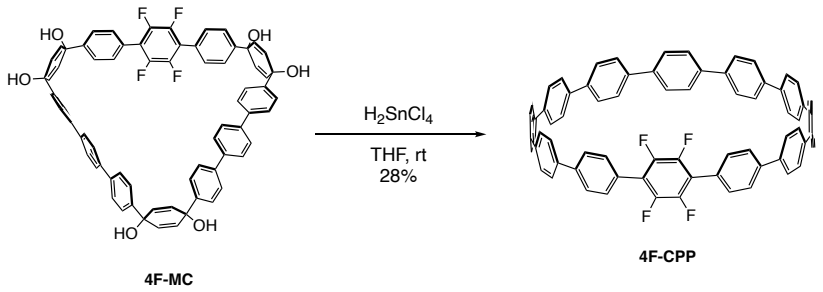

Synthesis of 4F-CPP. . To a flame-dried 100 mL round bottom flask equipped with a stir bar was added 4F-MC (0.167 g, 0.154 mmol, 1.0 equiv), which was placed under high vac for an hour and then dissolved in tetrahydrofuran (anhydrous/degassed; 26 mL, 0.006 M). In a separate 100 mL flame dried round bottom flask equipped with a stir bar was added SnCl2·2H2O (0.181 g, 0.154 mmol, 1.0 equiv) followed by concentrated aqueous HCl (0.133 mL, 0.308 mmol, 2.0 equiv). This was dissolved in tetrahydrofuran (20 mL, 0.040 M) and allowed to stir for 30 minutes at room temperature. The prepared H2SnCl4 solution (8.46 mL, 0.040 M, 2.2 equiv) was added to the **4F-MC** solution dropwise resulting in a cloudy yellow-white mixture that was allowed to stir overnight at room temperature. In the morning, a 1M aqueous NaOH solution (30 mL) was added followed by the removal of THF via rotary evaporation. The suspension was extracted with DCM (3 × 100 mL), washed with water (3 × 100 mL), brine (1 × 100 mL), and dried over sodium sulfate. After removal of the sodium sulfate and solvent, the crude yellow solid was dissolved in DCM, adsorbed onto alumina, and purified via alumina column chromatography from 0-100% DCM/hexanes. Concentration of fractions afforded **4F-CPP** as a blue-fluorescent yellow solid (36 mg, 24% yield). Single crystals suitable for X-ray diffraction were obtained by vapor diffusion of n-heptane into trichloroethylene.

1H NMR (500 MHz, CDCl3) δ 7.67–7.59 (m, 40H), 7.55 (d, J = 8.3 Hz, 4H). 13C{ 1H} NMR (126 MHz, CDCl3) δ 140.99, 138.99, 138.76, 138.62, 138.59, 138.54, 138.42, 138.32, 130.93,

127.74, 127.48, 127.44, 127.38, 127.00, 126.68. 19F NMR (471 MHz, CDCl3) δ –143.79 (s). HRMS (MALDI) m/z: [M]+ calculated for C72H44F4, 984.3379; found, 984.3390.

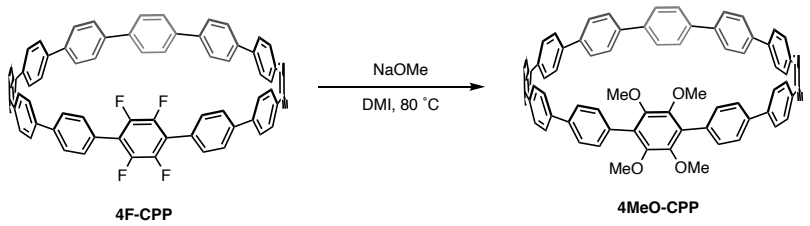

4F-CPP 4MeO-CPP

Synthesis of 4MeO-CPP. In a nitrogen-filled glovebox, 4F-CPP (22.8 mg, 23.1 μmol), sodium methoxide (20.3 mg, 0.376 mmol, 16 equiv), and DMI (0.8 mL) were divided evenly between two, 4 mL scintillation vials. The vials were sealed and stirred at 80 ˚C for 16 hr. The contents of both vials were combined. The mixture was removed from the glovebox, diluted with water (20 mL), acidified with 2M aqueous HCl (~15 drops), and the solution was verified to be acidic by pH paper. The resulting white precipitate was collected by vacuum filtration, washed with H2O, and dried under reduced pressure to give 4MeO-CPP as an off-white solid (20.7 mg, 87%). Residual DMI (ca. 5% by mass) was observed in the 1H NMR spectrum of isolated 4MeO-CPP, the contribution of which was already removed from the previously stated mass and yield. Further purification could be achieved by preparative TLC (DCM eluent) to give 4MeO-CPP as off-white solid (17.5 mg, 73%). Single crystals suitable for X-ray diffraction were obtained by vapor diffusion of n-heptane into trichloroethylene.

1H NMR (500 MHz, CDCl3) δ 7.67–7.55 (m, 40H), 7.48 (d, J = 8.5 Hz, 4H), 3.50 (s, 12H). 13C{1H} NMR (126 MHz, CDCl3) δ 147.42, 139.33, 138.83, 138.76, 138.70, 138.62, 138.59, 138.50, 138.44, 132.58, 131.43, 128.86, 127.79, 127.61, 127.56, 127.50, 127.48, 127.45, 127.43,

127.37, 127.31, 126.35, 61.18. HRMS (ESI) m/z: found 1033.4243 ([M+H] + , calc'd: 1033.4251 for C76H56O4H).

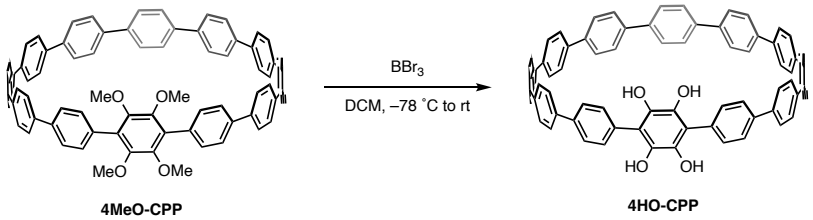

4MeO-CPP 4HO-CPP

Synthesis of 4HO-CPP. In a Schlenk flask under a nitrogen atmosphere, 4MeO-CPP (15.8 mg, 15.3 μmol) was dissolved in DCM (degassed/anhydrous, from the glovebox; 4 mL). The solution was cooled to –78 ˚C. A 1M solution of BBr3 in DCM (0.183 mL, 0.183 mmol, 12 equiv) was added dropwise via syringe. The reaction was allowed to return to room temperature over the course of 2-3 hr and stirred overnight without heating. The reaction was cooled to 0 ˚C, quenched carefully by dropwise addition of H2O (degassed; 10 mL), and stirred for 2 hr. Without exposing the mixture to air, the DCM was removed in vacuo and the flask was transferred to a nitrogen- S6 filled glovebox. Additional H2O (30 mL) was added, and the mixture was extracted with DCM (3 × 5 mL). The combined organic layers were reduced in vacuo, and the resulting solid was washed with pentane to yield 4HO-CPP as a light yellow/brown solid (13.6 mg, 91%).

1H NMR (500 MHz, CDCl3) δ 7.69–7.54 (m, 44H). 13C NMR (126 MHz, CDCl3) δ 197.23, 193.76, 154.32, 141.95, 140.99, 139.60, 139.46, 139.27, 139.14, 138.97, 138.90, 138.74, 138.64, 138.61, 138.59, 138.49, 138.40, 138.32, 132.07, 131.23, 128.84, 127.81, 127.77, 127.69, 127.63, 127.58, 127.54, 127.50, 127.48, 127.40, 127.38, 127.31, 126.93, 122.20. HRMS (ESI) m/z: found 975.3471 ([M-H] – , calc'd: 975.3469 for C72H47O4).

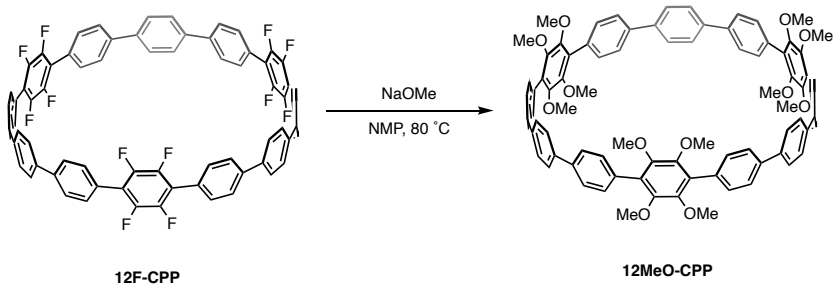

Synthesis of 12MeO-CPP. In a nitrogen-filled glovebox, 12F-CPP (99.6 mg, 88.2 μmol), sodium methoxide (229 mg, 4.25 mmol, 48 equiv), and NMP (4 mL) were divided evenly between four, 4 mL scintillation vials. All vials were sealed and stirred at 80 ˚C for 16 hr. The contents of all vials were combined. The mixture was removed from the glovebox and diluted with H2O (~20 mL). Aqueous 1M HCl (~10 mL) was added, and the solution was verified to be acidic by pH paper. The mixture was then extracted with ethyl acetate (4 × 25 mL). The combined organic layers were washed with H2O (4 × 30 mL), dried over magnesium sulfate, gravity filtered, and the solvent was removed in vacuo. The resulting solid was suspended in minimal cold MeOH, collected via vacuum filtration, and dried in vacuo to yield 12MeO-CPP as an off-white solid (109 mg, 97%). Crystals suitable for X-ray diffraction were grown by slow evaporation out of an acetone/MeOH mixture. Note: A small degree of premature demethylation may be observed in as-synthesized 12MeOCPP. While this is not of concern given our fully demethylated synthetic target, we found that any demethylation could be reversed using the following general procedure. Following heating, the vial(s) were removed from the glovebox, cooled to 0 ˚C, uncapped briefly, and methyl iodide (68 equiv) was added. Once resealed, the vial(s) were stirred at room temperature overnight. The resulting mixture was worked up as previously described, omitting the acidification step, to yield pure 12MeO-CPP as an off-white solid in 86% yield.

1H NMR (500 MHz, CDCl3) δ 7.66 (s, 12H), 7.59 (d, J = 8.7 Hz, 12H), 7.49 (d, J = 8.7 Hz, 12H), 3.53 (s, 36H). 13C{ 1H} NMR (126 MHz, CDCl3) δ 147.35, 139.25, 139.19, 132.52, 131.36, 128.77, 127.61, 126.25, 61.07. HRMS (ESI) m/z: found 1273.5077 ([M+H]+ , calc'd: 1273.5097 for C84H72O12H).

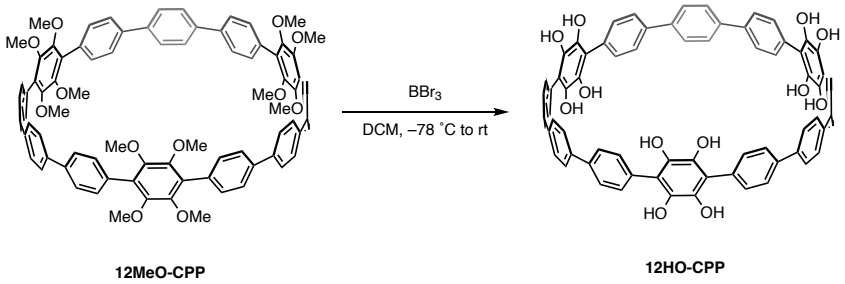

12MeO-CPP 12HO-CPP

Synthesis of 12HO-CPP. In a Schlenk flask under a nitrogen atmosphere, 12MeO-CPP (109 mg, 85.4 μmol) was dissolved in DCM (degassed/anhydrous, from the glovebox; 14 mL). The solution was cooled to –78 ˚C. A 1M solution of BBr3 in DCM (2.05 mL, 2.05 mmol, 24 equiv) was added dropwise via syringe. The reaction was allowed to return to room temperature over the course of 2-3 hr and stirred overnight without heating. The reaction was cooled to 0 ˚C, quenched carefully by dropwise addition of H2O (degassed; ~55 mL), and stirred for 2 hr. Without exposing the mixture to air, the DCM was removed in vacuo and the flask was transferred to a nitrogen-filled glovebox. The precipitate in the flask was recovered by vacuum filtration, washed with H2O, washed with a minimal amount of MeOH, and dried in vacuo to yield 12HO-CPP as an off-white/brown solid (64.9 mg, 69%). Note: workups conducted in air resulted in uncontrolled oxidation of the catechol units, as observed by significant peak broadening in the 1H NMR; this oxidation could be partially reversed through reaction with sodium dithionite, however the peaks were significantly less well resolved than for 12HO-CPP worked up under a nitrogen atmosphere.

1H NMR (500 MHz, DMSO-d6) δ 7.80 (br), 7.70 (br), 7.58 (br). HRMS (ESI) m/z: found 1143.2779 ([M+K] + , calc'd: 1143.2777 for C72H48O12K). 13C NMR could not be obtained due to poor solubility.

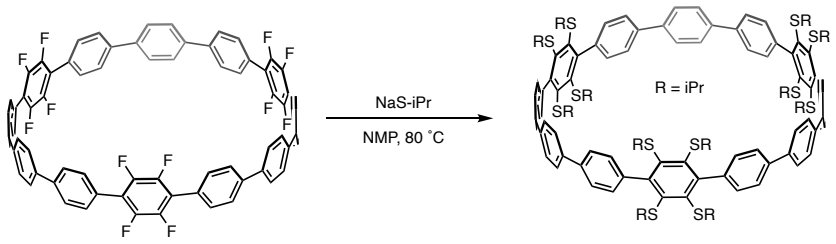

12F-CPP 12iPrS-CPP

Synthesis of 12iPrS-CPP. An oven-dried Schlenk flask under a nitrogen atmosphere was charged with 12F-CPP (20.0 mg, 17.7 μmol) and NMP (anhydrous/degassed, from the glovebox; 1.5 mL). Under nitrogen, sodium 2-propanethiolate (68.2 mg, 695 μmol, 39 equiv) was added and the reaction was stirred at 80 ˚C for 12 hr. The reaction was diluted with H2O (25 mL) and the resulting thiol byproducts were removed in vacuo. Additional H2O (75 mL) was added, and the mixture was extracted with DCM (3 × 20 mL) followed by ethyl acetate (3 × 20 mL). The combined DCM layers were washed with H2O (5 × 10 mL) and dried over magnesium sulfate. The DCM and ethyl S8 acetate layers were combined, and the solvent was removed in vacuo to yield an oily solid. The solid was suspended in MeOH, filtered, and washed with additional MeOH (~40 mL total) to yield 12iPrS-CPP as a yellow solid (27.3 mg, 86%). Single crystals could be obtained by slow evaporation out DMSO or a DCM/MeOH mixture, however these crystals were not of suitable quality for X-ray diffraction. 1H NMR (500 MHz, CDCl3) δ 7.56 (s, 12H), 7.41 (d, J = 8.1 Hz, 12H), 7.36 (d, J = 8.2 Hz, 12H), 3.13 (hept, J = 6.7 Hz, 12H), 1.00 (d, J = 6.7 Hz, 72H). 13C{ 1H} NMR (126 MHz, CDCl3) δ 149.82, 140.80, 140.58, 140.37, 140.20, 132.51, 128.22, 126.34, 40.24,

22.81, 1.11. HRMS (ESI) m/z: found 1801.6088 ([M+H] + calc'd: 1801.6111 for C108H120S12H).

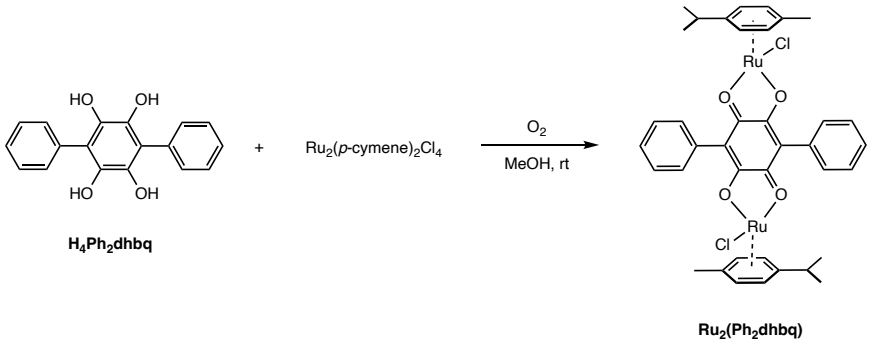

Synthesis of $Ru_2(Ph_2dhbq)$. This compound was prepared using a modified procedure from the literature.[44] In a nitrogen-filled glovebox, a 20 mL scintillation vial was charged with **H_4Ph_2dhbq** (45.0 mg, 0.153 mmol), $Ru_2(p\text{-cymene})_2Cl_4$ (95.7 mg, 0.156 mmol, 1 equiv), and MeOH (13 mL). The vial was capped, stirred at room temperature for 10 min, then removed from the glovebox. The vial was uncapped, and the mixture was stirred in air for two days. The resulting dark precipitate was collected by centrifugation and washed with MeOH (3 × 30 mL), diethyl ether (30 mL), and dried *in vacuo* to yield **$Ru_2(Ph_2dhbq)$** as a black solid (89.8 mg, 0.108 mmol, 71%). Slow diffusion of MeOH into a solution of **$Ru_2(Ph_2dhbq)$** in DCM gave single crystals suitable for X-ray diffraction.

^{1}H NMR and low-resolution ESI-MS data match the previously reported data for this compound. HRMS (ESI) *m/z*: 796.0560 ($[M–Cl]^+$ calc'd: 796.0564 for $C_{38}H_{38}O_4ClRu_2$).

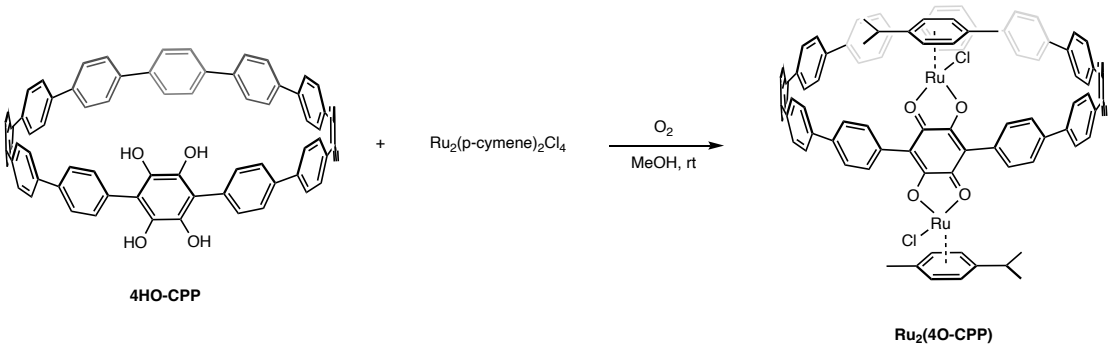

Synthesis of Ru_2(4O-CPP). In a nitrogen-filled glovebox, a 4 mL scintillation vial was charged with 4HO-CPP (2.8 mg, 2.9 μmol) and MeOH (0.5 mL). While stirring, a solution of [Ru(p- S9 cymene)Cl2]2 (4.0 mg, 6.5 μmol, 2.2 equiv) in MeOH (0.5 mL) was added dropwise. The vial was capped, stirred at room temperature for 10 min, and then removed from the glovebox. The vial lid was unscrewed by one-quarter turn to facilitate the slow diffusion of oxygen into the vial, and the mixture was stirred at room temperature for five days. The resulting dark precipitate was collected by filtration and washed with MeOH (2 × 1 mL). The precipitate was recovered using CHCl3 and purified by preparative TLC (DCM eluent; TLC plates were pre-treated with 4% NEt3 in DCM) to yield Ru2(4O-CPP) as a dark red solid (0.8 mg, 19%). Note: due to potential sensitivity of the product to acid, chlorinated solvents were stored over potassium carbonate prior to use. 1H NMR (500 MHz, CDCl3) δ 7.79 (d, J = 8.5 Hz, 4H), 7.66–7.57 (m, 36H), 7.50 (d, J = 8.5 Hz, 4H), 5.58 (d, J = 6.0 Hz, 4H), 5.28 (d, J = 5.9 Hz, 4H), 2.89 (hept, 2H), 2.21 (s, 6H), 1.36 (d, J = 6.9 Hz, 12H). HRMS (ESI) m/z: found 1479.3190 ([M–Cl] + calc'd: 1479.3236 for C92H72O4ClRu2). HRMS (MALDI) m/z: found 1514.2805 ([M]+ calc'd: 1514.2925 for C92H72O4Cl2Ru2).

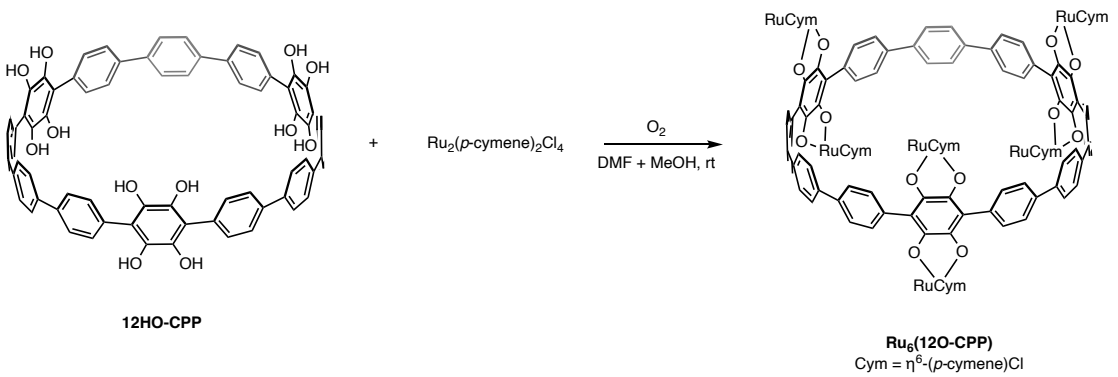

Synthesis of Ru_6(12O-CPP). In a nitrogen-filled glovebox, a 4 mL scintillation vial was charged with 12HO-CPP (2.5 mg, 2.3 μmol) and DMF (0.5 mL). While stirring, a solution of [Ru(pcymene)Cl2]2 (12.1 mg, 19.7 μmol, 8.6 equiv) in MeOH (0.5 mL) was added dropwise. The vial was capped, stirred at room temperature for 10 min, then removed from the glovebox. The vial was uncapped, and the mixture was stirred open to air at room temperature overnight. The mixture was evaporated to dryness under reduced pressure. The resulting dark solid was suspended in MeOH (10 mL), filtered, and washed with additional MeOH (3 × 2 mL). The precipitate was recovered with CHCl3 and concentrated in vacuo to yield Ru6(12O-CPP) as a dark red solid (3.3 mg, 54%). Note: due to potential sensitivity of the product to acid, chlorinated solvents were stored over potassium carbonate prior to use. 1H NMR (500 MHz, CDCl3) δ 7.82–7.47 (m), 5.59 (br), 5.28 (br), 3.94 (br), 2.22 (br), 1.36 (br). HRMS (MALDI) m/z: found 2681.1409 ([M–Cl] + calc'd: 2681.1543 for C132H120O12Cl5Ru6).

2.5 Bridge to Chapter III

Chapter II focuses on the synthesis of novel metalated CPPs via the utilization of a high-yielding late-stage nucleophilic aromatic substitution reaction on fluorinated CPPs. The success of this late-stage transformation is further exploited in chapter III, wherein redox and host-guest active polythianthrene-containing CPPs are synthesized and characterized.

2.6 References

(1) Omachi, H.; Segawa, Y.; Itami, K. Synthesis of Cycloparaphenylenes and Related Carbon Nanorings: A Step toward the Controlled Synthesis of Carbon Nanotubes. *Acc. Chem. Res.* **2012**, *45* (8), 1378–1389. https://doi.org/10.1021/ar300055x.

(2) Darzi, E. R.; Jasti, R. The Dynamic, Size-Dependent Properties of [5]–[12]Cycloparaphenylenes. *Chem. Soc. Rev.* **2015**, *44* (18), 6401–6410. https://doi.org/10.1039/C5CS00143A.

(3) Golder, M. R.; Jasti, R. Syntheses of the Smallest Carbon Nanohoops and the Emergence of Unique Physical Phenomena. *Acc. Chem. Res.* **2015**, *48* (3), 557–566. https://doi.org/10.1021/ar5004253.

(4) Leonhardt, E. J.; Jasti, R. Emerging Applications of Carbon Nanohoops. *Nat. Rev. Chem.* **2019**, *3* (12), 672–686. https://doi.org/10.1038/s41570-019-0140-0.

(5) Segawa, Y.; Levine, D. R.; Itami, K. Topologically Unique Molecular Nanocarbons. *Acc. Chem. Res.* **2019**, *52* (10), 2760–2767. https://doi.org/10.1021/acs.accounts.9b00402.

(6) Jasti, R.; Bhattacharjee, J.; Neaton, J. B.; Bertozzi, C. R. Synthesis, Characterization, and Theory of [9]-, [12]-, and [18]Cycloparaphenylene: Carbon Nanohoop Structures. *J. Am. Chem. Soc.* **2008**, *130* (52), 17646–17647. https://doi.org/10.1021/ja807126u.

(7) Jasti, R.; Bertozzi, C. R. Progress and Challenges for the Bottom-up Synthesis of Carbon Nanotubes with Discrete Chirality. *Chem. Phys. Lett.* **2010**, *494* (1–3), 1–7. https://doi.org/10.1016/j.cplett.2010.04.067.

(8) Omachi, H.; Nakayama, T.; Takahashi, E.; Segawa, Y.; Itami, K. Initiation of Carbon Nanotube Growth by Well-Defined Carbon Nanorings. *Nat. Chem.* **2013**, *5* (7), 572–576. https://doi.org/10.1038/nchem.1655.

(9) Segawa, Y.; Yagi, A.; Matsui, K.; Itami, K. Design and Synthesis of Carbon Nanotube Segments. *Angew. Chem. Int. Ed.* **2016**, *55* (17), 5136–5158. https://doi.org/10.1002/anie.201508384.

(10) Segawa, Y.; Yagi, A.; Itami, K. Chemical Synthesis of Cycloparaphenylenes. *Phys. Sci. Rev.* **2017**, *2* (1). https://doi.org/10.1515/psr-2016-0102.

(11) Wu, D.; Cheng, W.; Ban, X.; Xia, J. Cycloparaphenylenes (CPPs): An Overview of Synthesis, Properties, and Potential Applications. *Asian J. Org. Chem.* **2018**, *7* (11), 2161–2181. https://doi.org/10.1002/ajoc.201800397.

(12) Huang, Q.; Zhuang, G.; Zhang, M.; Wang, J.; Wang, S.; Wu, Y.; Yang, S.; Du, P. A Long π-Conjugated Poly(*Para* -Phenylene)-Based Polymeric Segment of Single-Walled Carbon Nanotubes. *J. Am. Chem. Soc.* **2019**, *141* (48), 18938–18943. https://doi.org/10.1021/jacs.9b10358.

(13) Peters, G. M.; Grover, G.; Maust, R. L.; Colwell, C. E.; Bates, H.; Edgell, W. A.; Jasti, R.; Kertesz, M.; Tovar, J. D. Linear and Radial Conjugation in Extended π-Electron Systems. *J. Am. Chem. Soc.* **2020**, *142* (5), 2293–2300. https://doi.org/10.1021/jacs.9b10785.

(14) Maust, R. L.; Li, P.; Shao, B.; Zeitler, S. M.; Sun, P. B.; Reid, H. W.; Zakharov, L. N.; Golder, M. R.; Jasti, R. Controlled Polymerization of Norbornene Cycloparaphenylenes Expands Carbon Nanomaterials Design Space. *ACS Cent. Sci.* **2021**, *7* (6), 1056–1065. https://doi.org/10.1021/acscentsci.1c00345.

(15) Hmadeh, M.; Lu, Z.; Liu, Z.; Gándara, F.; Furukawa, H.; Wan, S.; Augustyn, V.; Chang, R.; Liao, L.; Zhou, F.; Perre, E.; Ozolins, V.; Suenaga, K.; Duan, X.; Dunn, B.; Yamamto,

Y.; Terasaki, O.; Yaghi, O. M. New Porous Crystals of Extended Metal-Catecholates. *Chem. Mater.* **2012**, *24* (18), 3511–3513. https://doi.org/10.1021/cm301194a.
(16) Sheberla, D.; Sun, L.; Blood-Forsythe, M. A.; Er, S.; Wade, C. R.; Brozek, C. K.; Aspuru-Guzik, A.; Dincă, M. High Electrical Conductivity in Ni_3 (2,3,6,7,10,11-Hexaiminotriphenylene) $_2$, a Semiconducting Metal–Organic Graphene Analogue. *J. Am. Chem. Soc.* **2014**, *136* (25), 8859–8862. https://doi.org/10.1021/ja502765n.
(17) Kubota, N.; Segawa, Y.; Itami, K. H6-Cycloparaphenylene Transition Metal Complexes: Synthesis, Structure, Photophysical Properties, and Application to the Selective Monofunctionalization of Cycloparaphenylenes. *J. Am. Chem. Soc.* **2015**, *137* (3), 1356–1361. https://doi.org/10.1021/ja512271p.
(18) Kayahara, E.; Patel, V. K.; Mercier, A.; Kündig, E. P.; Yamago, S. Regioselective Synthesis and Characterization of Multinuclear Convex-Bound Ruthenium-[n]Cycloparaphenylene (N=5 and 6) Complexes. *Angew. Chem. Int. Ed.* **2016**, *55* (1), 302–306. https://doi.org/10.1002/anie.201508003.
(19) Ypsilantis, K.; Tsolis, T.; Garoufis, A. Interactions of (H5-CpRu)-[12]Cycloparaphenylene Full-Sandwich Complexes with 9-Methylguanine. *Inorg. Chem. Commun.* **2021**, *134*, 108992. https://doi.org/10.1016/j.inoche.2021.108992.
(20) Van Raden, J. M.; Louie, S.; Zakharov, L. N.; Jasti, R. 2,2′-Bipyridyl-Embedded Cycloparaphenylenes as a General Strategy To Investigate Nanohoop-Based Coordination Complexes. *J. Am. Chem. Soc.* **2017**, *139* (8), 2936–2939. https://doi.org/10.1021/jacs.7b00359.
(21) Heras Ojea, M. J.; Van Raden, J. M.; Louie, S.; Collins, R.; Pividori, D.; Cirera, J.; Meyer, K.; Jasti, R.; Layfield, R. A. Spin-Crossover Properties of an Iron(II) Coordination Nanohoop. *Angew. Chem. Int. Ed.* **2021**, *60* (7), 3515–3518. https://doi.org/10.1002/anie.202013374.
(22) Kayahara, E.; Qu, R.; Yamago, S. Bromination of Cycloparaphenylenes: Strain-Induced Site-Selective Bis-Addition and Its Application for Late-Stage Functionalization. *Angew. Chem. Int. Ed.* **2017**, *56* (35), 10428–10432. https://doi.org/10.1002/anie.201704982.
(23) Shudo, H.; Kuwayama, M.; Segawa, Y.; Yagi, A.; Itami, K. Half-Substituted Fluorocycloparaphenylenes with High Symmetry: Synthesis, Properties and Derivatization to Densely Substituted Carbon Nanorings. ChemRxiv February 17, 2023. https://doi.org/10.26434/chemrxiv-2023-zsvnt.
(24) Hashimoto, S.; Kayahara, E.; Mizuhata, Y.; Tokitoh, N.; Takeuchi, K.; Ozawa, F.; Yamago, S. Synthesis and Physical Properties of Polyfluorinated Cycloparaphenylenes. *Org. Lett.* **2018**, *20* (18), 5973–5976. https://doi.org/10.1021/acs.orglett.8b02715.
(25) Leonhardt, E. J.; Van Raden, J. M.; Miller, D.; Zakharov, L. N.; Alemán, B.; Jasti, R. A Bottom-Up Approach to Solution-Processed, Atomically Precise Graphitic Cylinders on Graphite. *Nano Lett.* **2018**, *18* (12), 7991–7997. https://doi.org/10.1021/acs.nanolett.8b03979.
(26) Van Raden, J. M.; Leonhardt, E. J.; Zakharov, L. N.; Pérez-Guardiola, A.; Pérez-Jiménez, A. J.; Marshall, C. R.; Brozek, C. K.; Sancho-García, J. C.; Jasti, R. Precision Nanotube Mimics via Self-Assembly of Programmed Carbon Nanohoops. *J. Org. Chem.* **2020**, *85* (1), 129–141. https://doi.org/10.1021/acs.joc.9b02340.
(27) Shudo, H.; Kuwayama, M.; Shimasaki, M.; Nishihara, T.; Takeda, Y.; Mitoma, N.; Kuwabara, T.; Yagi, A.; Segawa, Y.; Itami, K. Perfluorocycloparaphenylenes. *Nat. Commun.* **2022**, *13* (1), 3713. https://doi.org/10.1038/s41467-022-31530-x.

(28) Cui, S.; Zhuang, G.; Wang, J.; Huang, Q.; Wang, S.; Du, P. Multifunctionalized Octamethoxy-[8]Cycloparaphenylene: Facile Synthesis and Analysis of Novel Photophysical and Photoinduced Electron Transfer Properties. *Org. Chem. Front.* **2019**, *6* (11), 1885–1890. https://doi.org/10.1039/C9QO00372J.
(29) Lu, D.; Zhuang, G.; Jia, H.; Wang, J.; Huang, Q.; Cui, S.; Du, P. A Novel Symmetrically Multifunctionalized Dodecamethoxy-Cycloparaphenylene: Synthesis, Photophysical, and Supramolecular Properties. *Org. Chem. Front.* **2018**, *5* (9), 1446–1451. https://doi.org/10.1039/C8QO00033F.
(30) Narita, N.; Kurita, Y.; Osakada, K.; Ide, T.; Tsuchido, Y.; Kawai, H. A Dodecamethoxy [6]Cycloparaphenylene Consisting Entirely of Hydoroquinone Ether Units: Redox Properties and Host-Guest Complexation. ChemRxiv December 29, 2022. https://doi.org/10.26434/chemrxiv-2022-0c1s7.
(31) Mikhailovskaya, T. F.; Makarov, A. G.; Selikhova, N. Yu.; Makarov, A. Yu.; Pritchina, E. A.; Bagryanskaya, I. Yu.; Vorontsova, E. V.; Ivanov, I. D.; Tikhova, V. D.; Gritsan, N. P.; Slizhov, Y. G.; Zibarev, A. V. Carbocyclic Functionalization of Quinoxalines, Their Chalcogen Congeners 2,1,3-Benzothia/Selenadiazoles, and Related 1,2-Diaminobenzenes Based on Nucleophilic Substitution of Fluorine. *J. Fluor. Chem.* **2016**, *183*, 44–58. https://doi.org/10.1016/j.jfluchem.2016.01.009.
(32) Tashiro, M.; Fujimoto, H.; Tsuge, A.; Mataka, S.; Kobayashi, H. Metacyclophanes and Related Compounds. 23. Preparation of Fluorinated [2,2]Metacyclophanes. *J. Org. Chem.* **1989**, *54* (8), 2012–2015. https://doi.org/10.1021/jo00269a051.
(33) MICHAEL JARMAN; RAYMOND McCAGUE. Octafluorotoluene as a Reagent for the Selective Protection of Alcoholic and Phenolic Functions. Synthesis and Cleavage of Perfluorotolyl and Other Perfluoroaryl Ethers of Steroids and Other Model Compounds. *J Chem Res. S* **1985**, 114–115.
(34) Hellberg, J.; Dahlstedt, E.; Pelcman, M. E. Synthesis of Annulated Dioxins as Electron-Rich Donors for Cation Radical Salts. *Tetrahedron* **2004**, *60* (40), 8899–8912. https://doi.org/10.1016/j.tet.2004.07.017.
(35) Segawa, Y.; Miyamoto, S.; Omachi, H.; Matsuura, S.; Šenel, P.; Sasamori, T.; Tokitoh, N.; Itami, K. Concise Synthesis and Crystal Structure of [12]Cycloparaphenylene. *Angew. Chem. Int. Ed.* **2011**, *50* (14), 3244–3248. https://doi.org/10.1002/anie.201007232.
(36) Pierpont, C. G.; Buchanan, R. M. Transition Metal Complexes of O-Benzoquinone, o-Semiquinone, and Catecholate Ligands. *Coord. Chem. Rev.* **1981**, *38* (1), 45–87. https://doi.org/10.1016/S0010-8545(00)80499-3.
(37) Kitagawa, S.; Kawata, S. Coordination Compounds of 1,4-Dihydroxybenzoquinone and Its Homologues. Structures and Properties. *Coord. Chem. Rev.* **2002**, *224* (1), 11–34. https://doi.org/10.1016/S0010-8545(01)00369-1.
(38) Lyaskovskyy, V.; de Bruin, B. Redox Non-Innocent Ligands: Versatile New Tools to Control Catalytic Reactions. *ACS Catal.* **2012**, *2* (2), 270–279. https://doi.org/10.1021/cs200660v.
(39) Mercuri, M. L.; Congiu, F.; Concas, G.; Sahadevan, S. A. Recent Advances on Anilato-Based Molecular Materials with Magnetic and/or Conducting Properties. *Magnetochemistry* **2017**, *3* (2), 17. https://doi.org/10.3390/magnetochemistry3020017.
(40) Kamin, A. A.; Moseley, I. P.; Oh, J.; Brannan, E. J.; Gannon, P. M.; Kaminsky, W.; Zadrozny, J. M.; Xiao, D. J. Geometry-Dependent Valence Tautomerism, Magnetism, and

Electrical Conductivity in 1D Iron–Tetraoxolene Chains. *Chem. Sci.* **2023**. https://doi.org/10.1039/D2SC06392A.
(41) Therrien, B.; Süss-Fink, G.; Govindaswamy, P.; Renfrew, A. K.; Dyson, P. J. The "Complex-in-a-Complex" Cations [(Acac)2M⊂Ru6(p-iPrC6H4Me)6(Tpt)2(Dhbq)3]6+: A Trojan Horse for Cancer Cells. *Angew. Chem. Int. Ed.* **2008**, *47* (20), 3773–3776. https://doi.org/10.1002/anie.200800186.
(42) Mattsson, J.; Govindaswamy, P.; Renfrew, A. K.; Dyson, P. J.; Štěpnička, P.; Süss-Fink, G.; Therrien, B. Synthesis, Molecular Structure, and Anticancer Activity of Cationic Arene Ruthenium Metallarectangles. *Organometallics* **2009**, *28* (15), 4350–4357. https://doi.org/10.1021/om900359j.
(43) Therrien, B. Transporting and Shielding Photosensitisers by Using Water-Soluble Organometallic Cages: A New Strategy in Drug Delivery and Photodynamic Therapy. *Chem. - Eur. J.* **2013**, *19* (26), 8378–8386. https://doi.org/10.1002/chem.201301348.
(44) Garci, A.; Mbakidi, J.-P.; Chaleix, V.; Sol, V.; Orhan, E.; Therrien, B. Tunable Arene Ruthenium Metallaprisms to Transport, Shield, and Release Porphin in Cancer Cells. *Organometallics* **2015**, *34* (16), 4138–4146. https://doi.org/10.1021/acs.organomet.5b00555.
(45) Garci, A.; Gupta, G.; Dalvit, C.; Therrien, B. Investigating the Formation Mechanism of Arene Ruthenium Metallacycles by NMR Spectroscopy. *Eur. J. Inorg. Chem.* **2014**, *2014* (33), 5651–5661. https://doi.org/10.1002/ejic.201402639.
(46) Van Raden, J. M.; Leonhardt, E. J.; Zakharov, L. N.; Pérez-Guardiola, A.; Pérez-Jiménez, A. J.; Marshall, C. R.; Brozek, C. K.; Sancho-García, J. C.; Jasti, R. Precision Nanotube Mimics via Self-Assembly of Programmed Carbon Nanohoops. *J. Org. Chem.* **2020**, *85* (1), 129–141. https://doi.org/10.1021/acs.joc.9b02340.
(47) Kamin, A. A.; Moseley, I. P.; Oh, J.; Brannan, E. J.; Gannon, P. M.; Kaminsky, W.; Zadrozny, J. M.; Xiao, D. J. Geometry-Dependent Valence Tautomerism, Magnetism, and Electrical Conductivity in 1D Iron–Tetraoxolene Chains. *Chem. Sci.* **2023**. https://doi.org/10.1039/D2SC06392A.

CHAPTER III

LATE-STAGE SYNTHESIS AND CHARACTERIZATION OF REDOX-ACTIVE THIANTHRENE-CONTAINING CYCLOPARAPHENYLENES

Chapter III is adapted from a manuscript in preparation for submission to Angewandte Chemie entitled "Late-Stage Synthesis and Characterization of Redox-Active Thianthrene-Containing Cycloparaphenylenes." The manuscript was written by me (soon with contributions from Audrey Davenport and Rachel Galfo) with edits by Veronica Spaulding and Professor Ramesh Jasti. All molecules were synthesized and characterized by me, and all computations were performed by Veronica Spaulding. Cyclic voltammogram data collection and analysis was performed by Audrey Davenport and Rachel Galfo. Crystallographic data collection and analysis was performed by Dr. Lev Zakharov. Professor Ramesh Jasti provided guidance on the project.

3.1 Introduction

Thianthrene is a widely researched heterocyclic p-type organic semiconductor. It has rich electrochemistry that functions as a switch for its characteristic nonplanar to planar isomerization. The incorporation of the thianthrene moiety in macrocyclic systems is much less explored, however such systems may benefit from increased solubility and improved host-guest complexation. Cycloparaphenylenes (CPPs) are a relatively new class of nonplanar aromatic macrocycles with tunable electrochemical, photophysical, and host-guest properties. In this work we report high yielding, late-stage transformations of fluorinated cycloparaphenylenes (CPPs) into multi-thianthrene containing strained macrocyclic nanocarbons. Single crystal X-ray diffraction of our dodeca-substituted CPP displays tub-shaped 5,7,12,14-tetrathiapentacene units (TTP) that

curve around neighboring CPPs forming hexagonal crystals. Electrochemical analysis shows multiple reversible oxidation events, with the thianthrene CPPs being easier to oxidize compared to linear counterparts. Host-guest complexation with C60 shows improved binding constants compared to the all-hydrocarbon [12]CPP counterpart. This extremely efficient introduction of functional heterocyclic fragments into CPPs contributes to the study and development of strained, pi-rich, and electrochemically active nanomaterials.

[n]CPPs (n = the number of phenyl units) are a class of curved aromatic macrocycles that display size dependent optoelectronic properties that are unlike other small molecules or carbon nanomaterials.[1,2] First synthesized in 2008 by Jasti,[3] CPPs and their derivatives have garnered interest as bright and versatile chromophores,[4,5] participants in supramolecular and host-guest chemistry,[6] novel monomers,[7,8] organic ligands,[9–12] and components in organic electronics.[5,13,14] It is expected that future applications of CPP nanomaterials will continue to grow with advancements in derivatization, synthesis, and characterization.[15] New methods for late-stage CPP derivatization include nucleophilic aromatic substitution (SNAr), first shown on CPPs in 2023 by Terabayashi et al. who reported late-stage functionalization of an alkene-inserted CPP with a pyrrole nucleophile.[16] This was followed by work done by Shudo et al. also using pyrrole on highly fluorinated CPPs.[17] In 2023 Kamin et al., in collaboration with our lab, demonstrated that sulfur and oxygen nucleophiles also work efficiently to derivatize fluorinated CPPs.[11]

Thianthrene and thianthrene-containing systems are multi-talented scaffolds with d[18–21]18–21iverse applications in materials science and related fields.

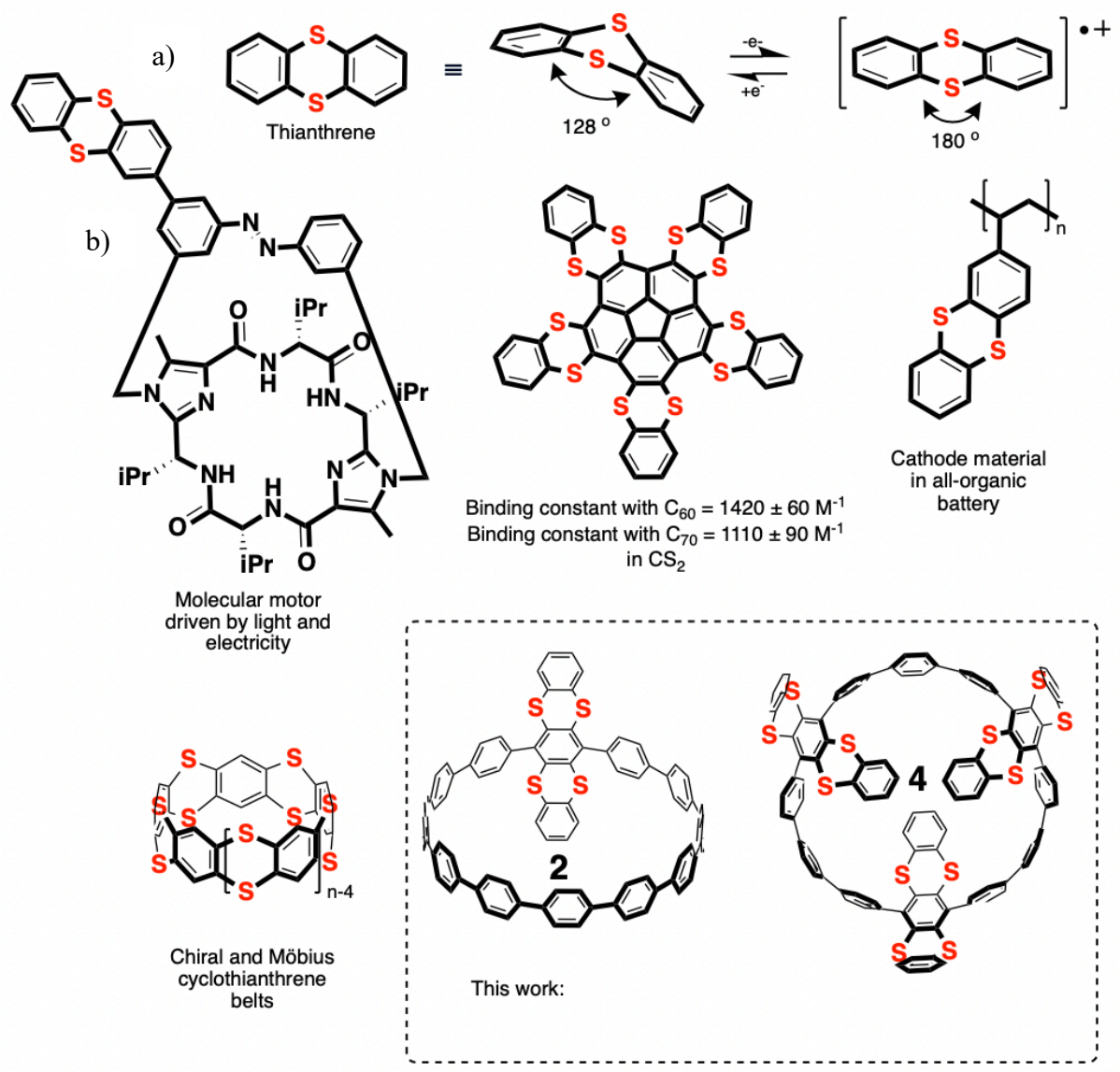

Figure: 3.1. a) Oxidation-induced planarization of thianthrene. b) Representative examples of diversly functioned thianthrene-containing systems.

Thianthrenes continue to be explored in the development of functional polymers,[18–20] room-temperature phosphorescent materials,[21–24] participants in supramolecular chemistry,[25–28] and redox-active materials. Thianthrene has one of the highest redox potentials amongst organic cathode materials (4.1 V vs. Li+/Li, 0.84 V vs. Fc/Fc+ for the first oxidation) making it a promising candidate for high-potential organic electrodes.[19,29] Unlike the planar oxygen-containing analogue

1,4-dibenzodioxin, neutral thianthrene has a bent geometry of 128 degrees which planarizes to 180 degrees upon its first and second oxidation to the cation and dictation respectively (Figure 3.1 a).[30] This planarization and increase in aromaticity upon oxidation helps provide stability while also affording a redox-activated isomerization that can be harnessed for applications requiring conformational flexibility.

Some representative examples that highlight the variety of uses for the thianthrene motif are shown (Figure 3.1 b). First, the thianthrene functions as a component in the first molecular motor activated by electrochemistry and light.[31] Researchers found that when connected to a chiral imidazole-containing macrocyclic clamp the redox-activated isomerization of thianthrene and the light-activated isomerization of azobenzene were able to propel the system with a pushing motion Another report utilizes the naturally bent shape of thianthrene synergistically with curved polyaromatics, such as corannulene, to form concave molecules with electron-rich arms that are capable of increasing the binding constant between the corannulene derivative and C60 (1.4x103 M-1), affording the highest corannulene-based fullerene binding at the time.[28] Researchers have exploited the promising electrochemical properties of thianthrene allowing for the construction of an all-organic battery with poly(2-vinylthianthrene) functioning as the cathode material and poly(2-methacrylamide-TCAQ) as the anode. This all-organic battery showed excellent performance with ~65% discharge capacity retention after 250 cycles and highly stable charge/discharge curve profiles.[32] Finally, the curved morphology of thianthrene was harnessed to make a series of sulfur embedded hydrocarbon belts.[33] The cyclothianthrenes [6]CT, [7]CT, and [8]CT showed quasi-reversible first oxidations at 1.14 V, 0.82 V and 0.90 V versus Fc/Fc+ respectively. While the cyclothianthrenes reported in this study showed diminished abilities to form stable radical cations upon oxidation in comparison to linear thianthrenes, the macrocyclic

nature of the cyclothianthrenes affords a potential system for novel host-guest complexes and porous systems. We hypothesized that decorating the backbone of the CPP with pendant thianthrenes could better preserve the redox character of linear thianthrenes while also maintaining the benefits of curved macrocyclic systems.

3.2 Results and Discussion

3.2.1 Synthesis

In this work we report the high yielding late-stage synthesis and characterization of multi-thianthrene-containing CPP systems (2 and 4) via SNAr of fluorinated CPPs (1 and 3) with 1,2-benzenedithiol (Scheme 3.1). This synthetic approach was inspired by work done in the Swager lab which showed that ortho-aryldithiols and ortho-aryldifluorides efficiently undergo SNAr affording a series of molecules and polymer networks with multiple thianthrene moieties.[34] Perfluorinated CPPs (1[11] and 3[35]) previously reported by our lab were used as electrophilic precursors affording the multi-thianthrene CPPs in extremely high yield. Structures 2 and 4 were confirmed by 1H NMR, 13C NMR, high-resolution mass spectrometry, UV-Vis/ fluorescence measurements, and 4 was confirmed by X-ray crystallography. We found that the multi-thianthrene-containing macrocycles synthesized herein retain the absorbance and fluorescence maximum values typical of CPPs of this size, display increased binding with C60 compared to their all-hydrocarbon [12]CPP counterpart, and show promising redox profiles with multiple reversible oxidation events.

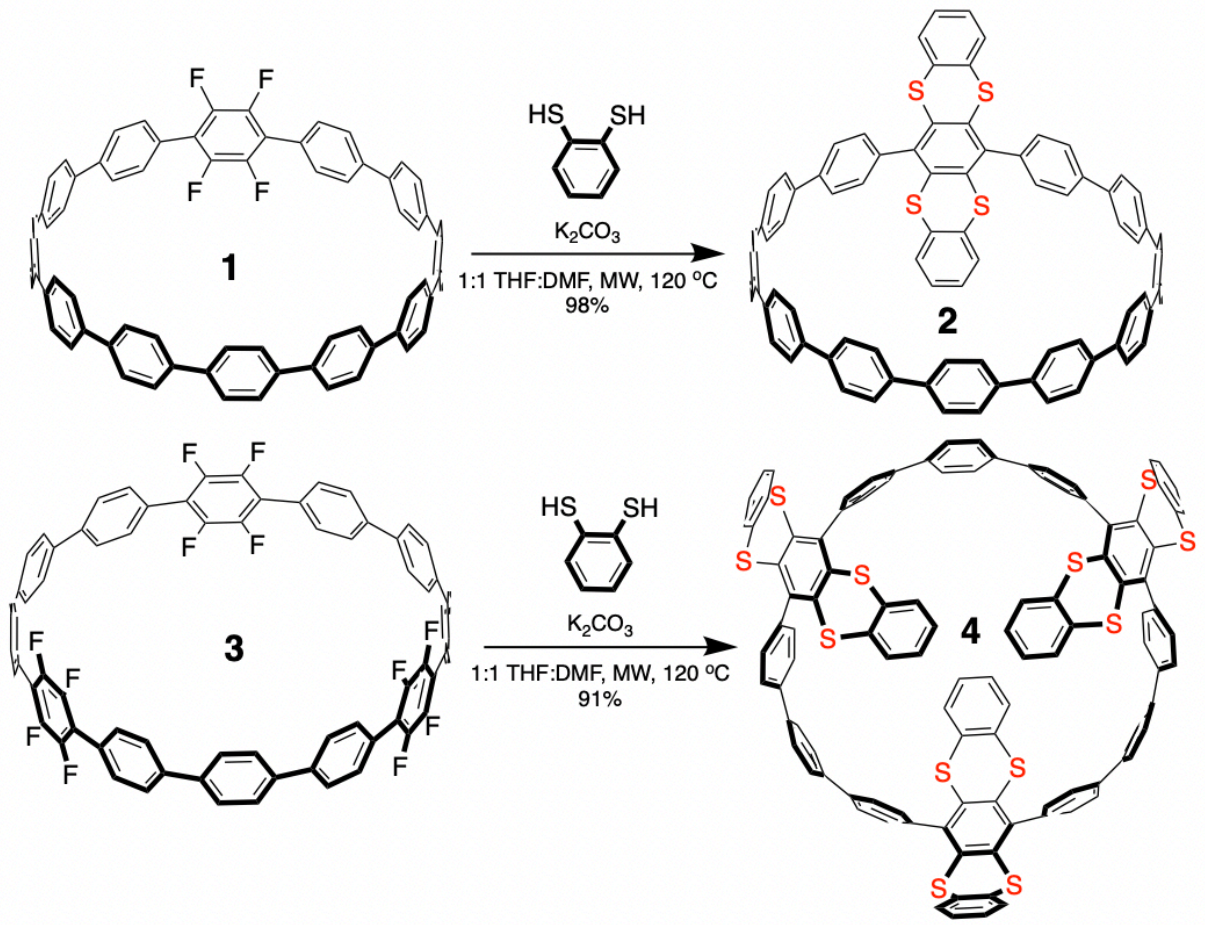

Scheme 3.1. Synthesis of multi-thianthrene-containing CPPs (2 and 4) from fluorinated CPP precursors (1 and 3) via nucleophilic aromatic substitution with 1,2-benzenedithiol.

CPP synthesis is very amenable to the inclusion of fluorine substituents, and because of this there is a large family of CPPs with varying amounts and placements of fluorine, some of which can be synthesized on gram scale.[36] This paired with the efficiency of SNAr for late-stage CPP derivatization makes this a very promising approach for realizing molecular applications. The nonplanarity of these systems and limited pi-pi stacking renders them soluble in common organic solvents, a feature that may be useful for certain applications such as flow batteries. Additional functionalization such as inclusion of donor and/or acceptor groups or functional handles that allow for extension of the CPP into pi-rich and polymeric systems are exciting directions for these

molecules. The dynamic self-correcting nature of the SNAr reaction as shown by the Swager lab[34] paired with the high reaction efficiency may allow for the synthesis of extended polymers and covalent organic frameworks from the reaction of fluorinated CPPs and 1,2-5,6-tetrathiolbenzene. Oxidation of 2 and 4 to electron-poor sulfoxide or sulfone-containing CPPs is another interesting late-stage modification that may afford yet another handle to modify the photophysics and host-guest abilities of CPPs.

3.2.2 X-ray Crystallographic Analysis

We were able to confirm the identity and connectivity of 4 via X-ray crystallographic analysis (Fig. 3.2). Crystals of 4 were grown via solvent layering of chloroform and pentane in an NMR tube. Due to a high amount of disordered solvent molecules, precise structural information could not be determined. It was possible to solve only two CHCl3 solvent molecules and other solvent molecules were treated by SQUEEZE. One of the S2C6H groups (C91-C96) is highly disordered. Atomic thermal parameters in this group are elongated and this group was refined as a C6-group with the ideal geometry. The X-ray data was however sufficient enough to confirm the structure, connectivity, and crystal packing. The hexagonal space group was determined as the crystal packing pattern. More information regarding the X-ray crystallographic analysis can be found in the supporting information. Interestingly, the TTP units display the less commonly favored tub conformation, as they curve around neighboring CPP backbones forming a hexagonal crystal. This suggests that interactions between the thianthrene units and neighboring CPPs afford a handle to influence crystal packing. While compound 2 is also crystalline, we were unable to get high enough quality crystals for single crystal X-ray analysis.

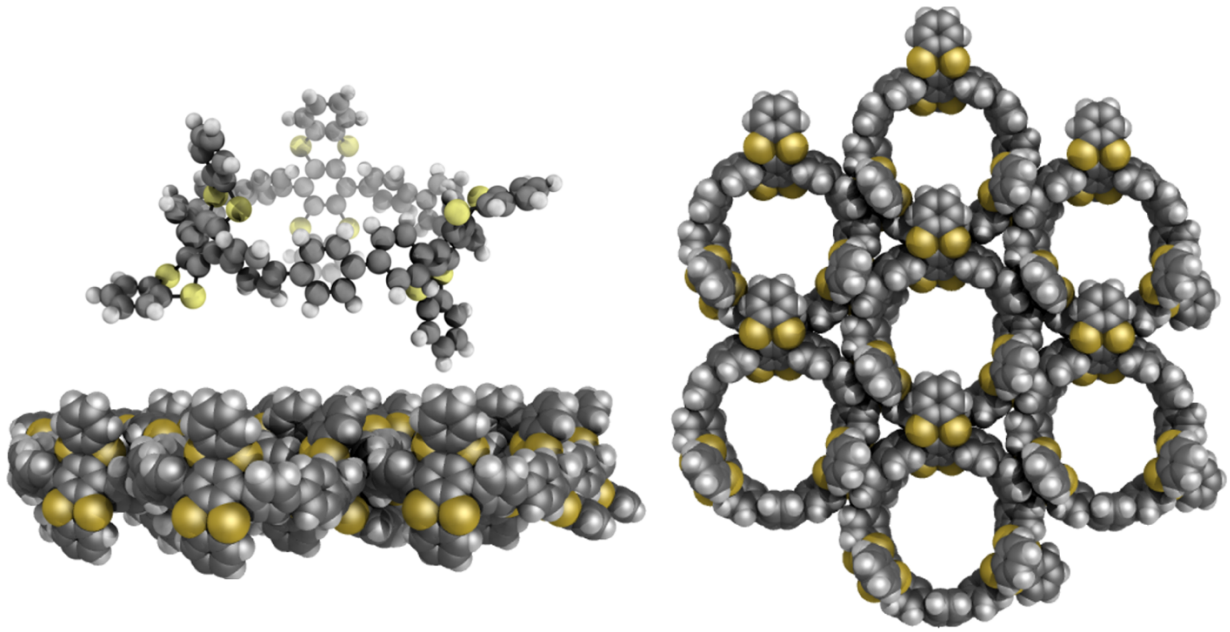

Figure 3.2. X-ray crystallographic data for 4.

3.2.3 Photophysical Properties

We next characterized the photophysical properties of 2 and 4 to probe the effects of the thianthrene units on the all-hydrocarbon [12]CPP scaffold (Fig. 3.3). Like the fluorinated parent molecules, the incorporation of thianthrene units into the backbone of [12]CPP has very little impact on the absorbance and emission maxima. Compound 2 was determined to have a maximum absorption at 330 nm in dichloromethane compared to 339 nm for the all-hydrocarbon [12]CPP. This slight hypsochromic shift is common amongst symmetry broken CPPs.[37–39] The extinction coefficient for 2 (1.2 x105 M-1 cm-1) is slightly lower than that of [12]CPP (1.4 x105 M-1 cm-1). Compound 2 has an emission profile nearly identical to [12]CPP with a fluorescence maximum at 448 nm compared to 450 nm for [12]CPP. Compound 4 is also similar photophysically to 2 and [12]CPP. Compound 4 has a maximum absorption of 316 nm and an extinction coefficient of 1.2 x105 M-1 cm-1. The maximum emission of 4 was found to be 428 nm in DCM. This hypsochromic

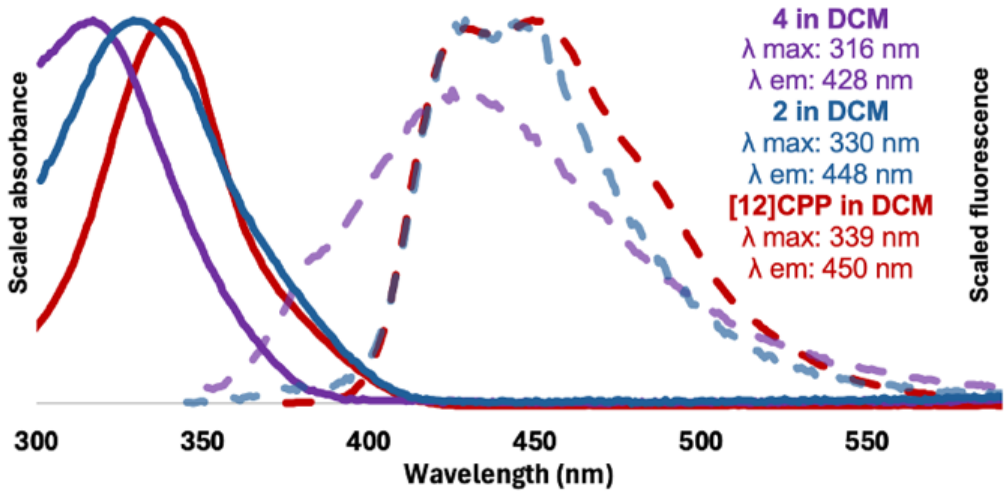

Figure 3.3. Scaled absorbance (solid lines) and emission (dashed lines) of 2, 4, and all-hydrocarbon [12]CPP in DCM.

shift may arise from the distortion of the CPP backbone leading to less effective conjugation. We observed a slight bathochromic shift to 448 nm in the fluorescence of 4 in DMF, however measurements in toluene afforded the same maximum emission as when in DCM. DFT analysis of the molecular orbitals suggests 4 has donor-acceptor behavior wherein upon excitation there is a transfer from the more electron-rich thianthrene unit to the more electron-poor CPP backbone.(SI) This would explain the slight solvatochromism and the reduced brightness of 4 in comparison to 2.(SI) The broadness of the fluorescence profile of 4 can be explained by an increased number of contributions from symmetry allowed transitions (SI).

3.2.4 Binding Studies with Fullerene

We also explored the effect of the thianthrene units on the host-guest properties of 2 and 4 with C60 (Fig.3.4). Fluorescence titration experiments showed complete quenching of the fluorescence of 2 and 4 in toluene upon the addition of sufficient concentrations of C60. The 1:1 binding constants calculated using BindFit were determined to be 7.3x104 M-1 and 1.0x105 M-1

for 2 and 4 respectively. This increase in binding compared to the all hydrocarbon [12]CPP suggests that the inclusion of thianthrene moieties can act as a handle to further tune host-guest interactions in CPPs.

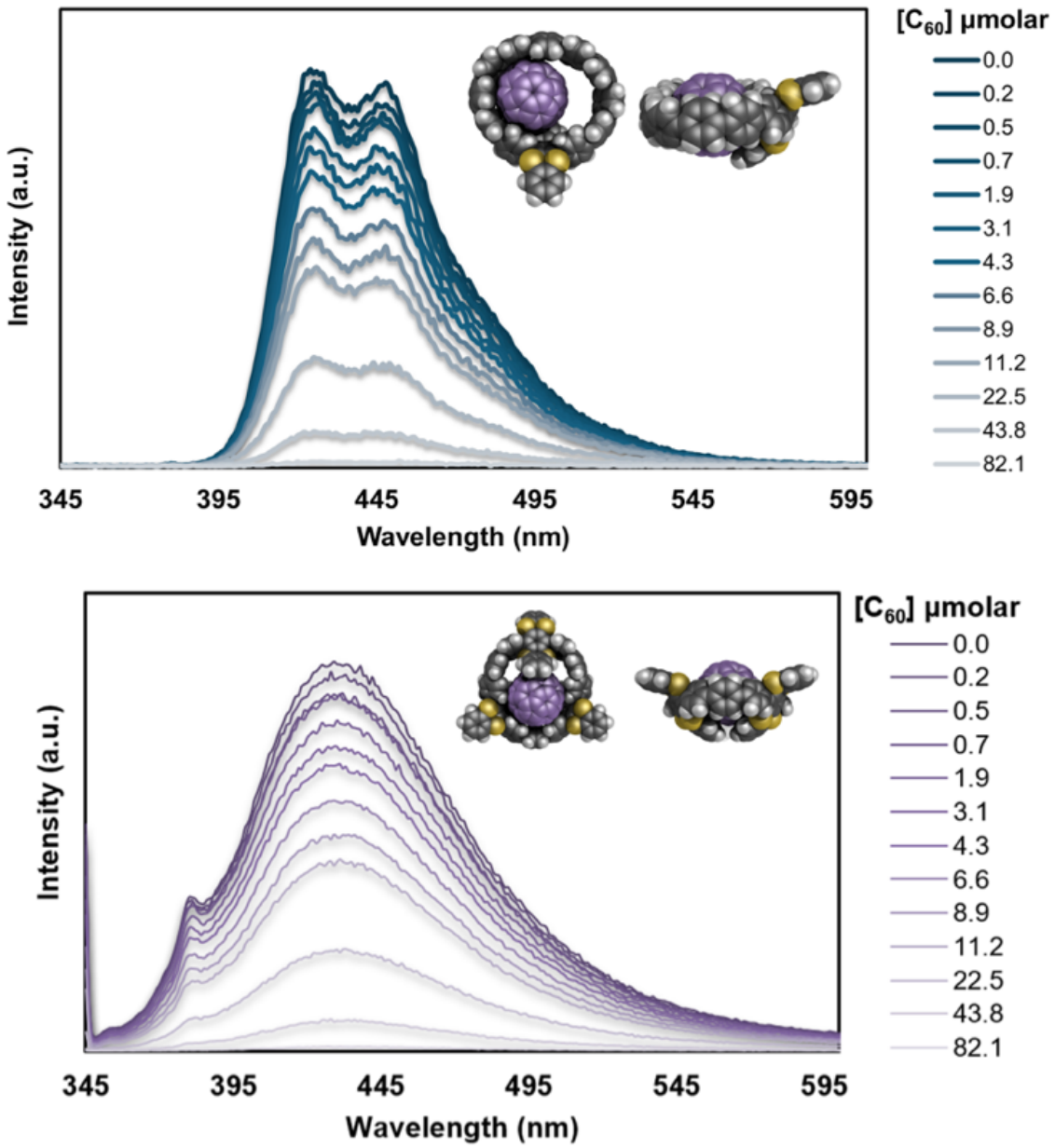

Figure 3.4. DFT space-filling models of CPPs 2 (top) and 4 (bottom) hosting C_{60} next to their fluorescence spectra, which both show quenching by C_{60}.

While these binding constants are lower than that of [10]CPP and C60, they are still quite high amongst other common hosts.

3.2.5 Redox Properties

We next investigated the redox properties of 2 and 4 and found that both molecules display two reversible oxidations. CV scans for 4 are shown below in Figure 3.5. The fact that both molecules show only two reversible oxidations could arise from the nature of delocalization in CPP radical cations. The delocalization may also account for the lower voltage needed to oxidize the thianthrene in the CPP versus linear counterparts. More work is being conducted to investigate the redox behavior of these molecules in solution and solid-state.

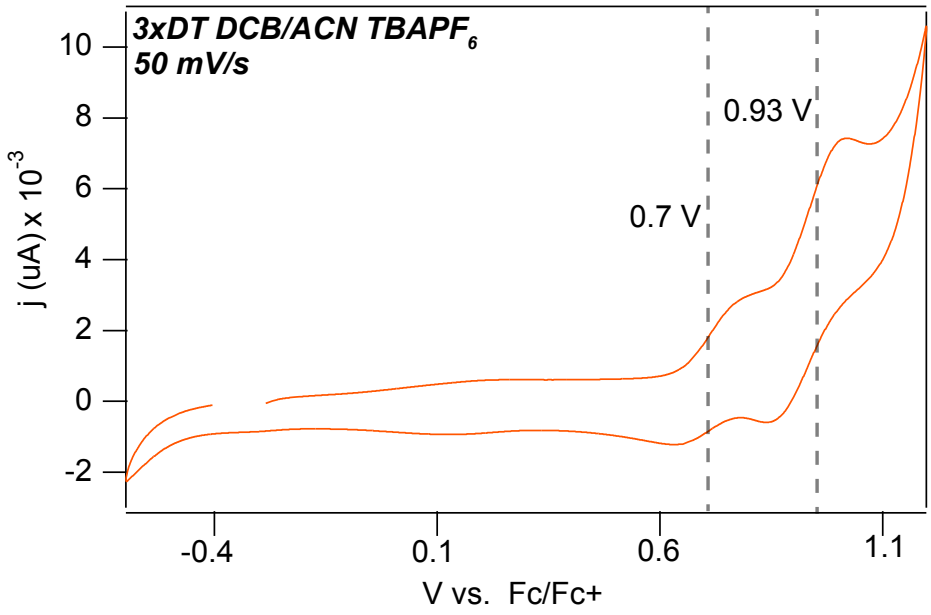

Figure 3.5. Cyclic voltammetry scan of 4 showing two reversible oxidations.

3.3 Conclusion

In summary, we have shown that SNAr of fluorinated CPPs and 1,2-benzenedithiol is a highly efficient late-stage modification that affords multi-thianthrene appended macrocycles with

increased binding to C60, altered solid-state crystal packing, and multiple reversible oxidations. Thianthrene-based molecules are promising for the development of high-potential organic electrodes towards rechargeable batteries with high energy and power density. The thianthrene motif has also been used as a molecular tool for imparting switchable motion, non-planar geometry, electron donation, and sites for late-stage functionalization. The highly tunable nature of CPPs and their strained macrocyclic nature makes these thianthrene-containing systems and future derivatives interesting from a synthetic and materials perspective. We anticipate that derivatives of these nanocarbons will be useful in materials and related fields.

3.4 Experimental Section

3.4.1 General Experimental Details

Unless otherwise noted, commercially available materials were used without purification. Compounds 1 and 3 were prepared according to the literature.[40–42] Moisture and oxygen sensitive reactions were carried out in flame-dried glassware and under an inert atmosphere of purified nitrogen using syringe/septa technique. Tetrahydrofuran (THF) and dimethylformamide (DMF) were dried by filtration through alumina according to the methods described by Grubbs.[43] Alumina column chromatography was conducted with SorbTech basic alumina (pH 10), Act. II-III, 50-200 μm. ^{1}H and ^{13}C NMR spectra were recorded on a Bruker Avance III HD 500 (^{1}H: 500 MHz, ^{13}C: 126 MHz) NMR spectrometer. The chemical shifts (δ) were reported in parts per million (ppm) and were referenced to the residual protio-solvent (CD_2Cl_2, ^{1}H: δ = 5.32 ppm and ^{13}C: δ = 53.84 ppm; deuterated 1,1,2,2-tetrachloroethane (TCE-d_2), ^{1}H: δ = 6.00 ppm and 13C: δ = 73.78 ppm) or to tetramethylsilane (for $CDCl_3$, TMS, δ = 0.00 ppm). Coupling constants (J) are given in Hz and the apparent resonance multiplicity is reported as s (singlet), d (doublet), t (triplet), q (quartet), dd (doublet of doublets) or m (multiplet). UV/Vis absorption and fluorescence spectra were

recorded on an Agilant Cary 100 spectrophotometer and a Horiba Jobin Yvon Fluoromax-4 Fluorimeter, respectively. All measurements were carried out under ambient conditions in a Spectrocell RF-1010-T threaded top vacuum formed borosilicate fluorometer cell (10 mm light path).

3.4.2 Synthetic Details

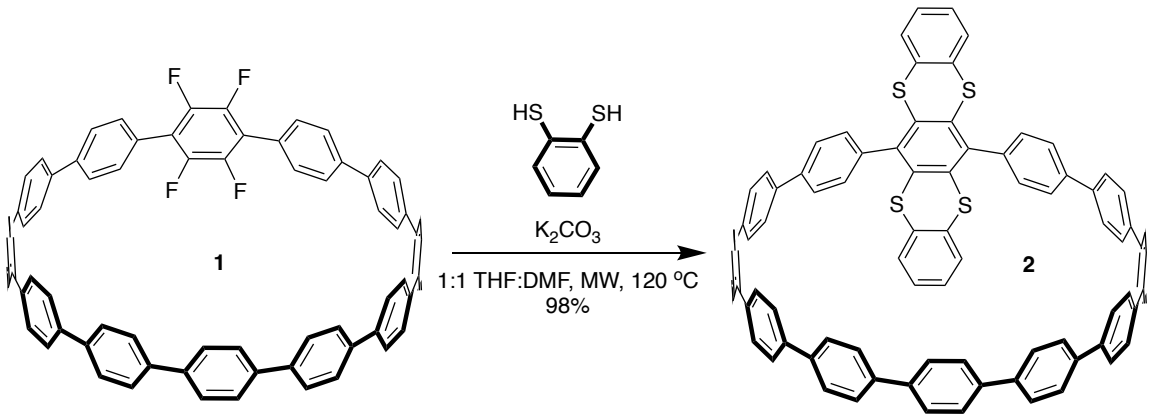

Compound 2: 1 (g, mmol, eq), 1,2-Benzenedithiol (g, mmol, eq), and K_2CO_3 (g, mmol, eq) were added to a microwave flask and dissolved in THF (mL, M) and DMF (mL, M). The reaction mixture was heated with microwave to 120 °C and allowed stir for 24 hrs. It was then cooled to room temperature and diluted with DCM and water. A 1M aqueous solution of K_2CO_3 was added until the solution was basic, and the product was extracted with DCM (4 X 50 mL), washed with water (2 X 50 mL), washed with brine (2 X 50 mL), dried over sodium sulfate, filtered, and concentrated. Finally, the material was rinsed with methanol and dried to afford the product as an off-white powder (mg) in 98% yield. ^{1}H NMR (500 MHz, Methylene Chloride-d_2) δ 7.77 – 7.63 (m, 40H), 7.26 (d, J = 8.2 Hz, 4H), 7.06 (dd, J = 5.8, 3.4 Hz, 4H), 6.95 (dd, J = 5.8, 3.4 Hz, 4H). ^{13}C NMR (126 MHz, CD_2Cl_2) δ 141.05, 140.05, 139.23, 138.59, 138.56, 138.54, 138.52, 138.49, 138.45, 138.38, 137.49, 135.79, 135.54, 130.99, 128.36, 127.98, 127.60, 127.42, 127.36, 127.34,

127.29, 127.27, 127.12. HRMS (MALDI) m/z: [M]+ calculated for $C_{84}H_{52}S_4$ 1188.30, found 1188.30.

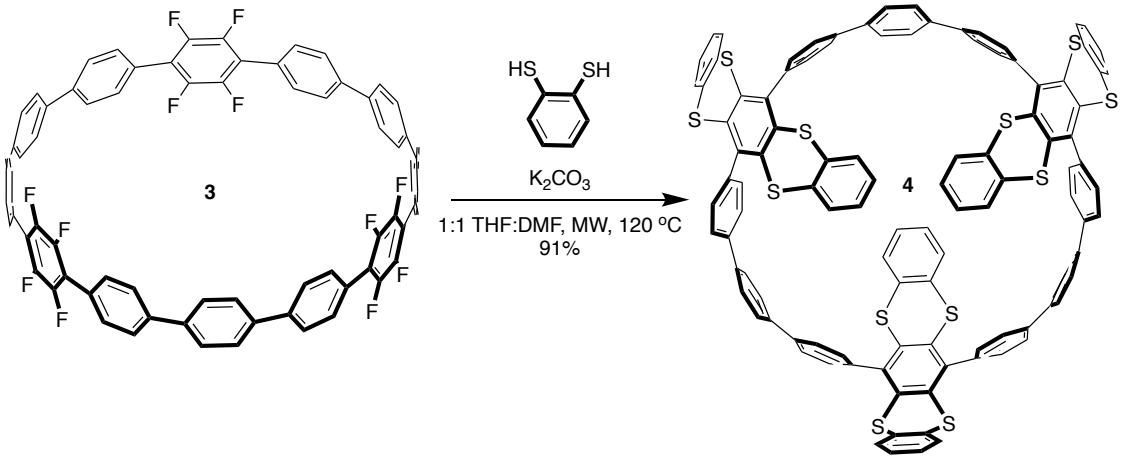

Compound 4: 3 (g, mmol, eq), 1,2-Benzenedithiol (g, mmol, eq), and K_2CO_3 (g, mmol, eq) were added to a microwave flask and dissolved in THF (mL, M) and DMF (mL, M). The reaction mixture was heated with microwave to 120 °C and allowed stir for 24 hrs. It was then cooled to room temperature and diluted with DCM and water. A 1M aqueous solution of K_2CO_3 was added until the solution was basic, and the product was extracted with DCM (4 X 50 mL), washed with water (2 X 50 mL), washed with brine (2 X 50 mL), dried over sodium sulfate, filtered, and adsorbed onto basic alumina. An alumina plug eluted with DCM in hexanes (0-100%) afforded the product as an off-white powder (mg) in 91% yield. ^{1}H NMR (500 MHz, Methylene Chloride-d_2) δ 7.78 – 7.57 (m, 24H), 7.53 (s, 4H), 7.41 (dd, J = 21.4, 7.3 Hz, 6H), 7.29 (dd, J = 25.7, 8.2 Hz, 12H), 7.16 (dd, J = 5.7, 3.4 Hz, 2H), 7.13 – 7.06 (m, 6H), 6.97 (dd, J = 13.2, 5.7 Hz, 6H). ^{13}C NMR (126 MHz, CD_2Cl_2) δ 141.01, 140.11, 139.66, 136.40, 135.93, 135.83, 135.75, 135.64, 131.74, 131.48, 129.13, 128.67, 128.49, 128.30, 127.79, 127.22, 127.06, 126.88. HRMS (MALDI) m/z: [M]+ calculated for $C_{108}H_{60}S_{12}$ 1740.13, found 1740.14.

3.4.3. X-ray Crystallographic Analysis

X-ray Crystallography. Diffraction intensities for 4 were collected at 173 K on a Bruker Apex2 single crystal diffractometer using CuKα radiation, 1.54178 Å. Space group was determined based on systematic absences. Absorption correction was applied by SADABS[*]. Structure was solved by direct methods and Fourier techniques and refined on F^2 using full matrix least-squares procedures. All non-H atoms were refined with anisotropic thermal parameters. H atoms in the structure were refined in calculated positions in a rigid group model. The diffraction data at high angles are very weak due to a strong disorder of solvent molecules. They were collected only up to resolution 1.01 Å even by using a strong *Incoatec* Cu-source. However, it provides the appropriate ratio of the number of the measured reflections per the number of the refined parameters, 12202/1142. Two $CHCl_3$ solvent molecules located outside the hoop were found from the XRD data and refined. Others solvent molecules located inside the hoop are highly disordered and were treated by SQUEEZE[**]. Solvent molecules treated by SQUEEZE were not included in the total formula of the compound given in the CIF file. The structure was determined in a non-centrosymmetrical space group as a racemic twin: the Flack is 0.12(3). One of the $S_2C_6H_4$ groups is highly disordered. Atomic thermal parameters in this group are elongated and this group was refined as a C6-group with the ideal geometry. The RIGU option was used in the structure refinement. The structure is determined with a low resolution. However, the X-ray structure provides the clear chemical results. All calculations were performed by the Bruker SHELXL-2014/7 package [***].

*Crystallographic Data for **4**:* $C_{110}H_{62}Cl_6S_{12}$, M = 1981.01, 0.15 x 0.14 x 0.08 mm, T = 173(2) K, Hexagonal, space group $P6_5$, a = 19.6392(4) Å, b = 19.6392(4) Å, c = 53.6698(19) Å, α = 90°, β = 90°, γ = 120.0°, V = 17927.0(10) Å^3, Z = 6, Dc = 1.101 Mg/m^3, μ(Cu) = 3.582 mm^{-1}, F(000) = 6096, $2\theta_{max}$ = 100.134°, 87596 reflections, 12202 independent reflections [R_{int} = 0.1647], R1 =

0.0717, wR2 = 0.1832 and GOF = 1.028 for 12202 reflections (1142 parameters) with I>2σ(I), R1 = 0.1057, wR2 = 0.2059 and GOF = 1.001 for all reflections, the Flack = 0.12(3), max/min residual electron density +0.268/-0.293 eÅ^{-3}.

3.4.4. Photophysical Characterization

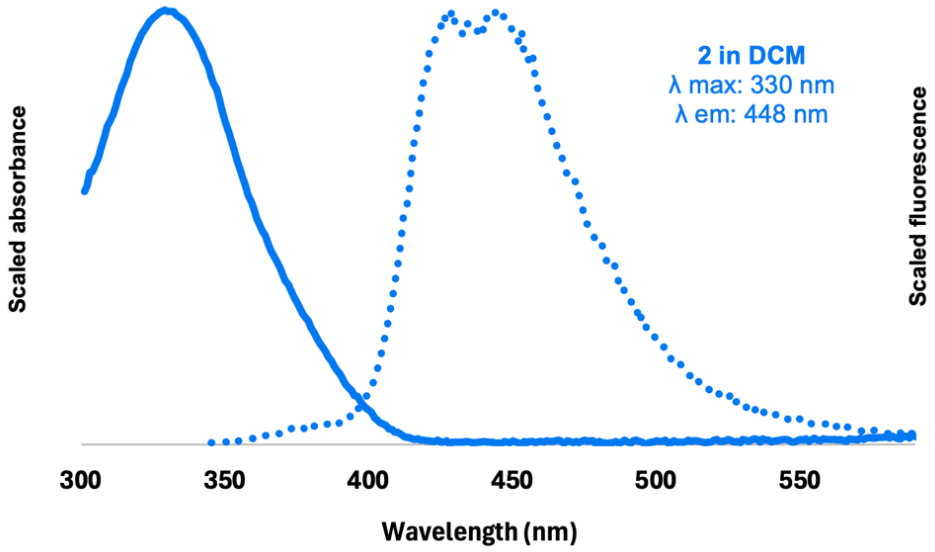

Figure 3.6. UV-Vis and fluorescence profiles of 2 in DCM.

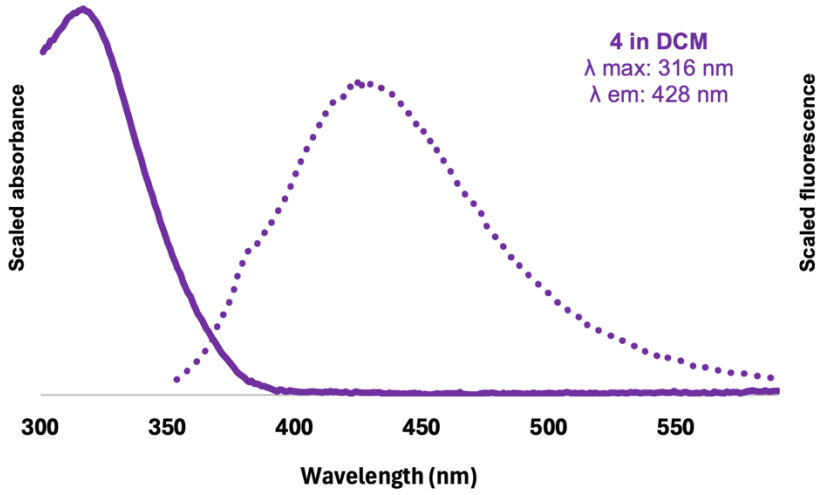

Figure 3.7. UV-Vis and fluorescence profiles of 4 in DCM.

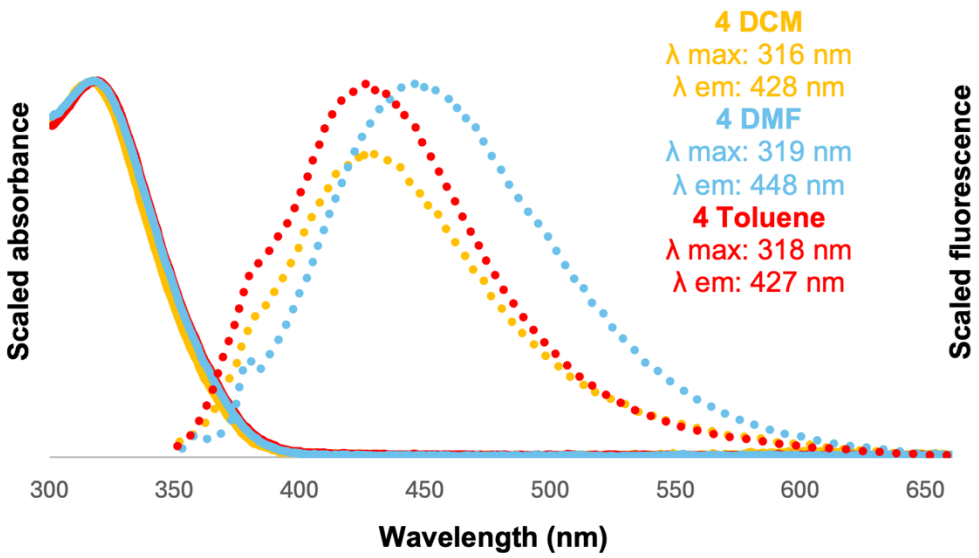

Figure 3.8. Scaled absorbance and fluorescence of 4 in various solvents excited at 340 nm.

For extinction coefficient measurements, 2 and 4 were dissolved at known concentrations in DCM. Solutions of 2 and 4 were then added incrementally to a cuvette containing a known amount of DCM and absorbance measurements were taken after each addition. The whole process was repeated three times for 2 and 4 respectively. Data was worked up by dividing the absorbance value at the absorbance maxima by the solution's concentration. Measurements from each trial were averaged together, and the standard deviation between trials was determined.

3.4.5. C_{60} Binding Studies

Fluorescence titration experiments were used to determine the association constant (K) between the CPP host (H) 2 and 4 and C60 guest (G). Stock solutions of 2, 4, and C60 were made in toluene at room temperature. Varying concentrations of the C60 solution were added to a known concentration of the CPP solution until fluorescence was quenched. All samples were excited at 340 nm. Emission spectra were collected from 345 nm - 800 nm and the fluorescence signal was

measured at 426 nm, 448 nm, and 474 nm for 2 and 381 nm, 429 nm, and 450 nm for 4. Open-source software BindFit was used to fit the data with the Nelder-Mead method.

The association constants were derived by applying a non-linear 1:1 and 2:1 binding model.

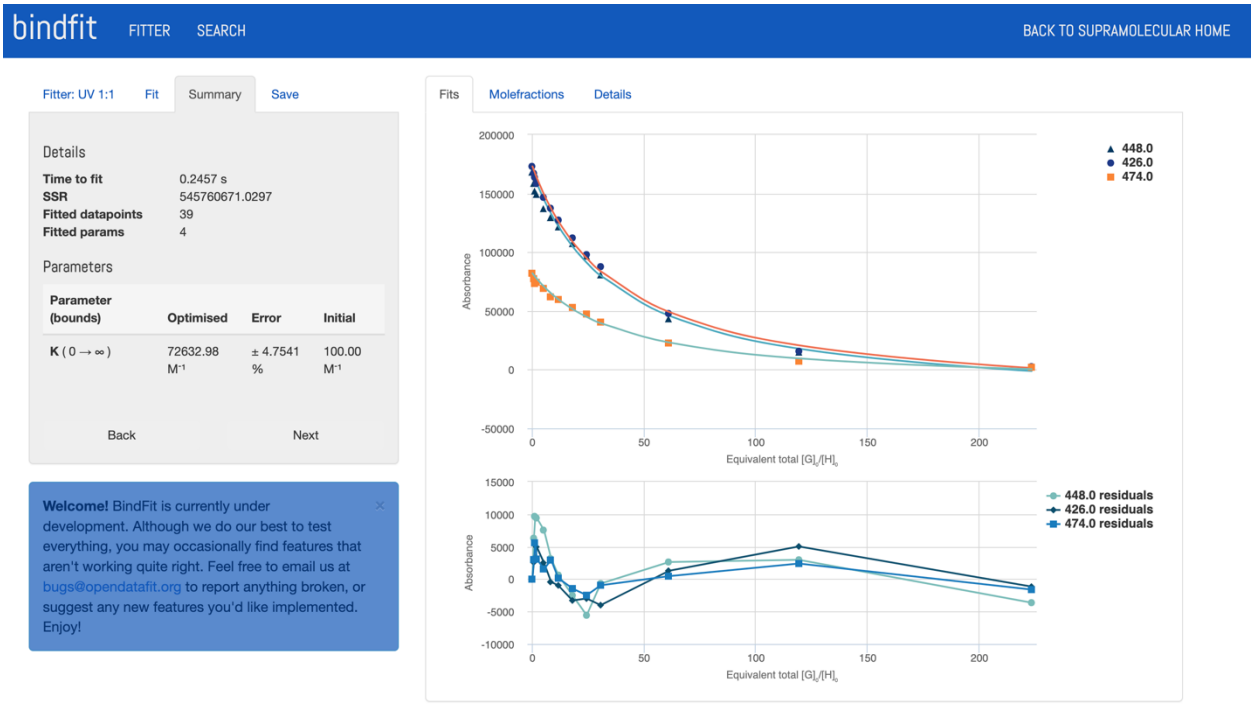

Figure 3.9. 1:1 binding constant for 2 and C60 calculated using BindFit.

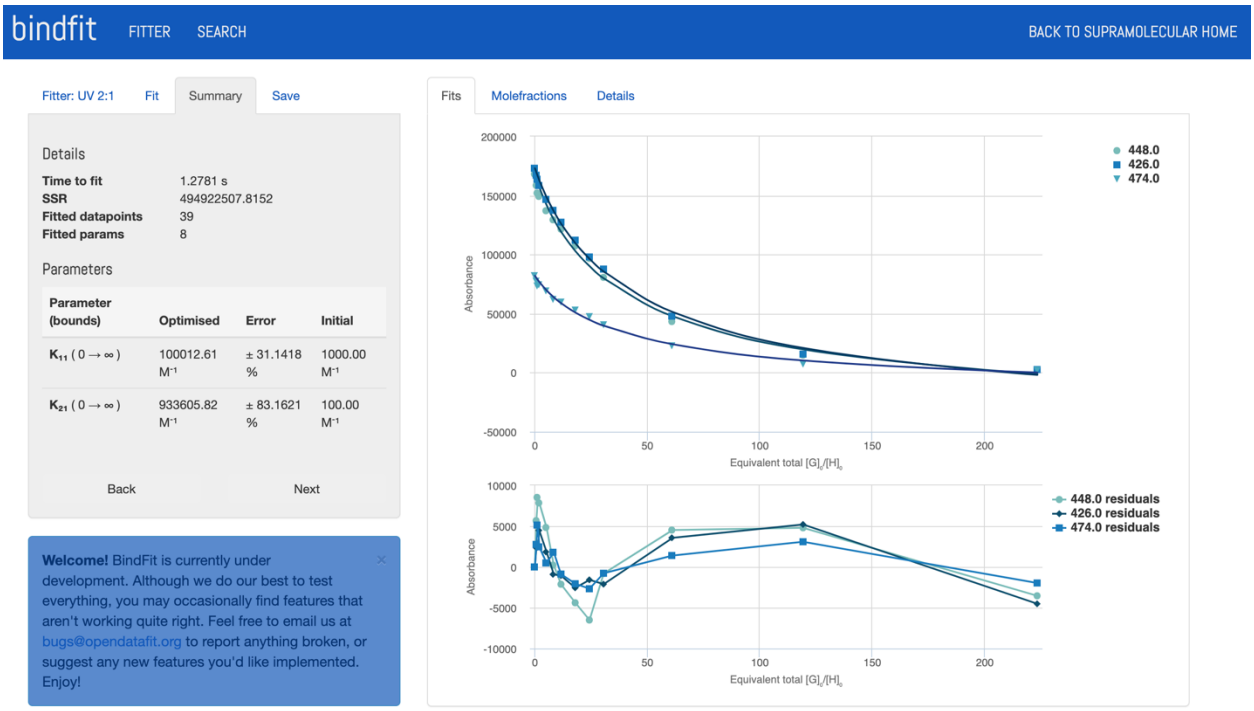

Figure 3.10. 2:1 binding constant for 2 and C60 calculated using BindFit.

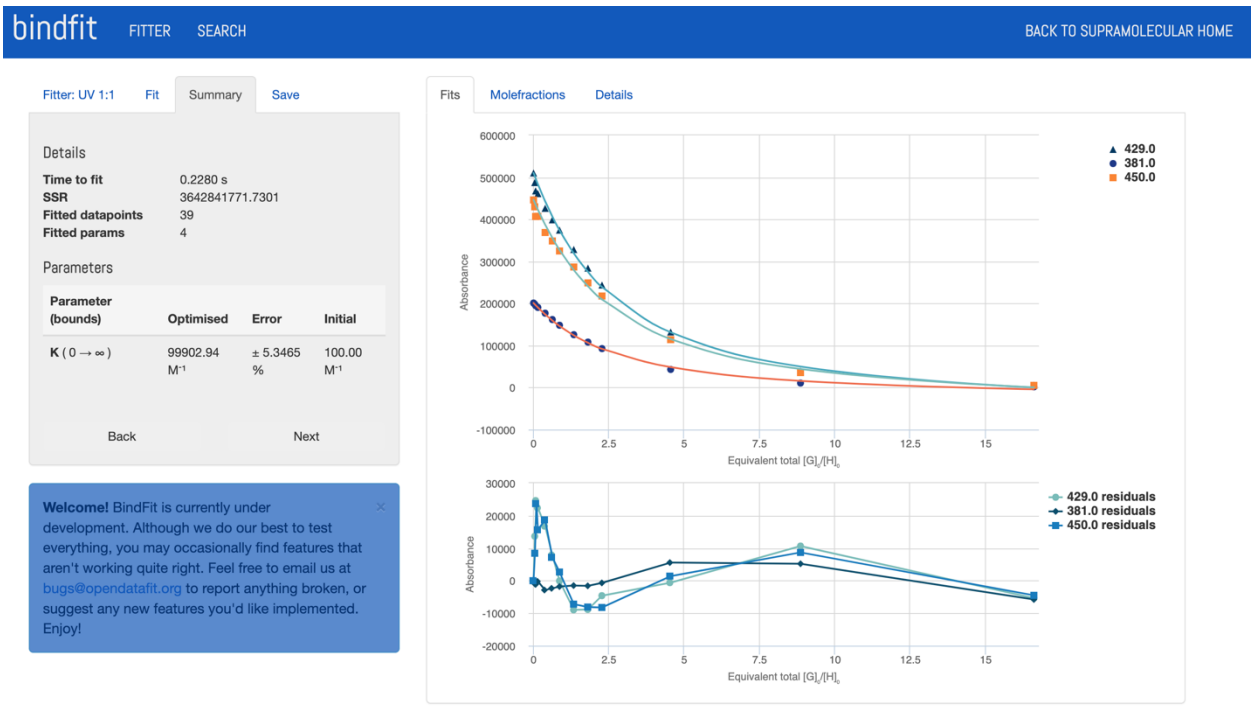

Figure 3.11. 1:1 binding constant for 4 and C60 calculated using BindFit.

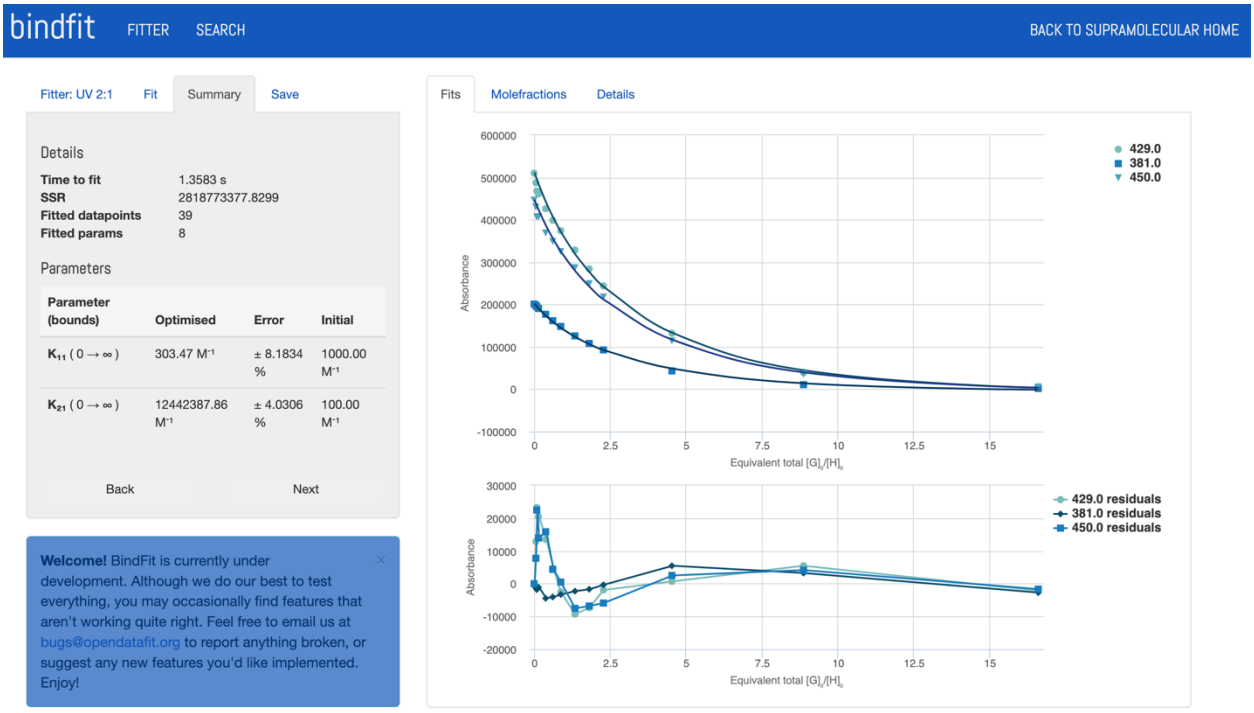

Figure 3.12. 2:1 binding constant for 2 and C60 calculated using BindFit.

3.4.6 Computational Details

Computational Methods:

All Gaussian output files for stationary points are available via Figshare with the following link, (INSERT Figshare Link).

Keywords –

a) Geometry Optimization

#n B3LYP/6-31G (d,p) Opt Freq

b) Vertical Transitions

#n B3LYP/6-31G(d,p) TD=NSTATES=12 scrf=(solvent=dichloromethane)

#n CAM-B3LYP/6-31G(d,p) Opt TD scrf=(solvent=dichloromethane)

Vertical transitions were determined using the time-dependent DFT method to probe excited states when exposed to an external field. Optical absorption spectra were observed for 12 states, and emission spectra were found by optimizing the time-dependent excited states.

Table 3.1 Optical absorption transitions for 2.

No.	Energy (cm-1)	Wavelength (nm)	Osc. Strength	Symmetry	Major Contributions
1	26474.34258	377.7242049	0.3397	Singlet-A	H-1->L+1 (12%), HOMO->LUMO (83%)
2	28127.77916	355.520425	2.3988	Singlet-A	H-1->LUMO (44%), HOMO->L+1 (48%)
3	29592.482	337.9236659	0.0078	Singlet-A	H-1->LUMO (51%), HOMO->L+1 (45%)

4	29978.82157	333.5688154	0.8715	Singlet-A	H-1->L+1 (62%), HOMO->L+2 (13%)
5	30803.1202	324.6424367	0.5565	Singlet-A	H-1->L+1 (16%), HOMO->L+2 (64%)
6	30954.75243	323.0521718	0.0147	Singlet-A	H-3->LUMO (44%), H-3->L+2 (15%), H-2->LUMO (13%)
7	31198.33187	320.5299579	0.0081	Singlet-A	H-3->L+1 (22%), H-3->L+3 (38%), H-2->L+3 (12%)
8	31294.31185	319.5468892	0.0912	Singlet-A	H-3->LUMO (21%), H-2->LUMO

					(53%), HOMO->L+2 (16%)
9	31980.68966	312.6886914	0.0063	Singlet-A	H-1->L+2 (13%), HOMO->L+3 (71%)
10	32057.31234	311.9413098	0.0078	Singlet-A	H-1->L+2 (77%)
11	32418.64872	308.46443	0.151	Singlet-A	H-3->L+1 (12%), H-2->L+1 (65%), HOMO->L+3 (11%)
12	32423.48805	308.4183906	0.0006	Singlet-A	H-3->L+1 (52%), H-3->L+3 (21%)

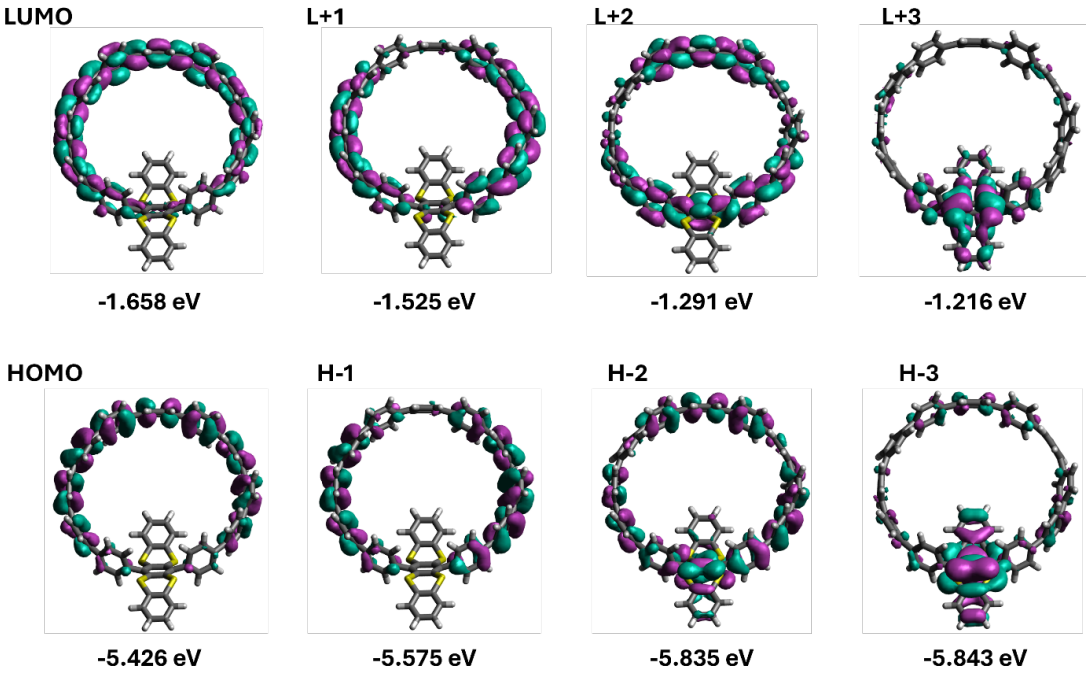

Figure 3.13. HOMO-LUMO orbital distribution of 2.

Table 3.2 Optical absorption transitions for 4.

No.	Energy (cm-1)	Wavelength (nm)	Osc. Strength	Symmetry	Major Contributions
1	29151.3	343	0.1798	Singlet-A	H-1->LUMO (36%), H-1->L+1 (14%)
2	29296.5	341	0.1835	Singlet-A	H-3->LUMO (27%), H-1->LUMO (12%), HOMO->LUMO (11%)
3	29387.6	340	0.0479	Singlet-A	H-2->LUMO (48%), HOMO->L+1 (13%)

4	30123.2	332	0.8993	Singlet-A	H-2->L+1 (17%), HOMO->LUMO (27%), HOMO->L+2 (18%)
5	30199.8	331	0.1445	Singlet-A	H-3->L+3 (14%), HOMO->L+3 (57%)
6	30453.1	328	0.0035	Singlet-A	H-3->L+5 (24%), H-1->L+5 (47%)
7	30547.4	327	0.0191	Singlet-A	H-3->L+4 (33%), H-1->L+4 (24%)
8	30647.5	326	0.4774	Singlet-A	H-4->LUMO (17%), H-2->L+1 (20%)
9	30832.2	324	0.9958	Singlet-A	H-5->LUMO (25%), H-2->L+2 (19%), HOMO->L+1 (16%)
10	31425.8	318	0.1251	Singlet-A	H-4->L+1 (14%), HOMO->L+1 (39%)
11	31638.7	316	0.0397	Singlet-A	H-3->L+2 (22%), H-1->L+1 (34%), HOMO->L+2 (11%)
12	31725.8	315	0.0205	Singlet-A	H-3->L+1 (17%), H-1->L+2 (33%)

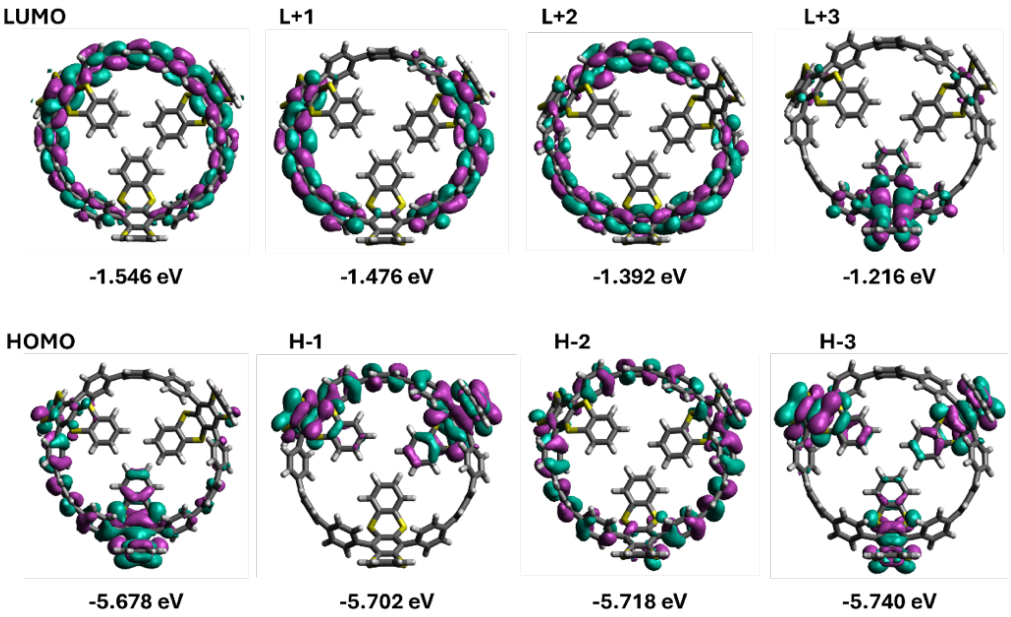

Figure 3.14. HOMO-LUMO orbital distribution of 4.

c) Binding Energy

#n M062X/6-31G(d,p) Opt Freq scrf=(solvent=toluene)

Binding energy calculations were performed using G09[44] at the M062X level of theory to compare to literature values of cycloparaphenylenes.[45] Frequency calculations were performed with the polarizable continuum model (PCM) to better represent toluene solvation. Binding analysis was performed by computing the difference of the sums of values for the reactants (Host, Guest) and products (Complex) to derive corrected Gibbs free energy values, see equation 1.[46] We see that as we increased the number of thianthrene units we can increase [12]CPPs binding to C60. M062X is known to overestimate binding energy, in the case for [10]CPP it is highly overestimated (ΔG°_{lit}=37 kj/mol, ~121% overestimate) perhaps due to closer H contacts. However, with substituted [12]CPP variations it appears to more closely estimate binding compared to experimental observations (~6 to 21% differences).

$$\Delta_r G°(298K) = \sum(\mathcal{E}_0 + G_{corr})_{\text{products}} - \sum(\mathcal{E}_0 + G_{corr})_{\text{reactants}} \quad (1)$$

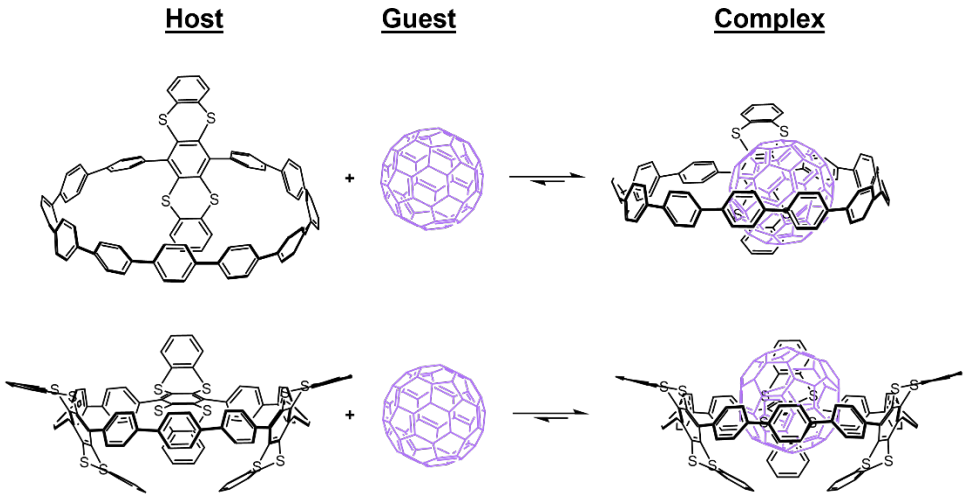

Figure 3.15. Host, guest, and host-guest complexes of 2, 4, and C_{60}

Table 3.3 DFT calculated binding favorability of CPP-fullerene complexes.

CPP Complex	ΔG (kJ/mol)	Total Error in DFT (%)
H10 DFT	-82	
H10 EXP	-37	121.6
2 DFT	-22	
2 EXP (1:1)	-27.7	-20.6
2 EXP (2:1)	-28	-21.4
4 DFT	-31	
4 EXP (1:1)	-29	6.9
4 EXP (2:1)	-38	-18.4

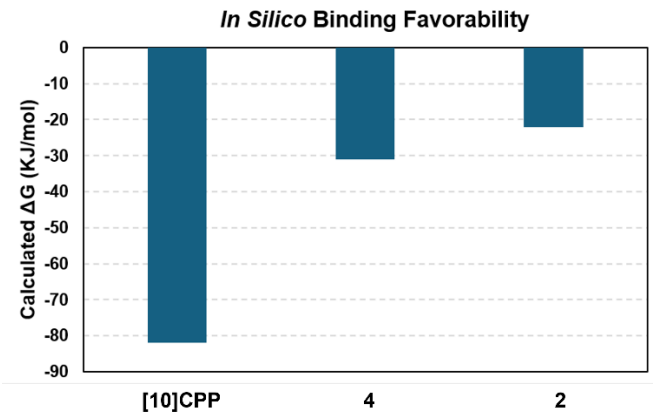

Figure 3.16. DFT calculated binding favorability of fullerene complexed with [10]CPP, 4, and 2.

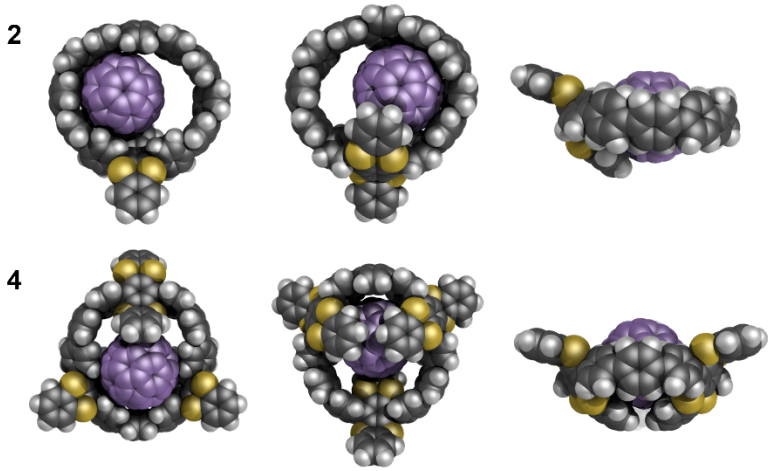

Figure 3.17. DFT calculated space-filling models of 2 and 4 complexing with C_{60}.

3.5 Bridge to Chapter IV

Chapter III focuses on late-stage approaches to efficiently introduce multiple non-planar, redox-active, sulfur-containing heterocycles to the CPP backbone. In Chapter IV we explore the efficient late-stage expansion of internal-alkyne-containing CPPs into trimeric multi-hoop structures.

3.6 References

(1) Darzi, E. R.; Jasti, R. The Dynamic, Size-Dependent Properties of [5]–[12]Cycloparaphenylenes. *Chem. Soc. Rev.* **2015**, *44* (18), 6401–6410. https://doi.org/10.1039/C5CS00143A.

(2) Fujitsuka, M.; Cho, D. W.; Iwamoto, T.; Yamago, S.; Majima, T. Size-Dependent Fluorescence Properties of [n]Cycloparaphenylenes (n = 8–13), Hoop-Shaped π-Conjugated Molecules. *Phys. Chem. Chem. Phys.* **2012**, *14* (42), 14585–14588. https://doi.org/10.1039/C2CP42712E.

(3) Jasti, R.; Bhattacharjee, J.; Neaton, J. B.; Bertozzi, C. R. Synthesis, Characterization, and Theory of [9]-, [12]-, and [18]Cycloparaphenylene: Carbon Nanohoop Structures. *J. Am. Chem. Soc.* **2008**, *130* (52), 17646–17647. https://doi.org/10.1021/ja807126u.

(4) Lovell, T. C.; Bolton, S. G.; Kenison, J. P.; Shangguan, J.; Otteson, C. E.; Civitci, F.; Nan, X.; Pluth, M. D.; Jasti, R. Subcellular Targeted Nanohoop for One- and Two-Photon Live Cell Imaging. *ACS Nano* **2021**, *15* (9), 15285–15293. https://doi.org/10.1021/acsnano.1c06070.

(5) Chen, D.; Wada, Y.; Kusakabe, Y.; Sun, L.; Kayahara, E.; Suzuki, K.; Tanaka, H.; Yamago, S.; Kaji, H.; Zysman-Colman, E. A Donor–Acceptor 10-Cycloparaphenylene and Its Use as an Emitter in an Organic Light-Emitting Diode. *Org. Lett.* **2023**, *25* (6), 998–1002. https://doi.org/10.1021/acs.orglett.3c00127.

(6) Lu, D.; Huang, Q.; Wang, S.; Wang, J.; Huang, P.; Du, P. The Supramolecular Chemistry of Cycloparaphenylenes and Their Analogs. *Front. Chem.* **2019**, *7*.

(7) Peters, G. M.; Grover, G.; Maust, R. L.; Colwell, C. E.; Bates, H.; Edgell, W. A.; Jasti, R.; Kertesz, M.; Tovar, J. D. Linear and Radial Conjugation in Extended π-Electron Systems. *J. Am. Chem. Soc.* **2020**, *142* (5), 2293–2300. https://doi.org/10.1021/jacs.9b10785.

(8) Zhang, J.; Cheng, H.; Meng, Z.; Zhang, H.; Luo, Z.; Muddassir, M.; Li, X.; Sha, Y. Side-Chain Meta [6]Cycloparaphenylene-Based Nanoring-Containing Polymers. *Polym. Chem.* **2023**, *14* (45), 5029–5033. https://doi.org/10.1039/D3PY01058A.

(9) Heras Ojea, M. J.; Van Raden, J. M.; Louie, S.; Collins, R.; Pividori, D.; Cirera, J.; Meyer, K.; Jasti, R.; Layfield, R. A. Spin-Crossover Properties of an Iron(II) Coordination Nanohoop. *Angew. Chem. Int. Ed.* **2021**, *60* (7), 3515–3518. https://doi.org/10.1002/anie.202013374.

(10) Van Raden, J. M.; Louie, S.; Zakharov, L. N.; Jasti, R. 2,2′-Bipyridyl-Embedded Cycloparaphenylenes as a General Strategy To Investigate Nanohoop-Based Coordination Complexes. *J. Am. Chem. Soc.* **2017**, *139* (8), 2936–2939. https://doi.org/10.1021/jacs.7b00359.

(11) A. Kamin, A.; D. Clayton, T.; E. Otteson, C.; M. Gannon, P.; Krajewski, S.; Kaminsky, W.; Jasti, R.; J. Xiao, D. Synthesis and Metalation of Polycatechol Nanohoops Derived from Fluorocycloparaphenylenes. *Chem. Sci.* **2023**, *14* (36), 9724–9732. https://doi.org/10.1039/D3SC03561A.

(12) Kayahara, E.; Patel, V. K.; Mercier, A.; Kündig, E. P.; Yamago, S. Regioselective Synthesis and Characterization of Multinuclear Convex-Bound Ruthenium-[n]Cycloparaphenylene (N=5 and 6) Complexes. *Angew. Chem. Int. Ed.* **2016**, *55* (1), 302–306. https://doi.org/10.1002/anie.201508003.

(13) Lv, Y.; Lin, J.; Song, K.; Song, X.; Zang, H.; Zang, Y.; Zhu, D. Single Cycloparaphenylene Molecule Devices: Achieving Large Conductance Modulation via Tuning Radial π-Conjugation. *Sci. Adv. 7* (52), eabk3095. https://doi.org/10.1126/sciadv.abk3095.
(14) Roy, R.; Brouillac, C.; Jacques, E.; Quinton, C.; Poriel, C. π-Conjugated Nanohoops: A New Generation of Curved Materials for Organic Electronics. *Angew. Chem.* **2024**, *136* (30), e202402608. https://doi.org/10.1002/ange.202402608.
(15) Leonhardt, E. J.; Jasti, R. Emerging Applications of Carbon Nanohoops. *Nat. Rev. Chem.* **2019**, *3* (12), 672–686. https://doi.org/10.1038/s41570-019-0140-0.
(16) Terabayashi, T.; Kayahara, E.; Zhang, Y.; Mizuhata, Y.; Tokitoh, N.; Nishinaga, T.; Kato, T.; Yamago, S. Synthesis of Twisted [n]Cycloparaphenylene by Alkene Insertion. *Angew. Chem. Int. Ed.* **2023**, *62* (2), e202214960. https://doi.org/10.1002/anie.202214960.
(17) Shudo, H.; Kuwayama, M.; Segawa, Y.; Yagi, A.; Itami, K. Half-Substituted Fluorocycloparaphenylenes with High Symmetry: Synthesis, Properties and Derivatization to Densely Substituted Carbon Nanorings. *Chem. Commun.* **2023**, *59* (90), 13494–13497. https://doi.org/10.1039/D3CC04887J.
(18) Mohamed, M. G.; Chaganti, S. V.; Li, M.-S.; Samy, M. M.; Sharma, S. U.; Lee, J.-T.; Elsayed, M. H.; Chou, H.-H.; Kuo, S.-W. Ultrastable Porous Organic Polymers Containing Thianthrene and Pyrene Units as Organic Electrode Materials for Supercapacitors. *ACS Appl. Energy Mater.* **2022**, *5* (5), 6442–6452. https://doi.org/10.1021/acsaem.2c00942.
(19) E. Speer, M.; Kolek, M.; Jacques Jassoy, J.; Heine, J.; Winter, M.; M. Bieker, P.; Esser, B. Thianthrene-Functionalized Polynorbornenes as High-Voltage Materials for Organic Cathode-Based Dual-Ion Batteries. *Chem. Commun.* **2015**, *51* (83), 15261–15264. https://doi.org/10.1039/C5CC04932F.
(20) Ren, J.; Wang, X.; Liu, H.; Hu, Y.; Zhang, X.; Masuda, T. Poly(Phenylacetylene)s Bearing Thianthrene Groups as High-Voltage Organic Cathode Materials for Lithium Batteries. *React. Funct. Polym.* **2020**, *146*, 104365. https://doi.org/10.1016/j.reactfunctpolym.2019.104365.
(21) Pander, P.; Swist, A.; Soloducho, J.; Dias, F. B. Room Temperature Phosphorescence Lifetime and Spectrum Tuning of Substituted Thianthrenes. *Dyes Pigments* **2017**, *142*, 315–322. https://doi.org/10.1016/j.dyepig.2017.03.049.
(22) Wen, Y.; Liu, H.; Zhang, S.-T.; Pan, G.; Yang, Z.; Lu, T.; Li, B.; Cao, J.; Yang, B. Modulating Room Temperature Phosphorescence by Oxidation of Thianthrene to Achieve Pure Organic Single-Molecule White-Light Emission. *CCS Chem.* **2020**, *3* (7), 1940–1948. https://doi.org/10.31635/ccschem.020.202000433.
(23) Yang, Z.; Zhao, S.; Zhang, X.; Liu, M.; Liu, H.; Yang, B. Efficient Room-Temperature Phosphorescence from Discrete Molecules Based on Thianthrene Derivatives for Oxygen Sensing and Detection. *Front. Chem.* **2022**, *9*. https://doi.org/10.3389/fchem.2021.810304.
(24) Li, N.; Wang, Y.; Li, Z. Photo-Induced Room Temperature Phosphorescence and Thermally Activated Photochromism Based on Thianthrene Derivatives. *J. Mater. Chem. C* **2024**, *12* (31), 12045–12053. https://doi.org/10.1039/D4TC02034K.
(25) Yuan, J.; Lv, W.; Li, A.; Zhu, K. A Self-Assembled M2L2 Truncated Square and Its Application as a Container for Fullerenes. *Chem. Commun.* **2021**, *57* (95), 12848–12851. https://doi.org/10.1039/D1CC05581J.
(26) Georghiou, P. E.; Dawe, L. N.; Tran, H.-A.; Strübe, J.; Neumann, B.; Stammler, H.-G.; Kuck, D. C3v-Symmetrical Tribenzotriquinacenes as Hosts for C60 and C70 in Solution

and in the Solid State. *J. Org. Chem.* **2008**, *73* (22), 9040–9047. https://doi.org/10.1021/jo801782z.
(27) Amthor, S.; Lambert, C.; Graser, B.; Leusser, D.; Selinka, C.; Stalke, D. Synthesis and Ligand Properties of Thianthrenophane. *Org. Biomol. Chem.* **2004**, *2* (20), 2897–2901. https://doi.org/10.1039/B407048H.
(28) Georghiou, P. E.; Tran, A. H.; Mizyed, S.; Bancu, M.; Scott, L. T. Concave Polyarenes with Sulfide-Linked Flaps and Tentacles: New Electron-Rich Hosts for Fullerenes. *J. Org. Chem.* **2005**, *70* (16), 6158–6163. https://doi.org/10.1021/jo0503761.
(29) Heiska, J.; Nisula, M.; Karppinen, M. Organic Electrode Materials with Solid-State Battery Technology. *J. Mater. Chem. A* **2019**, *7* (32), 18735–18758. https://doi.org/10.1039/C9TA04328D.
(30) Etkind, S. I.; Swager, T. M. The Properties, Synthesis, and Materials Applications of 1,4-Dithiins and Thianthrenes. *Synthesis* **2022**, 4843–4863. https://doi.org/10.1055/s-0042-1751368.
(31) Burkhart, C.; Haberhauer, G. A Light- and Electricity-Driven Molecular Pushing Motor. *Eur. J. Org. Chem.* **2017**, *2017* (10), 1308–1317. https://doi.org/10.1002/ejoc.201601371.
(32) Wild, A.; Strumpf, M.; Häupler, B.; Hager, M. D.; Schubert, U. S. All-Organic Battery Composed of Thianthrene- and TCAQ-Based Polymers. *Adv. Energy Mater.* **2017**, *7* (5), 1601415. https://doi.org/10.1002/aenm.201601415.
(33) Wang, S.; Yuan, J.; Xie, J.; Lu, Z.; Jiang, L.; Mu, Y.; Huo, Y.; Tsuchido, Y.; Zhu, K. Sulphur-Embedded Hydrocarbon Belts: Synthesis, Structure and Redox Chemistry of Cyclothianthrenes. *Angew. Chem.* **2021**, *133* (34), 18591–18595. https://doi.org/10.1002/ange.202104054.
(34) Ong, W. J.; Swager, T. M. Dynamic Self-Correcting Nucleophilic Aromatic Substitution. *Nat. Chem.* **2018**, *10* (10), 1023–1030. https://doi.org/10.1038/s41557-018-0122-8.
(35) Leonhardt, E. J.; Van Raden, J. M.; Miller, D.; Zakharov, L. N.; Alemán, B.; Jasti, R. A Bottom-Up Approach to Solution-Processed, Atomically Precise Graphitic Cylinders on Graphite. *Nano Lett.* **2018**, *18* (12), 7991–7997. https://doi.org/10.1021/acs.nanolett.8b03979.
(36) Van Raden, J. M.; Leonhardt, E. J.; Zakharov, L. N.; Pérez-Guardiola, A.; Pérez-Jiménez, A. J.; Marshall, C. R.; Brozek, C. K.; Sancho-García, J. C.; Jasti, R. Precision Nanotube Mimics via Self-Assembly of Programmed Carbon Nanohoops. *J. Org. Chem.* **2020**, *85* (1), 129–141. https://doi.org/10.1021/acs.joc.9b02340.
(37) Lovell, T. C.; Colwell, C. E.; Zakharov, L. N.; Jasti, R. Symmetry Breaking and the Turn-on Fluorescence of Small, Highly Strained Carbon Nanohoops. *Chem. Sci.* **2019**, *10* (13), 3786–3790. https://doi.org/10.1039/C9SC00169G.
(38) Kuwabara, T.; Orii, J.; Segawa, Y.; Itami, K. Curved Oligophenylenes as Donors in ShapePersistent DonorAcceptor Macrocycles with Solvatofluorochromic Properties. *Angew Chem* **2015**, 4.
(39) Lovell, T. C.; Garrison, Z. R.; Jasti, R. Synthesis, Characterization, and Computational Investigation of Bright Orange-Emitting Benzothiadiazole [10]Cycloparaphenylene. *Angew. Chem. Int. Ed.* **2020**, *59* (34), 14363–14367. https://doi.org/10.1002/anie.202006350.
(40) Schaub, T. A.; Margraf, J. T.; Zakharov, L.; Reuter, K.; Jasti, R. Strain-Promoted Reactivity of Alkyne-Containing Cycloparaphenylenes. *Angew. Chem. Int. Ed.* **2018**, *57* (50), 16348–16353. https://doi.org/10.1002/anie.201808611.

(41) Bruno, N. C.; Tudge, M. T.; Buchwald, S. L. Design and Preparation of New Palladium Precatalysts for C–C and C–N Cross-Coupling Reactions. *Chem. Sci.* **2013**, *4* (3), 916–920. https://doi.org/10.1039/C2SC20903A.
(42) Fehr, J. M.; Myrthil, N.; Garrison, A. L.; Price, T. W.; Lopez, S. A.; Jasti, R. Experimental and Theoretical Elucidation of SPAAC Kinetics for Strained Alkyne-Containing Cycloparaphenylenes. *Chem. Sci.* **2023**, *14* (11), 2839–2848. https://doi.org/10.1039/D2SC06816H.
(43) Pangborn, A. B.; Giardello, M. A.; Grubbs, R. H.; Rosen, R. K.; Timmers, F. J. Safe and Convenient Procedure for Solvent Purification. *Organometallics* **1996**, *15* (5), 1518–1520. https://doi.org/10.1021/om9503712.
(44) *Citation | Gaussian.com*. https://gaussian.com/citation/ (accessed 2024-12-19).
(45) Iwamoto, T.; Watanabe, Y.; Sadahiro, T.; Haino, T.; Yamago, S. Size-Selective Encapsulation of C60 by [10]Cycloparaphenylene: Formation of the Shortest Fullerene-Peapod. *Angew. Chem. Int. Ed.* **2011**, *50* (36), 8342–8344. https://doi.org/10.1002/anie.201102302.
(46) Ochterski, J. W. Thermochemistry in Gaussian.

CHAPTER IV

PINWHEEL-LIKE CURVED AROMATICS FROM THE CYCLOTRIMERIZATION OF STRAINED-ALKYNE CYCLOPARAPHENYLENES

Chapter IV is adapted from a study published in Journal of the American Chemical Society entitled "Pinwheel-Like Curved Aromatics from the Cyclotrimerization of Strained-Alkyne Cycloparaphenylenes." Trimeric CPPs **7** and **9** were synthesized and characterized by me, and trimeric CPPs **3** and **5** were synthesized and characterized by Dr. Julia Fehr. StrainViz calculations were performed by Dr. Tavis Price. The manuscript was written Dr. Julia Fehr and I and with edits from Dr. Tavis Price and Professor Ramesh Jasti. Professor Ramesh Jasti provided guidance on the project.

4.1 Introduction

Curved aromatic hydrocarbons are a useful and continuously evolving class of carbon nanomaterials. Their deviation from the flat, planar structure expected of aromatic molecules can grant them advantages such as: (1) narrower HOMO–LUMO gaps with increasing strain,[1] (2) heightened solubility due to less efficient self-stacking,[2] and (3) complementary intermolecular interactions such as convex-–concave pi-interactions.[3,4] Since the landmark discoveries of fullerenes and carbon nanotubes,[5,6] many structural variants of curved aromatic hydrocarbons have been synthesized. Small molecules such as helicenes, corannulenes, saddle-shaped polyaromatics, and a variety of conjugated macrocycles are now accessible *via* controlled, bottom-up synthetic methods.[7] Efficient methods of derivatizing and extending these smaller fragments of curved carbon nanomaterials are crucial, as the properties and potential applications of pi-rich molecules rely heavily on dimensionality, size, crystal morphology, etc. However, structural

modifications of strained aromatics can be challenging, particularly due to strain-relieving pathways leading to undesired side products.

In the last several years a class of synthetically tunable curved aromatic hydrocarbons, carbon nanohoops, have garnered much attention from the broader scientific community.[7–13] Carbon nanohoops (also known as cycloparaphenylenes and abbreviated [*n*]CPP where *n* = number of phenylene units) are strained aromatic macrocycles that represent the smallest cross-section of an armchair carbon nanotube.[14] Many molecules in this class have shape-persistent pores with host–-guest capabilities,[3,4] are redox active,[13,15–18] brightly fluorescent,[15] possess excellent solubility in most organic solvents,[15] and have syntheses which are highly modular and tunable; this has enabled the study of nanohoops of many different sizes, shapes, functionalities, and properties.[7–13,19]

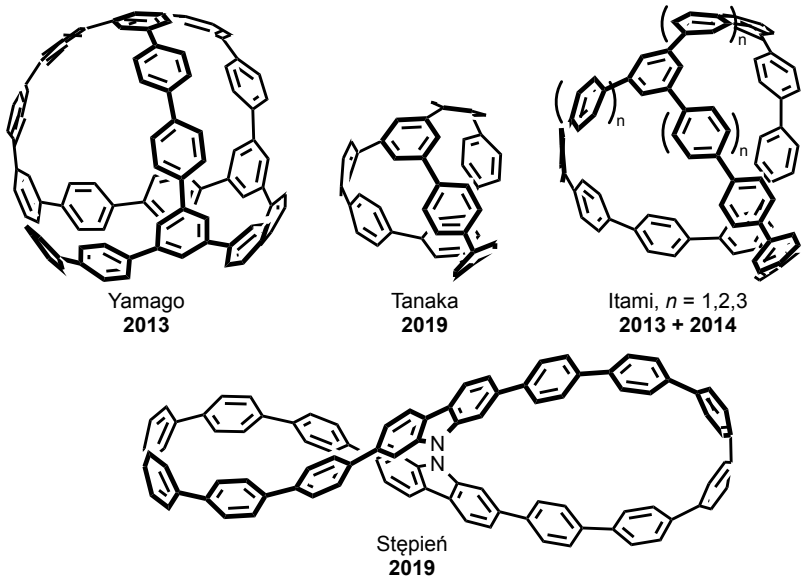

Figure 4.1. Representative examples of multi-pore nanohoop like structures.

A growing area of CPP research aims to controllably extend the strained scaffold into novel pi-rich systems, such as cages, mechanically interlocked molecules (MIMs), supramolecular

complexes, discrete oligomers, and high molecular weight polymers.[20–24] Specifically, several recent publications have showcased the syntheses[25–30] of cycloparaphenylene-like structures with multiple hoops incorporated within one molecule (see **Figure 4.1** for a few representative examples). The synthetic strategies of these extended CPP derivatives, however, typically use early-stage functionalization to build multi-pore precursors, which are aromatized to the final molecule often in low yield. Much less prevalent are examples of CPPs undergoing late-stage transformations, a synthetic strategy that circumvents restrictive pre-functionalization and should afford easier access to further derivation.

Our group has recently focused on the synthesis and study of [*n*+1]CPPs,[31] wherein the "+1" refers to the incorporation of a single alkyne unit inserted in the macrocyclic backbone providing a synthetic handle for further reactivity. We have shown that these [*n*+1]CPPs have tunable reactivity towards strain-promoted [2+2]cycloadditions/cycloreversions and [3+2]azide-alkyne cycloadditions ,[31–33] but other strain-promoted transformations that may lead to multi-pore structures have not been reported.[33] The present work explores the [2+2+2] alkyne cyclotrimerization of a series of [*n*+1]CPPs. While the formation of benzene derivatives *via* transition metal catalyzed [2+2+2] cycloaddition of alkynes has been known for over 70 years,[34] typically these reactions require elevated temperatures and long reaction times.[35] Inspired by related reactions with arynes[36,37] and small, strained cycloalkynes,[38] herein, we demonstrate the first examples of strain-promoted [2+2+2] cyclotrimerizations of alkyne-containing macrocyclic precursors to realize large, highly fluorescent, and soluble carbon nanostructures. This is a highly efficient late-stage transformation affording large curved aromatic molecules wherein three CPP fragments are linked in two dimensions around a newly formed central benzene unit (**Scheme 4.1**). Coupled with the well-established building block approach to nanohoop derivatives and the ease

of preparation of most [*n*+1]CPPs, this methodology provides access to an array of new structures that are interesting for potential applications in molecular electronics, extended supramolecular complexes, and porous carbon nanomaterials.[39]

4.2 Results and Discussion

4.2.1 Synthesis

Our most recent work with the [n+1]CPPs focused on increasing reactivity towards the strain-promoted azide–alkyne cycloaddition (SPAAC) reaction by (1) the introduction of electron-withdrawing fluorine atoms near the strained alkyne, and (2) the installation of a *meta*-linked phenylene into the nanohoop opposite the alkyne.[32] At that time we were

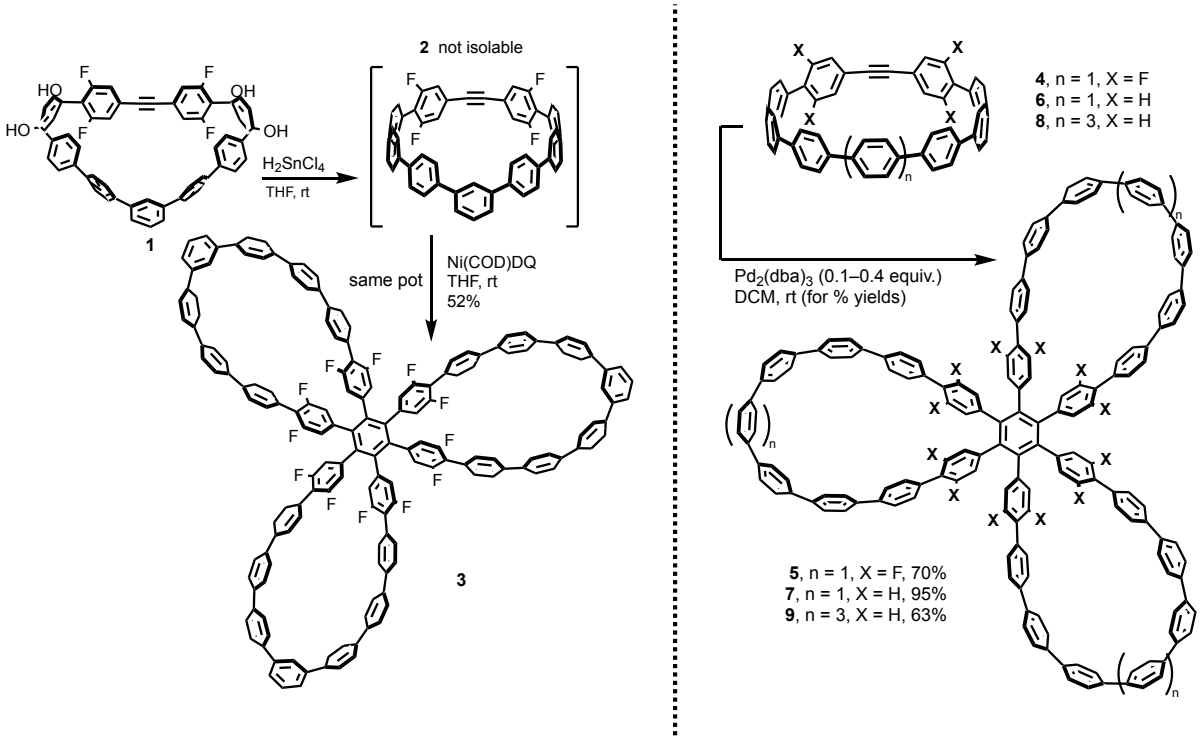

Scheme 4.1. Conversion of [*n*+1]CPPs to trimers. **2** is not stable enough for isolation, however, can be converted to **3** upon formation. **4** was chosen as a model system to assess the effectiveness of metal catalysts on the reaction (see **Table 4.1**). Percent yields refer to optimized conditions with $Pd_2(dba)_3$.

unable to isolate the highly strained and electronically activated CPP **2** (**Scheme 4.1**) due to its

propensity to decompose and/or react immediately under the reaction conditions. Gratifyingly, we were later able to identify the trimeric species **3** (**Scheme 4.1**) as one of the byproducts of the highly reactive **2**. With knowledge of the reactivities, photophysical characteristics, and host-guest capabilities of the previously synthesized [*n*+1]CPPs in mind, we chose four species with increasingly reactive alkyne units for this study: the **8, 6, 4**, and **2**. We hypothesized that the transient **2** and other alkyne-containing CPPs could be efficiently trimerized with the addition of an appropriate metal catalyst.

We first focused our attention on the synthesis of the fully *para*-linked fluorinated internal-alkyne CPP **4** (**Scheme 4.1**) using a combination of previously described[31,32] molecular building blocks (see SI for full synthetic details). We found that **4** could be isolated effectively under the same reaction and purification conditions which had proved unsuccessful for **2**. Interestingly, we would occasionally observe slow conversion of **4** to **5** if the sample was kept as a solution in possibly metal-contaminated glassware and/or had not yet been rigorously purified. This finding, along with that of **2** forming trimer without added catalyst, suggests that the [2+2+2] alkyne trimerization of [*n*+1]CPPs might be strain-promoted.

With the comparatively more stable **4** in hand, we turned our attention to better understanding the nature of the trimerization reaction. Under inert atmosphere at room temperature with new and pristine glassware in deuterated chloroform ($CDCl_3$), we treated **4** with different metal catalysts (approximately 20% catalyst loading) for one hour and assessed the results of each reaction with quantitative ^{19}F NMR (**Table 4.1** and **Scheme 4.1**). The screened metal complexes are well-known catalysts for alkyne trimerization; Rh(I)[40,41] and Ni(0)[42–44] are common catalysts for the trimerization of unstrained alkynes, while Pd(0)[36,38,45] is

often an effective catalyst for aryne trimerization.

Table 4.1. Metal screening results for conversion of **4** to **5**.

metal	conversion (%)
none	0.5
$Pd_2(dba)_3$	99.9
$RhCl(PPh_3)_3$	6.3
Ni(cod)DQ	11.5

Reactions carried out in $CDCl_3$ at room temperature for 1 h under inert atmosphere with 1.9 mM **4**, 0.39 mM metal. Conversions determined by quantitative ^{19}F NMR.

We found that $Pd_2(dba)_3$ was by far the most efficient catalyst for the transformation of **4** to **5**, with a calculated percent conversion of over 99% (with these conditions, we achieved 70% isolated yield in a separate experiment). $RhCl(PPh_3)_3$ and Ni(cod)DQ performed much more modestly at 6.3% and 11.5% conversion, respectively.

This apparent catalyst preference is similar to that observed by Peña et al in their investigations of cyclohexyne trimerization.[38] Notably, we observed less than 0.5% conversion of **4** to **5** in an hour-long, room temperature control experiment with no added metal (first entry of **Table 4.1**). In a separate control experiment, we found that diphenylacetylene (an unstrained, phenyl-substituted alkyne) showed no reaction under the same

conditions with $Pd_2(dba)_3$ (see SI for details). These results are consistent with our hypothesis that the cyclotrimerization of the [*n*+1]CPPs with Pd(0) is strain-promoted. Bennett et al have shown that cyclooctyne, the smallest isolable unsubstituted cycloalkyne, has increased complexation towards transition metal compounds compared to acyclic alkynes.[46] As a result, cyclooctyne undergoes transition metal-catalyzed cyclotrimerization far more readily than acyclic alkynes. We hypothesize that our strained alkyne-containing CPPs may also benefit from enhanced transition metal complexation, affording complete conversion to trimeric species in minutes at room temperature.

We next questioned whether less reactive [*n*+1]CPPs could undergo cyclotrimerization under the same conditions. To assess whether electron-withdrawing fluorine atoms were necessary for the transformation, we combined **6** and catalytic $Pd_2(dba)_3$ and found that alkyne cyclotrimerization occurred efficiently to form **7** in 95% isolated yield. To investigate if less strained [*n*+1]CPPs were also capable of this transformation, we subsequently treated **8** with $Pd_2(dba)_3$ and found that **9** could be isolated in 63% yield. While we found that **7**, **5**, and **3** all possessed excellent solubility in a range of organic solvents, **9** suffered from a lack of significant solubility in most solvents, which likely contributed to its diminished isolated yield. Despite difficulties during isolation, the crude NMR of the trimerization of **8** shows clean and complete conversion to **9**.

Finally, we turned our attention back to a more efficient synthesis of **3**. After testing several methods, we found that we could reliably form **3** by adding 1.5 equivalents of Ni(cod)DQ directly to the reductive aromatization reaction of **2**. This allowed us to form **3** in up to 52% yield from **1** after purification.

4.2.2 X-ray Crystallographic Analysis

We confirmed the identity and connectivity of **3** and **5** *via* X-ray crystal analysis (unit cells shown in **Figure 4.2**). Crystals of **5** were formed from the slow evaporation of 1,4-dioxane. Crystals of **3** were formed from vapor diffusion of pentanes into 1,4-dioxane. In both cases, precise structural information could not be determined due to a high number of disordered solvent molecules. However, the X-ray data was sufficient to confirm the correct assignment of both molecules and assign a space group ($P\bar{1}$ for **5** and $R\bar{3}$ for **3**) for each crystal packing pattern. Notably, **3** packs into an interdigitated structure with long-range, solvent-filled channels.

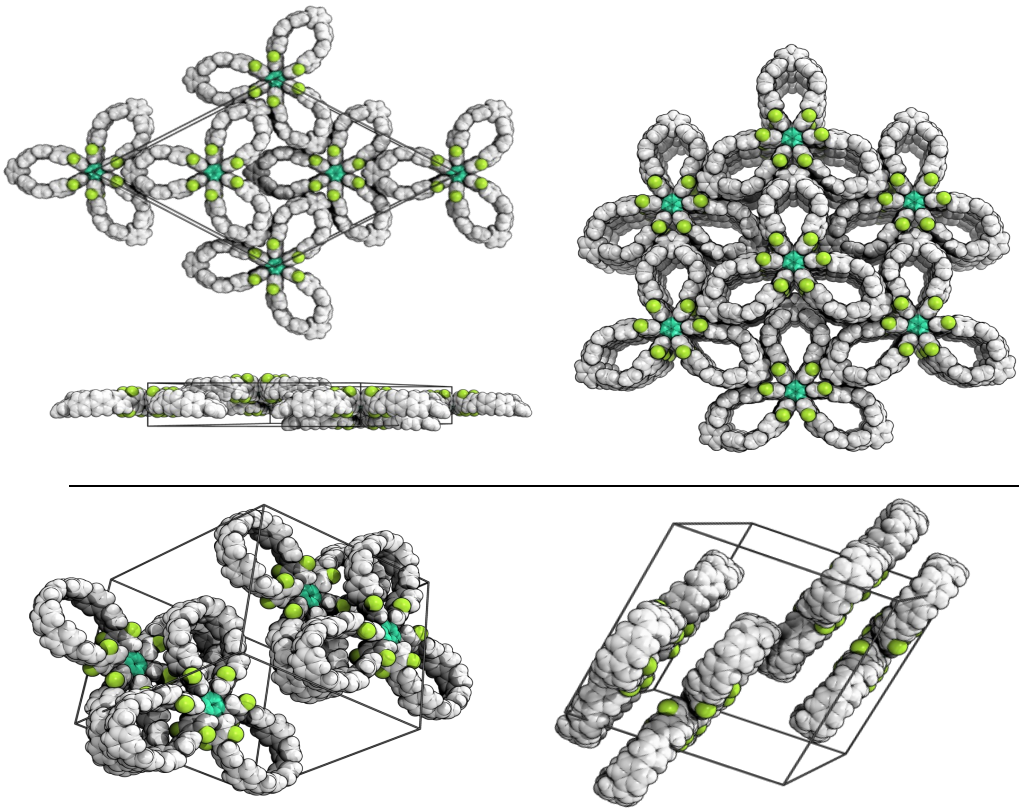

Figure 4.2. X-ray crystal structure unit cells of **3 (a)** and **5 (b)**. Solvent is emitted for clarity.

While we were not able to grow suitable single crystals of **7** and **9**, spectroscopic evidence is consistent with the structural assignment. **Figure 4.3** shows the ^{1}H NMR spectra in deuterated dichloromethane (CD_2Cl_2) for each of the trimers described herein as well as relevant [*n*+1]CPPs. For [*n*+1]CPPs, we typically observe a distinctive upfield doublet representative of the hydrogens *ortho* to the alkyne (shown generically as H_A in **Figure 4.3**).[31,32] For non-fluorinated **7** and **9**, another upfield doublet, likely representative of the hydrogens *meta* to the alkyne (H_B in **Figure 4.3**), can also be observed. Upon trimerization of **4**, an upfield shift of the H_A doublet occurred from 6.96 ([*n*+1]CPP) to 6.65 ppm (trimer). Notably, the H_A doublets of **6** and **8** experience very

comparable shifts upon trimerization (7.36 to 6.99 ppm for **6** to **7**, and 7.45 to 7.05 ppm for **8** to **9**). In these

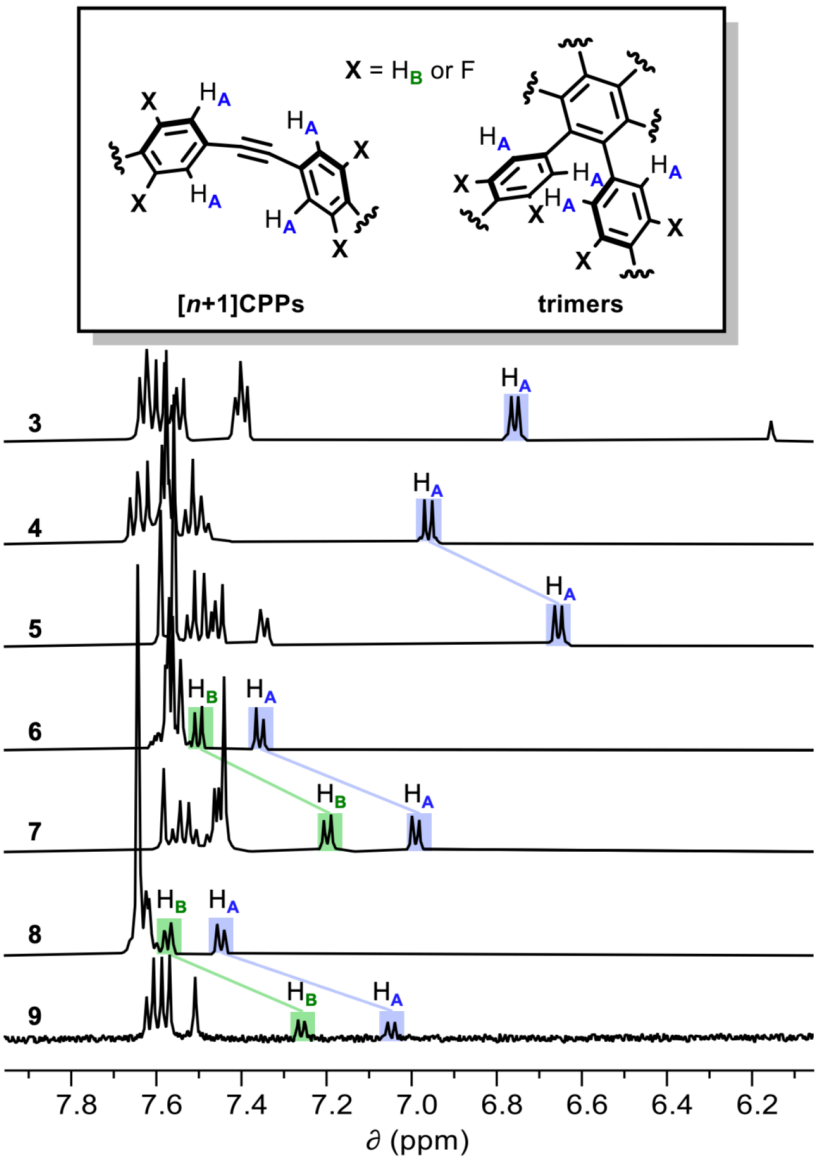

Figure 4.3. Diagnostic ^{1}H NMR shifts for trimers and associated [*n*+1]CPPs in CD_2Cl_2.

cases, we can also note the upfield shift of the H_B signal; the doublet representing H_B shifts from 7.50 ppm for **6** to 7.20 ppm for **7**, and from 7.57 ppm for **8** to 7.26 ppm for **9**. Further NMR evidence for successful trimerization can be found in the ^{13}C NMR (see SI for full details). In these

spectra, we see a disappearance of any signals below 120 ppm, indicating the lack of an alkyne in the product (the alkyne signals for **4**, **6**, and **8** in CD_2Cl_2 are observed at 99.24 ppm, 99.39 ppm, and 97.10 ppm, respectively). In addition to NMR spectroscopic evidence, high resolution mass spectrometry of **3**, **5**, **7**, and **9** resulted in the correct ion masses.

4.2.3 StrainViz Analysis

We next worked to better understand the total strain and distribution of local strain in these new nanohoop derivatives. We used the computational program StrainViz to calculate and visualize the local and total strain of each trimer and its parent [*n*+1]CPP (**Table 4.2** and **Figure 4.4**).[48] For the [*n*+1]CPPs, local strain is greatest at the alkyne as has been shown previously.[32,48]

Table 4.2. Quantitative strain data as determined by StrainViz (all values in kcal mol^{-1}). Computations performed with Gaussian 09 at the B3LYP/6-31G(d) level of theory.[47]

compound	max. local strain	total strain
3	1.8	80.5
5	3.1	130.3
7	3.1	129.3
9	2.3	112.8
2	3.4	42.9
4	2.8	55.6
6	2.9	58.0
8	1.3	44.4

For the trimers, however, local strain is greatest at the phenylene units opposite the newly formed *ortho* linkage—this is consistent with our understanding of how strain is distributed in these types of macrocycles.[48] Additionally, the trimmers have total strain values equivalent to less than three times the total strain of the precursor [*n*+1]CPPs. For example, **5** has a calculated 130 kcal mol^{-1} of inherent strain, whereas **4** has 56 kcal mol^{-1}. These findings indicate that the inherent strain per macrocyclic unit decreases post-trimerization. We also note that **2**, which has the highest calculated maximum local strain value of the [*n*+1]CPPs in this study at 3.4 kcal mol^{-1}, trimerizes

to form the most locally and globally unstrained trimer in this series, **3**. The *meta* linkage serves to heighten strain in nanohoops at the region of the molecule directly across from it,[48] but post-trimerization the newly formed *ortho*-linkage ameliorates this effect.

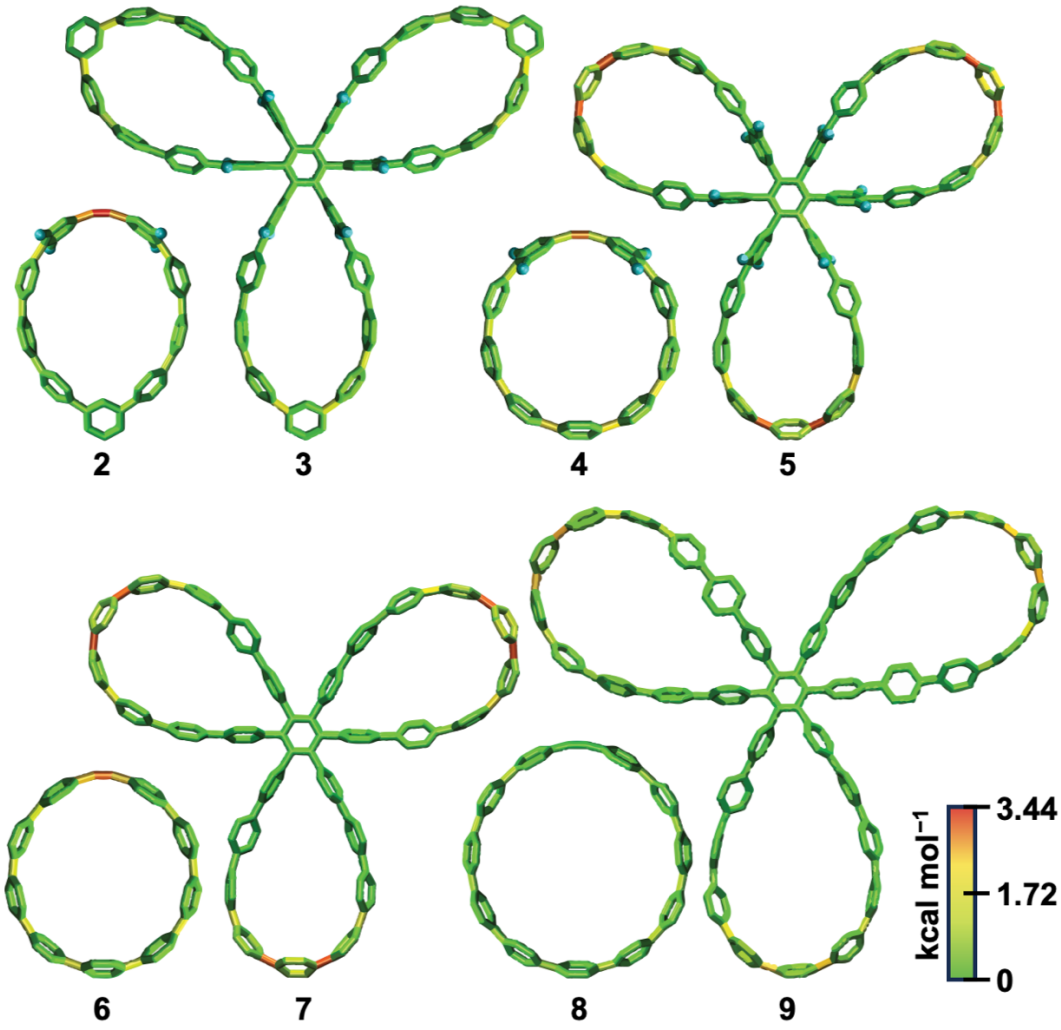

Figure 4.4. StrainViz structures for each trimer and its respective [*n*+1]CPP (**2** was not isolated but is shown here for completeness).

4.2.4 Photophysical Analysis

Photophysical data for each trimer and its associated parent [*n*+1]CPP[31,32] (where applicable) are displayed in **Figure 4.5** and **Table 4.3**. Absorbance and emission traces as well as

quantum yields were collected for all molecules in comparatively nonpolar dichloromethane

Table 4.3. Tabulated photophysical data for trimers and associated [*n*+1]CPPs.

compound	$\lambda_{max,abs}$ (nm)		$\lambda_{max,em}$ (nm)		extinction coefficient, ε ($\times 10^5$ M^{-1} cm^{-1})	quantum yield, Φ	
	DCM	DMSO	DCM	DMSO	DCM	DCM	DMSO
3	315	318	402	415	3.27 ± 0.04	0.88	0.88
4	335	343	463	507	1.02 ± 0.04	0.49	0.07
5	330	337	472	479	3.13 ± 0.23	0.40	0.46
6	342	351	463	473	1.55	0.76	0.67
7	337	-	472	487	4.52 ± 0.07	0.42	0.47
8	341	350	449	460	1.63	0.80	0.83
9	338	-	454	468	4.93 ± 0.20	0.69	0.67

* values for **6** and **8** were measured previously[24,25] and included here as a point of reference. Note that quantum yields were measured by slightly different methods than were used in this study (see SI and previous publications for details).

(DCM) and polar dimethyl sulfoxide (DMSO) to probe any solvent-dependent effects; extinction

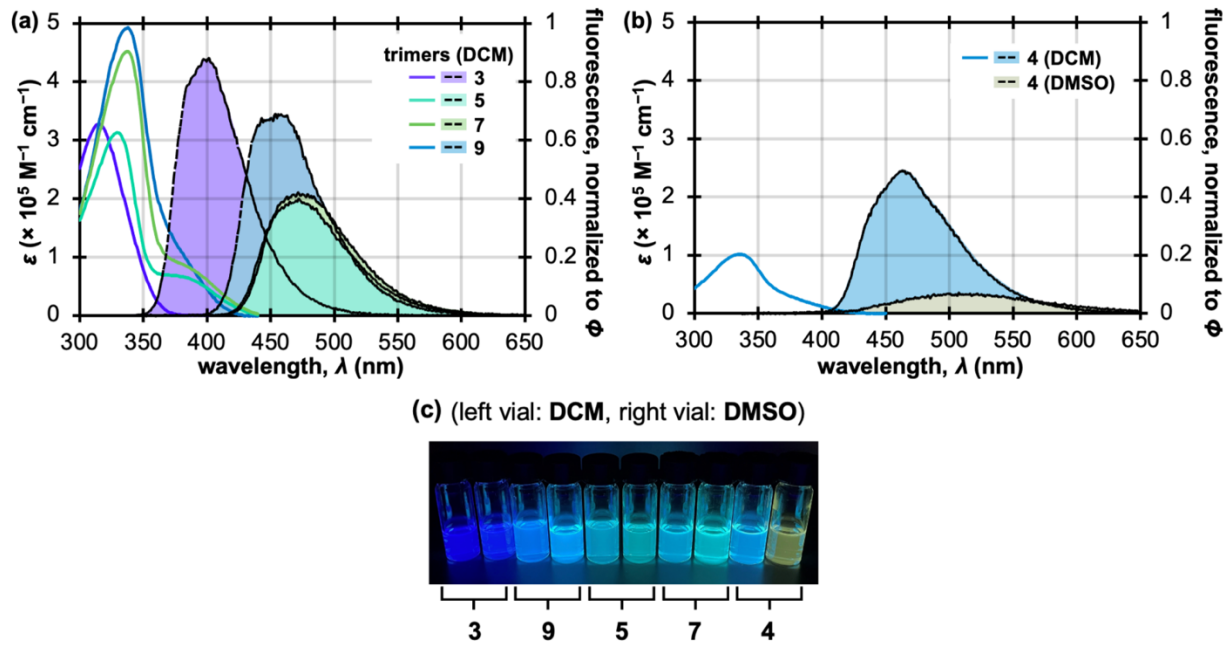

Figure 4.5. Photophysical characterization for the new molecules described herein. (a) Extinction coefficients (colored lines) and fluorescence emission traces (black lines) for each trimer in DCM plotted as a function of wavelength. Fluorescence traces are scaled such that the maximum *y*-value of each curve matches the quantum yield of the compound in DCM. (b) Extinction coefficient for

4 (blue line) as a function of wavelength in DCM plotted along with fluorescence emission traces (black lines) for **4** in DCM and DMSO (emission curves are also scaled to quantum yield in the respective solvent). (c) Solutions of trimers and **4** in DCM and DMSO under irradiation with long-wave UV light.

coefficients were collected in DCM. For all but one of the trimers, we did not observe a large solvent effect on photophysics beyond a slight red-shifting in maximum absorbance wavelength ($\lambda_{max,abs}$) and maximum emission wavelength ($\lambda_{max,em}$) values in DMSO (**Table 4.3** and **Figure 4.5c**). Therefore, we focused our analysis of trimer photophysics on the measured values in DCM. The only notable solvent effects were observed for **fluor[9+1]CPP**, which displayed highly solvent-dependent fluorescence properties (*vide infra*).

Carbon nanohoops typically display a $\lambda_{max,abs}$ around 340 nm. This major absorbance band is dominated by degenerate HOMO−-2/HOMO−-1 to LUMO and HOMO to LUMO+1/LUMO+2 transitions, as the HOMO to LUMO transition is symmetry forbidden in most cases.[15,49]

When comparing the absorbance profiles of each trimer to its parent [*n*+1]CPP, we can observe a slight hypsochromic shift of $\lambda_{max,abs}$ upon trimerization. For example, **6** has a measured $\lambda_{max,abs}$ of 342 nm in DCM, while **7** has a slightly blue-shifted $\lambda_{max,abs}$ of 337 nm. Nonetheless, **5**, **7**, and **9** all maintain $\lambda_{max,abs}$ values around the typical 340 nm. Computational results for **5** (SI Table S9) indicate that the HOMO-LUMO transition is weak, and the stronger absorption is a combination of higher energy transitions (e.g. HOMO to LUMO +3, HOMO to LUMO +4, etc.). Comparing the trimers, we note that **5** has a slightly blue-shifted $\lambda_{max,abs}$ compared to **7**. We have previously observed a slight hypsochromic shift in fluorinated *para*-linked nanohoops compared to their hydrocarbon counterparts.[32,50,51] Finally, the shortest wavelength $\lambda_{max,abs}$ is displayed by **3**; we hypothesize that the significant lack of strain in this molecule in comparison to the other trimers elevates the energy of this transition.[52]

The extinction coefficient for each trimer is plotted as a function of wavelength in **Figure 4.5a**; extinction coefficients for each trimer (and corresponding [*n*+1]CPP) at $\lambda_{max,abs}$ are displayed in **Table 4.3**. In each case where it is possible to compare the trimer to its [*n*+1]CPP parent, we observe that the extinction coefficient at $\lambda_{max,abs}$ is (within error) approximately three times that of the parent. For instance, we previously measured an extinction coefficient for **6** of 1.55×10^5 M^{-1} cm^{-1} in DCM at $\lambda_{max,abs}$.[31] This value essentially triples for **7** with a measured extinction coefficient of 4.52×10^5 M^{-1} cm^{-1}. This is an intriguing result which suggests that the molar absorptivity of each [*n*+1]CPP macrocycle is maintained even upon its incorporation into the trimeric species, establishing the [*n*+1] trimers as exceptionally bright chromophores.

The fluorescence emission traces for each trimer are plotted in **Figure 4.5a** as a function of wavelength and normalized such that the maximum *y*-axis value matches the molecule's measured quantum yield in DCM. We observe that **9**, **5**, and **7** display fluorescence emissions that are slightly red-shifted in comparison to their parent [*n*+1]CPPs; for example, the maximum emission wavelength ($\lambda_{max,em}$) for **6** in DCM was previously measured to be 463 nm,[31] while **7** displays a $\lambda_{max,em}$ of 472 nm. As is generally observed in carbon nanohoops,[15] the smaller **7** and **5** have a red-shifted emission in comparison to the larger **9**, probably due to increased conjugation between phenylenes in smaller sizes. We observe that fluorination of scaffold of **7** does not seem to significantly affect fluorescence properties. The hypsochromic fluorescence emission of **3** in comparison to the other trimers in this study can most likely be attributed to a lack of strain in the molecule which in turn decreases p-orbital overlap and widens the HOMO-LUMO gap.[15,52] Quantum yields for all trimers were reasonably high: **5** and **7** displayed quantum yields of 0.40 and 0.42 in DCM, respectively, while the larger **9** displayed a slightly higher quantum yield of 0.69. **3** exhibited the highest quantum yield in the series at 0.88.

Figure 4.5b and 4.**5c** highlight the significant solvent-dependent fluorescence properties of **4**. The $\lambda_{max,em}$ for **4** shifts from 463 nm in DCM to 507 nm in DMSO. This bathochromic shift in $\lambda_{max,em}$ with increasing solvent polarity is accompanied by a notable drop in quantum yield from 0.49 in DCM to 0.07 in DMSO. These results suggest that **4** is a donor-acceptor-type nanohoop that, upon excitation, experiences charge transfer from the electron-rich curved phenylene backbone of the nanohoop to the electron-poor, fluorinated, alkyne-containing region.[13,16,17,32,53–56] (See SI Figure S39 for further details). We speculate that a polarized excited state would be better stabilized in polar solvents such as DMSO, therefore resulting in a lower energy transition back to the ground state and longer wavelength $\lambda_{max,em}$.[57] The lower quantum yield would in turn be explained by the energy gap law, as has been seen previously for donor-acceptor molecules.[58] The fact that the quantum yield in DMSO is largely restored upon trimerization to **5** suggests that the trimer's excited state is significantly less polarized.[57,58] This finding is consistent with our calculations (see SI Figure S33).

4.3 Conclusion

Employing suitable late-stage transformations of curved aromatic hydrocarbons is a promising approach for systematically diversifying their structures, and in turn, their applications. The realization of unique molecular architectures is a major driving force for uncovering and characterizing the rich structure function relationships that render organic synthesis a tool for advancing carbon nanoscience. Our previous studies of strained alkyne-containing carbon nanohoops focused on efficiently attaching them *via* click chemistry methods to other small molecules of interest.[31–33] In this work, we have described a synthetically simple and high yielding method for expanding these molecules into larger carbon nanostructures by a metal-catalyzed trimerization reaction. The result is high molecular weight pinwheel-shaped [*n*+1] trimers with

exceptionally high luminescence and generally good solubility. We envision that this method can provide access to trimer derivatives with unique photophysics, structure, and functionality, especially given the modularity of [*n*+1]CPP syntheses. For example, the inclusion of donor and acceptor groups to tune optoelectronic properties, functional handles as sites for further reactivity, and heteroatoms to tune supramolecular capabilities are all accessible and exciting next steps for these trimeric macrocycles. The current work also provides further evidence that strained alkyne nanohoops are amenable to derivatization through a variety of metal-mediated reactions; classical work of Reppe et al. suggests that the use of an appropriate transition metal catalyst may afford tetrameric species with four CPPs linked around a newly formed cyclooctatetraene.[34] The use of strain promoted reactions to generate well-defined carbon nanomaterials is an exciting area of research lying at the interface of organic synthesis and nanoscience that we will continue to explore.

4.4 Experimental Section

4.4.1 General Experimental Details

Unless otherwise noted, commercially available materials were used without purification. Compounds S1, S2, S5, [9+1]CPP, [11+1]CPP, and Pd SPhos G3 were prepared according to the literature. Moisture and oxygen sensitive reactions were carried out in flame-dried glassware and under an inert atmosphere of purified nitrogen using syringe/septa technique. Tetrahydrofuran (THF), dimethylformamide (DMF), and 1,4-dioxane were dried by filtration through alumina according to the methods described by Grubbs.[60] Thin-layer chromatography (TLC) was performed on aluminium plates coated with 0.20 mm thickness of Silica Gel 60 F254 (Macherey-Nagel). Developing plates were visualized using UV light at wavelengths of 254 and 365 nm. Silica column chromatography was conducted with Zeochem Zeoprep n60 Eco 40-63 μm silica

gel. Alumina column chromatography was conducted with SorbTech basic alumina (pH 10), Act. II-III, 50-200 μm. ^{1}H and ^{13}C NMR spectra were recorded on either a Bruker Avance III HD 500 (^{1}H: 500 MHz, ^{13}C: 126 MHz) or Bruker Avance III HD 600 MHz (^{1}H: 600 MHz, ^{13}C: 151 MHz) NMR spectrometer. The samples were measured at 25 °C. The chemical shifts (δ) were reported in parts per million (ppm) and were referenced to the residual protio-solvent (CD_2Cl_2, ^{1}H: δ = 5.32 ppm and ^{13}C: δ = 53.84 ppm; deuterated 1,1,2,2-tetrachloroethane (TCE-d_2), ^{1}H: δ = 6.00 ppm and 13C: δ = 73.78 ppm) or to tetramethylsilane (for $CDCl_3$, TMS, δ = 0.00 ppm). Coupling constants (J) are given in Hz and the apparent resonance multiplicity is reported as s (singlet), d (doublet), t (triplet), q (quartet), dd (doublet of doublets) or m (multiplet). Infrared absorption (IR) spectra were recorded on a Thermo Scientific Nicolet 6700 spectrometer equipped with a diamond crystal Smart ATR. Characteristic IR absorptions are reported in cm^{-1} and denoted as strong (s), medium (m), and weak (w). UV/Vis absorption and fluorescence spectra were recorded on an Agilant Cary 100 spectrophotometer and a Horiba Jobin Yvon Fluoromax-4 Fluorimeter, respectively. All measurements were carried out under ambient conditions in a Spectrocell RF-1010-T threaded top vacuum formed borosilicate fluorometer cell (10 mm light path).

4.4.2 Synthesis

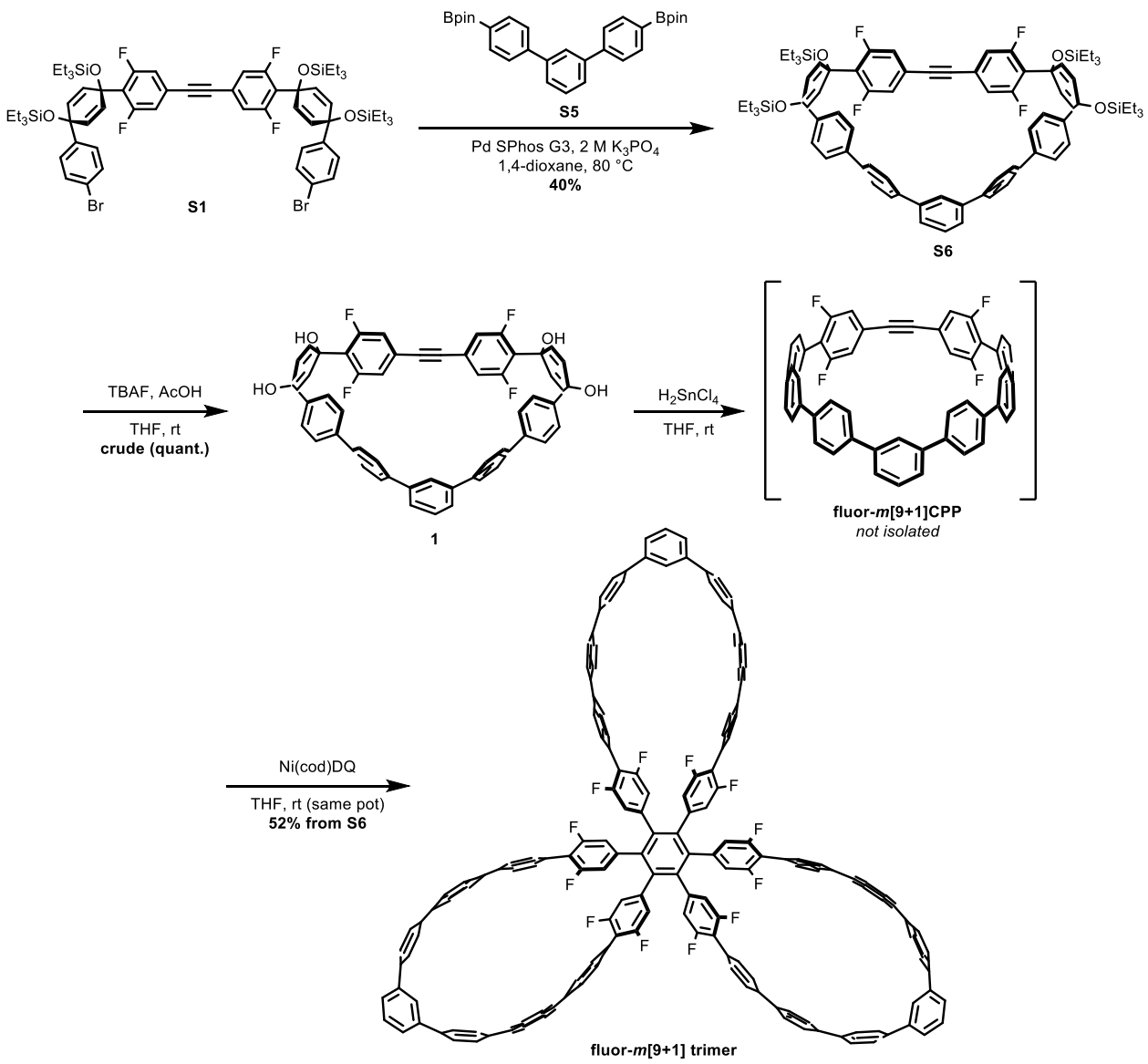

Scheme S2. Overview of the synthesis of **fluor-*m*[9+1] trimer**.

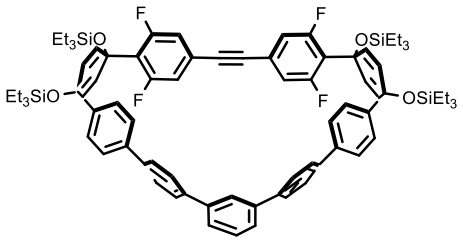

Compound S6. **S5** (0.146 g, 0.302 mmol, 1.1 equiv.), **S1** (0.340 g, 0.275 mmol, 1 equiv.), and Pd SPhos G3 (0.022 g, 0.028 mmol, 0.1 equiv.) were dissolved in 1,4-dioxane (336 mL, 0.0009 M, sparged with N_2 for one hour prior to use). The resulting solution was sparged with N_2 for an additional 15 minutes. The reaction mixture was heated to 80 °C over the course of 15 minutes. Deoxygenated aqueous K_3PO_4 solution (34 mL, 2.0 M, sparged with N_2 for one hour prior to use) was added via syringe. The reaction mixture was allowed to stir at 80 °C for two hours. It was then cooled to room temperature and the aqueous layer was removed. The dioxane was removed via rotary evaporator. The resultant oily solid was dissolved in DCM, washed with brine, dried over sodium sulfate, filtered and concentrated to yield the crude product as an orange solid. The crude product was purified via automated column chromatography (0 – 30% DCM/hexanes), then sonicated in methanol to yield the final product as a white solid (0.143 g, 0.11 mmol, 40%). R_f = 0.42 (SiO_2, 35% DCM/hexanes); ^{1}H NMR (500 MHz, Methylene Chloride-d_2) δ 7.64 – 7.60 (m, 2H), 7.59 – 7.50 (m, 9H), 7.39 (d, J = 8.5 Hz, 4H), 7.32 (d, J = 8.5 Hz, 4H), 7.17 (t, J = 1.9 Hz, 1H), 6.98 (d, J = 9.9 Hz, 4H), 6.43 (dt, J = 10.3, 3.4 Hz, 4H), 6.04 (d, J = 10.2 Hz, 4H), 1.02 (t, J = 7.9 Hz, 18H), 0.91 (t, J = 7.9 Hz, 18H), 0.72 (q, J = 7.9 Hz, 12H), 0.59 (q, J = 8.0 Hz, 12H). ^{13}C NMR (126 MHz, Methylene Chloride-d_2) δ 161.90 (d, J = 9.3 Hz), 159.89 (d, J = 9.3 Hz), 144.96, 142.42, 141.50, 140.37, 139.89, 133.88, 133.47, 129.88 (t, J = 3.2 Hz), 129.50, 128.57, 127.70, 127.34, 126.11, 124.36, 124.07 (t, J = 13.3 Hz), 123.52 (t, J = 14.0 Hz), 116.33 (dd, J = 21.0, 7.2 Hz), 89.01 (t, J = 3.5 Hz), 72.18, 70.26 (t, J = 2.7 Hz), 7.25, 6.95, 6.80, 6.54. ^{19}F NMR (471 MHz,

Methylene Chloride-d_2) δ -105.02 (d, J = 10.3 Hz); IR (ATR) ṽ 2952 (m), 2909 (m), 2874 (m), 1619 (m), 1549 (m), 1477 (w), 1457 (w), 1069 (s), 1014 (s), 955 (s), 853 (m), 823 (m), 792 (m), 720 (s); HRMS (ASAP, positive mode) m/z calcd for $C_{80}H_{93}O_4F_4Si_4$: 1305.6087 $[M+H]^+$, found 1305.6215.

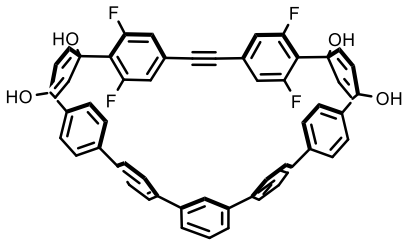

Compound 1. S6 (0.140 g, 0.011 mmol, 1 equiv.) was dissolved in THF (13.4 mL, 0.008 M) at room temperature. Acetic acid (0.31 mL, 5.36 mmol, 50 equiv.) was added dropwise, closely followed by dropwise addition of tetra-*n*-butylammonium fluoride (1 M solution in THF, 2.68 mL, 2.68 mmol, 25 equiv.). The reaction mixture was allowed to stir for 18 hours at room temperature. Deionized water (10 mL) was added. The organic layer was almost completely removed *via* rotary evaporator, and the resultant white suspension was vigorously sonicated. The now-deprotected intermediate S**7** (a white solid) was isolated *via* vacuum filtration and thorough washing with DI water and dichloromethane (assumed quantitative yield, 0.091 g, 0.11 mmol).

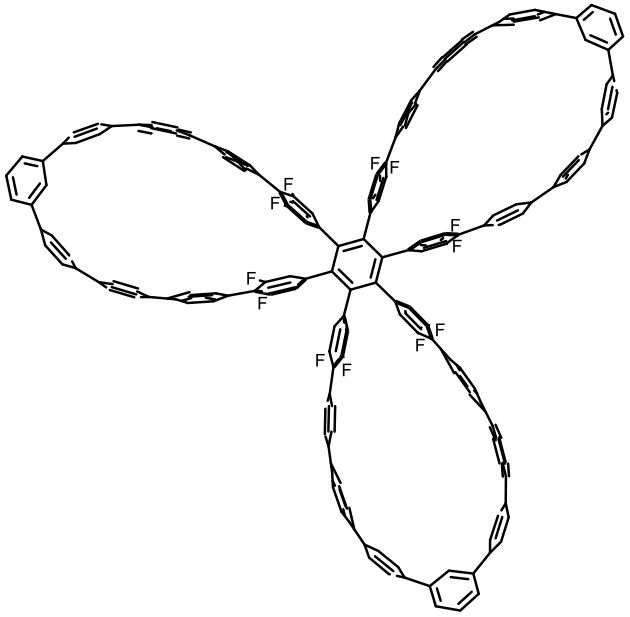

fluor-*m*[9+1]CPP trimer. *One-pot reductive aromatization and trimerization from **1***. $SnCl_2 \cdot 2H_2O$ (0.181 g, 0.8 mmol, 1.0 equiv. with respect to HCl) was dissolved in tetrahydrofuran (20 mL, 0.040 M). HCl (0.13 mL, 1.6 mmol, 2.0 equiv. with respect to $SnCl_2 \cdot 2H_2O$) was added and the reaction was allowed to stir for 20 minutes. Concurrently in a separate flask, the deprotected macrocycle (0.091 g, 0.11 mmol, 1 equiv.) was dissolved in THF (10 mL, 0.011 M). After the 20 minutes had elapsed, prepared H_2SnCl_4 solution (5.9 mL, 0.24 mmol, 2.2 equiv.) was added to the solution of deprotected macrocycle **1**. The reaction was allowed to stir for 40 minutes. Concurrently, Ni(cod)DQ (0.053 g, 0.16 mmol, 1.5 equiv.) was dissolved in THF (8 mL, 0.02 M). After the 40 minutes had elapsed, the Ni(cod)DQ solution was transferred to the reaction flask and the reaction was allowed to stir for an additional 40 minutes. The reaction was quenched with a saturated aqueous solution of sodium bicarbonate (20 mL). THF was removed via rotary evaporator and the organic products were extracted with DCM (5 X 30 mL), washed with brine (1 X 30 mL), dried over sodium sulfate, filtered, and concentrated to yield the crude product as a yellow solid. Purification via column chromatography (basic AlOx, 50–100% DCM/hexanes) yielded the final

product as a white solid (0.044 g, 0.056 mmol, 52%). R_f = 0.61 (60% DCM/hexanes). ^{1}H NMR (500 MHz, Methylene Chloride-d_2) δ 7.62 – 7.50 (m, 57H), 7.41 – 7.35 (m, 24H), 6.74 (d, J = 7.9 Hz, 12H), 6.13 (t, J = 1.9 Hz, 3H). ^{13}C NMR (126 MHz, Methylene Chloride-d_2) δ 159.73 (dd, J = 249.8, 8.1 Hz), 143.12, 142.68, 140.78, 140.28 (t, J = 10.4 Hz), 139.93, 139.69, 139.45, 139.16, 138.95, 131.15 (d, J = 2.4 Hz), 129.69, 129.61, 127.84, 127.70, 127.61, 127.29, 127.10, 123.19, 116.95 (t, J = 18.0 Hz), 114.86 (d, J = 27.7 Hz). ^{19}F NMR (471 MHz, Methylene Chloride-d_2) δ -115.04 (d, J = 8.1 Hz). IR (ATR) ṽ 3023 (w), 2974 (w), 2853 (w), 1629 (w), 1574 (w), 1563 (w), 1550 (w), 1483 (m), 1390 (s), 1290 (m), 1197 (m), 1111 (m), 1021 (s), 1003 (s), 806 (s), 756 (s); HRMS (ESI, positive mode) m/z calcd for $C_{168}H_{96}F_{12}$: 2340.7315 $[M]^+$, found 2340.7425.

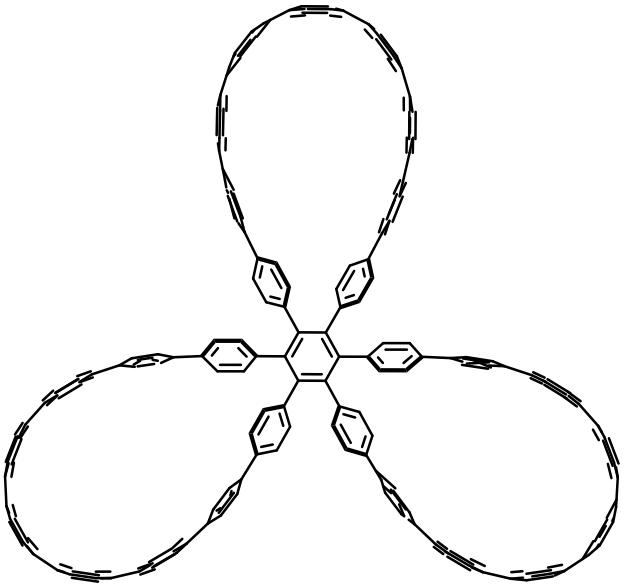

[9+1] trimer. [9+1]CPP (0.0097 g, 0.014 mmol, 1 equiv.) and $Pd_2(dba)_3$ (0.0013 g, 0.0014 mmol, 0.1 equiv.) were dissolved in DCM (5 mL, 0.003 M). The red mixture was allowed to stir at room temperature for 1 hour. The crude mixture was directly purified *via* column chromatography (basic AlO_x, 0-100% DCM/hexanes). Product containing fractions were combined and solvent was removed via rotary evaporation. This afforded the product as a yellow solid (0.0093 g, 0.0045

mmol, 95%). ^{1}H NMR (500 MHz, Methylene Chloride-d_2) δ 7.60 – 7.42 (m, 84H), 7.20 (d, J = 8.6 Hz, 12H), 6.99 (d, J = 8.4 Hz, 12H). ^{13}C NMR (126 MHz, CD_2Cl_2) δ 140.42, 139.90, 138.67, 138.57, 138.48, 138.19, 137.95, 137.57, 137.46, 136.50, 131.94, 127.65, 127.56, 127.44, 127.28, 126.88, 126.76, 126.56, 124.70. IR (ATR) ṽ 3025.83 (w), 2915.53 (w), 1586.95 (w), 1484.43 (m), 1388.95 (w), 1259.26 (w), 1000.30 (m), 809.16 (s), 729.98 (m). HRMS (MALDI) m/z: [M]+ calculated for $C_{168}H_{108}$, 2124.8451; found, 2124.8375.

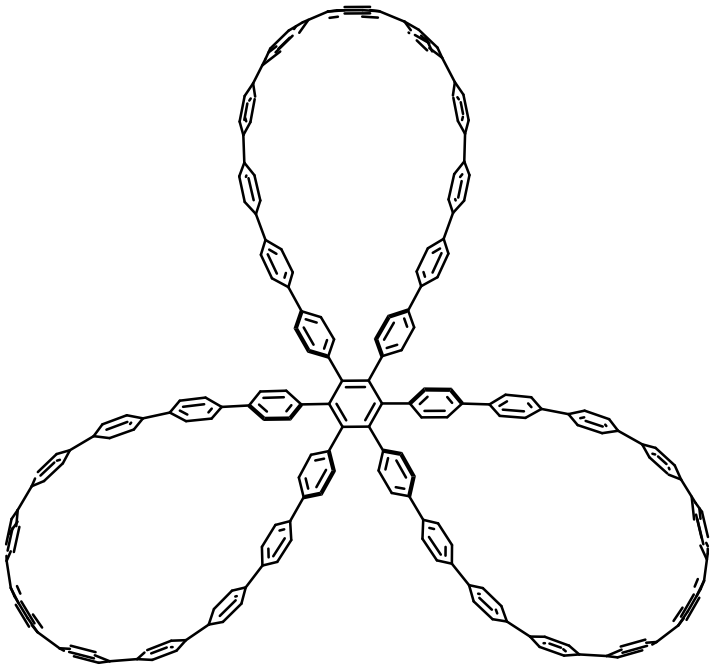

[11+1] trimer. [11+1]CPP (0.005 g, 0.0058 mmol, 1 equiv.) and $Pd_2(dba)_3$ (0.0021 g, 0.0023 mmol, 0.4 equiv.) were dissolved in DCM (2 mL, 0.003 M). The resultant red mixture was allowed to stir at room temperature for 1 hour. The crude mixture was directly purified *via* column chromatography (basic AlO_x, 0-100% DCM/hexanes). Product containing fractions were combined and solvent was removed via rotary evaporation. This afforded the product as a slightly yellow/white solid (0.0031 g, 0.0019 mmol, 63%). ^{1}H NMRs were taken in both CD_2Cl_2 and TCE-d_2 due to low solubility in CD_2Cl_2. ^{13}C NMR was taken in TCE-d_2 to heighten solubility and maximize signal, but signal-to-noise ratio is still low. ^{1}H NMR (500 MHz, TCE-d_2) δ 7.67 – 7.46

(m, 108H), 7.24 (d, J = 7.6 Hz, 12H), 7.00 (d, J = 8.0 Hz, 12H). ^{1}H NMR (500 MHz, CD_2Cl_2) δ 7.62 – 7.57 (m, 84H), 7.51 (s, 24H), 7.26 (d, J = 8.6 Hz, 12H), 7.05 (d, J = 8.6 Hz, 12H)—solubility was too low in this solvent to derive accurate peak integrations. ^{13}C NMR (126 MHz, TCE-d_2) δ 140.00, 139.86, 139.01, 138.79, 138.62, 138.27, 137.81, 137.68, 137.59, 135.91, 131.83, 127.52, 127.29, 127.11, 126.89, 126.70, 124.77 (6 signals unaccounted for). IR (ATR) ṽ 3022.86 (w), 1590.41 (w), 1482.53 (m), 1386.40 (w), 1062.69 (br), 1001.94 (m), 806.94 (s), 734.75 (m). HRMS (MALDI) m/z: $[M]^+$ calculated for $C_{204}H_{132}$, 2581.0329; found, 2581.0409.

4.4.3 Metal screening for cyclotrimerization with fluor[9+1]CPP

Fluor[9+1]CPP (0.0015 g, 0.0019 mmol) was added to four separate vials (containing new stir bars) and placed under inert atmosphere (N_2). Concurrently, air-free solutions of each metal tested were made with N_2-sparged deuterated chloroform ($CDCl_3$) as described in the table below:

Table S1. Stock solution makeup for metal screening experiment.

metal	mass (g)	volume $CDCl_3$ (mL)	[metal] in solution (mM)
$Pd_2(dba)_3$	0.0036	10	0.39
$RhCl(PPh_3)_3$	0.0036	10	0.39
Ni(cod)DQ	0.0026	20	0.39

Then, 1 mL of each stock solution was added to its respective vial. A final 1 mL of deuterated chloroform was added to the fourth vial to serve as a metal-free control. Each non-control vial therefore contained 1.9 mM **fluor[9+1]CPP** and 0.39 mM of metal catalyst (20% catalyst loading). Each reaction vial was allowed to stir for one hour at room temperature under inert atmosphere, at which point the solution was transferred to an NMR tube and a quantitative ^{19}F NMR of the

mixture was taken (8 scans, d1 relaxation time of 120 s). The NMR spectra were manually phased and baseline corrected at the peaks of interest. Integration values for starting material (**fluor[9+1]CPP**) and product (**fluor[9+1] trimer**) peaks are shown in the table below. Percent conversions are also calculated.

Table S2. Integrations of starting material and product peaks from quantitative ^{19}F NMR.

trial	**fluor[9+1]CPP** integration (–113.13 to –113.27 ppm)	**fluor[9+1] trimer** integration (–113.86 to –113.98 ppm)	calc. % conversion
control	819.243	3.84015	0.5
$Pd_2(dba)_3$	0.108673	391.49	100
$RhCl(PPh_3)_3$	462.268	31.3141	6.3
Ni(cod)DQ	343.44	44.6885	11.5

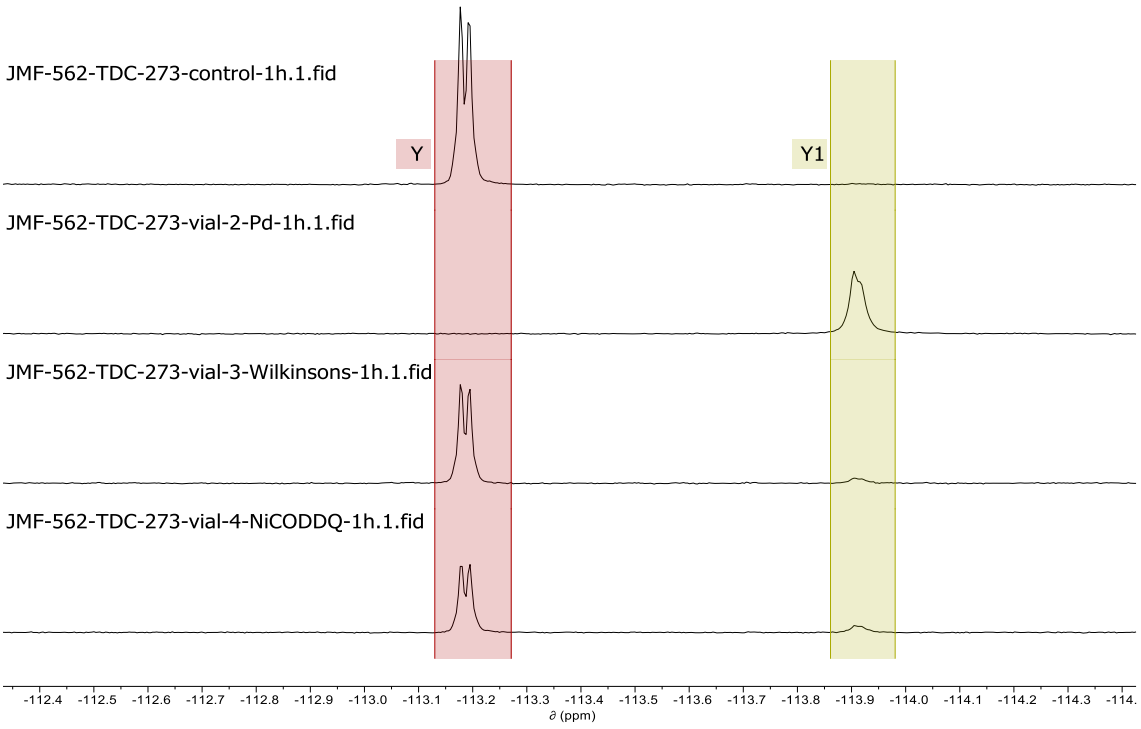

Figure S20. Stacked spectra of starting material (**fluor[9+1]CPP**) and product (**fluor[9+1] trimer**) peaks in quantitative ^{19}F NMR for each metal tested.

4.4.4. Treatment of diphenylacetylene with $Pd_2(dba)_3$

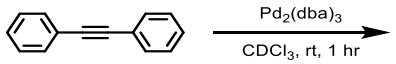

The purpose of this experiment was to assess the reactivity of diphenylacetylene towards a Pd(0) catalyst. Diphenylacetylene (0.0034 g, 0.019 mmol, 1 equiv.) was added to two vials. To the second vial was also added $Pd_2(dba)_3$ (0.0036 g, 0.0039 mmol, 0.2 equiv.) Under inert atmosphere (N_2), the solids in each vial were dissolved in $CDCl_3$ (10 mL, sparged with N_2 prior to use). The solutions were allowed to stir for one hour at room temperature under inert atmosphere. ^1H NMR (**Figure S21**) was collected after one hour.

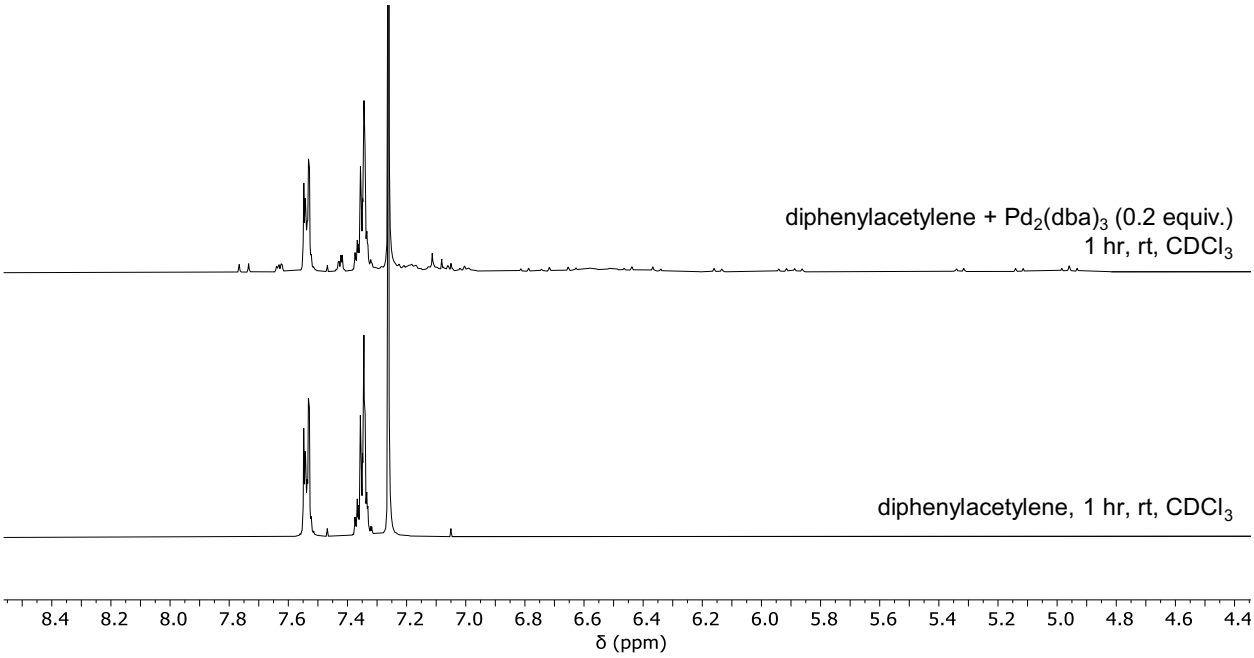

Figure S21. Comparison of ^{1}H NMR spectra of diphenylacetylene with (top) and without (bottom) subjection to Pd_2dba_3 (0.2 equiv.) in $CDCl_3$.

We found that the diphenylacetylene appeared unreacted even after stirring with $Pd_2(dba)_3$ for one hour. We also found no evidence of precipitate forming in either solution. To ensure that the minor peaks in the top spectrum of **Figure S21** could be assigned back to the $Pd_2(dba)_3$ catalyst, we stacked this spectrum with a spectrum of $Pd_2(dba)_3$ alone in $CDCl_3$ (**Figure S22**).

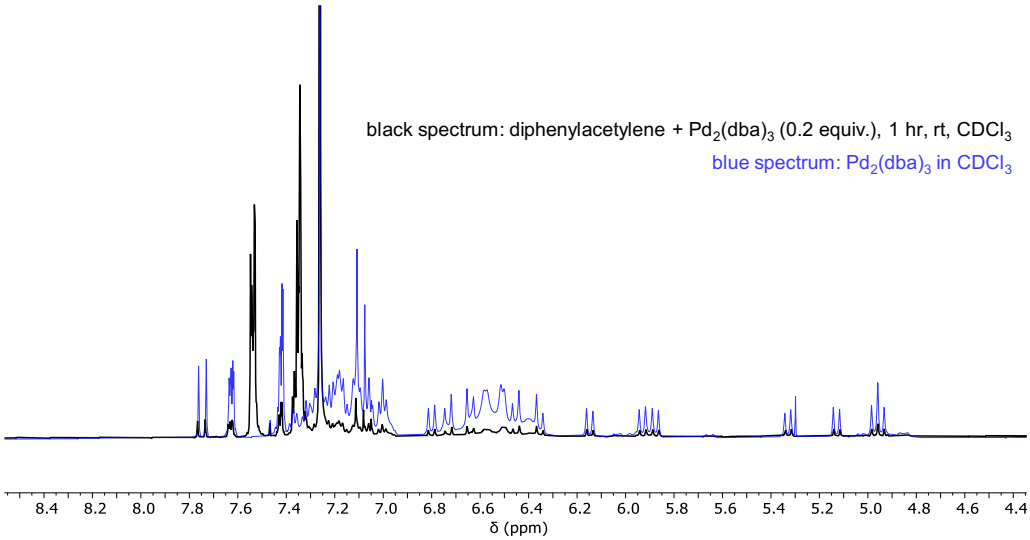

Figure S22. Overlay of top spectrum of **Figure S21** (black) with $Pd_2(dba)_3$ in $CDCl_3$ (blue).

4.4.5. Photophysical characterization

For extinction coefficient measurements, the compound of interest was first dissolved at known concentration using volumetric glassware. This solution was then added incrementally to a cuvette containing a known amount of solvent and absorbance measurements were taken after each addition The whole process was repeated three times. Data was worked up by dividing the absorbance value at each wavelength by the solution's concentration. Measurements from each trial were averaged together, and the table inset for each figure below shows the measured extinction coefficient at the $\lambda_{max,abs}$ for each trial.

$\lambda_{max,abs}$ = 335 nm

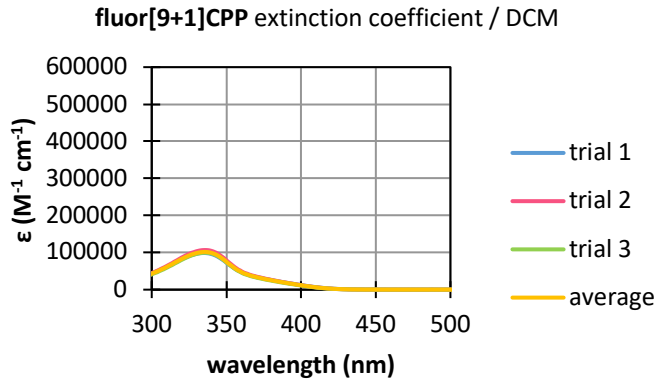

trial	ε (M^{-1} cm^{-1})
1	9.89×10^4
2	1.07×10^5
3	9.95×10^4
avg.	1.02×10^5
std. dev.	0.04×10^5

Figure S23. Extinction coefficient plot for **fluor[9+1]CPP** in DCM.

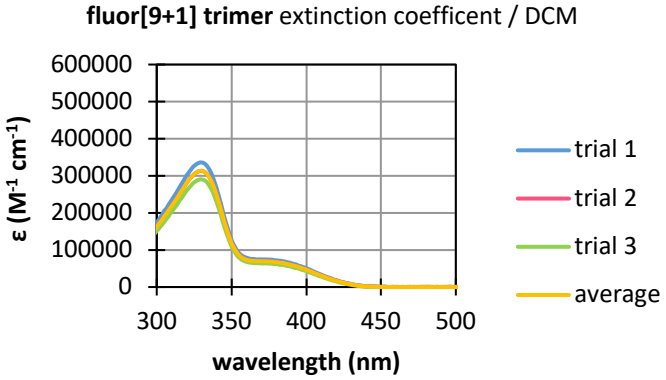

$\lambda_{max,abs}$ = 330 nm	
trial	**ε (M^{-1} cm^{-1})**
1	3.36×10^5
2	3.13×10^5
3	2.90×10^5
avg.	3.13×10^5
std. dev.	0.23×10^5

Figure S24. Extinction coefficient plot for **fluor[9+1] trimer** in DCM.

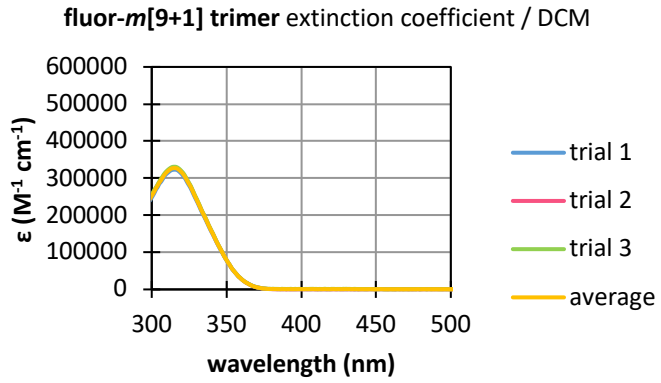

$\lambda_{max,abs}$ = 315 nm	
trial	**ε (M^{-1} cm^{-1})**
1	3.23×10^5
2	3.28×10^5
3	3.31×10^5
avg.	3.27×10^5
std. dev.	0.04×10^5

Figure S25. Extinction coefficient plot for **fluor-*m*[9+1] trimer** in DCM.

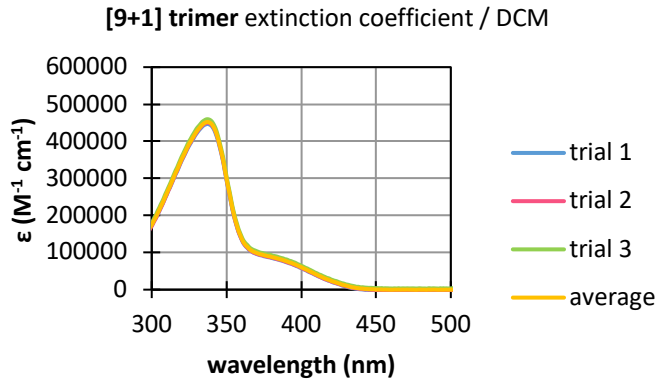

Figure S26. Extinction coefficient plot for **[9+1] trimer** in DCM.

$\lambda_{max,abs}$ = 337 nm	
trial	**ε (M^{-1} cm^{-1})**
1	4.47 x 10^5
2	4.50 x 10^5
3	4.60 x 10^5
avg.	4.52 x 10^5
std. dev.	0.07 x 10^5

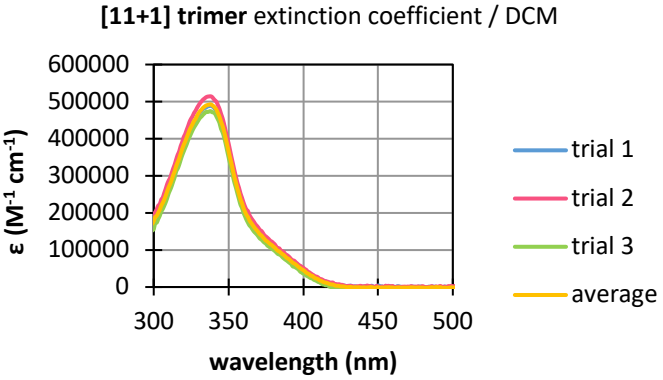

Figure S27. Extinction coefficient plot for **[11+1] trimer** in DCM.

$\lambda_{max,abs}$ = 338 nm	
trial	**ε (M^{-1} cm^{-1})**
1	4.89 x 10^5
2	5.14 x 10^5
3	4.75 x 10^5
avg.	4.93 x 10^5
std. dev.	0.20 x 10^5

Quantum yield measurements were performed using the method described in "A Guide to Recording Fluorescence Quantum Yields" by Horiba Scientific.[61] The internal standards used were quinine sulfate (0.1 M H_2SO_4, aqueous, lit. value Φ = 0.54, fluorescence signal integrated from 400-600 nm) and anthracene (ethanol, lit. value Φ = 0.27, fluorescence signal integrated from 360-480 nm). For fluorescence measurements, all compounds were excited at a wavelength of 330 nm with consistent excitation and emission slit widths of 1 nm. Absorbance values plotted below were as measured at 330 nm. Fluorescence signal integrations for compounds of interest are listed

below:

Table S3: Compound integration ranges in DMSO and DCM.

compound of interest	integration range (DCM, nm)	integration range (DMSO, nm)
fluor[9+1]CPP	400 – 600	400 – 600
fluor[9+1] trimer	400 – 600	400 – 600
fluor-m[9+1] trimer	345 – 550	345 – 600
[9+1] trimer	400-600	400-600
[11+1] trimer	400-600	400-600

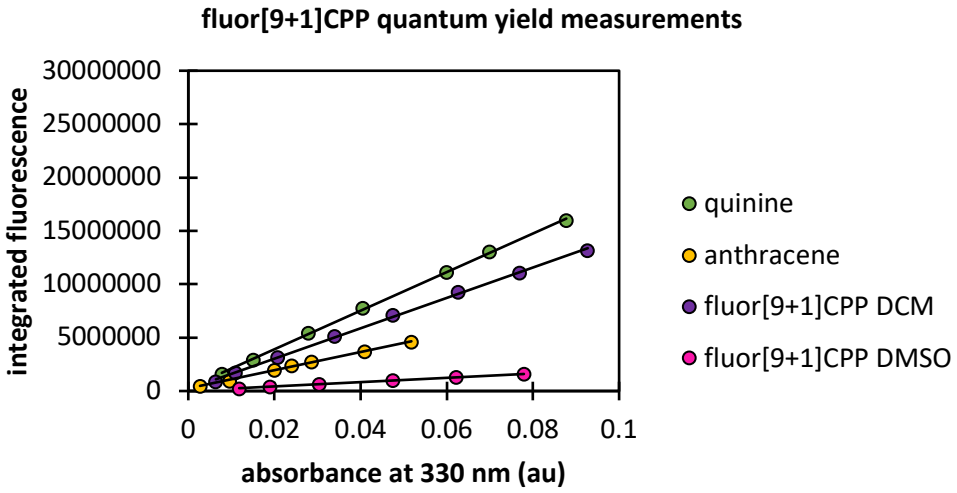

Figure S28. Quantum yield plot for **fluor[9+1]CPP**.

Table S4: Quantum yield data for **fluor[9+1]CPP**.

compound	solvent	slope	Φ w.r.t. quinine	Φ w.r.t. anthracene	avg. Φ	std. dev.
quinine	0.1 M H_2SO_4	1.81 x	0.54 (lit)	0.55	0.54	0.007

	(*aq*)	10^8				
anthracene	ethanol	8.51 x 10^7	0.26	0.27 (lit)	0.27	0.003
fluor[9+1]CPP	DCM	1.42 x 10^8	0.49	0.49	0.49	0.006
fluor[9+1]CPP	DMSO	2.01 x 10^7	0.07	0.08	0.07	0.001

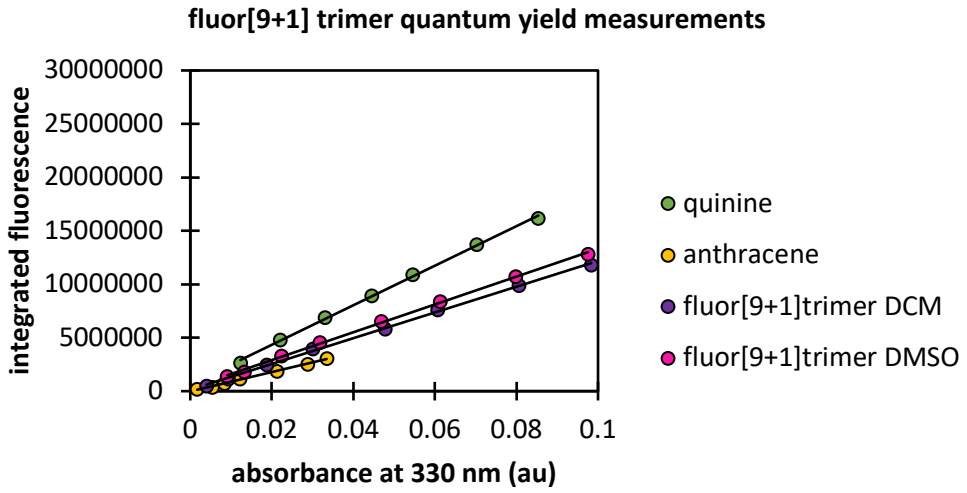

Figure S29. Quantum yield plot for **fluor[9+1] trimer**.

Table S5: Quantum yield data for **fluor[9+1] trimer**.

compound	**solvent**	**slope**	**Φ w.r.t. quinine**	**Φ w.r.t. anthracene**	**avg. Φ**	**std. dev.**
quinine	0.1 M H_2SO_4 (*aq*)	1.85 x 10^8	0.54 (lit)	0.53	0.53	0.004

anthracene	ethanol	9.05 x 10^7	0.28	0.27 (lit)	0.27	0.002
fluor[9+1] trimer	DCM	1.20 x 10^8	0.40	0.39	0.40	0.003
fluor[9+1] trimer	DMSO	1.30 x 10^8	0.47	0.46	0.46	0.003

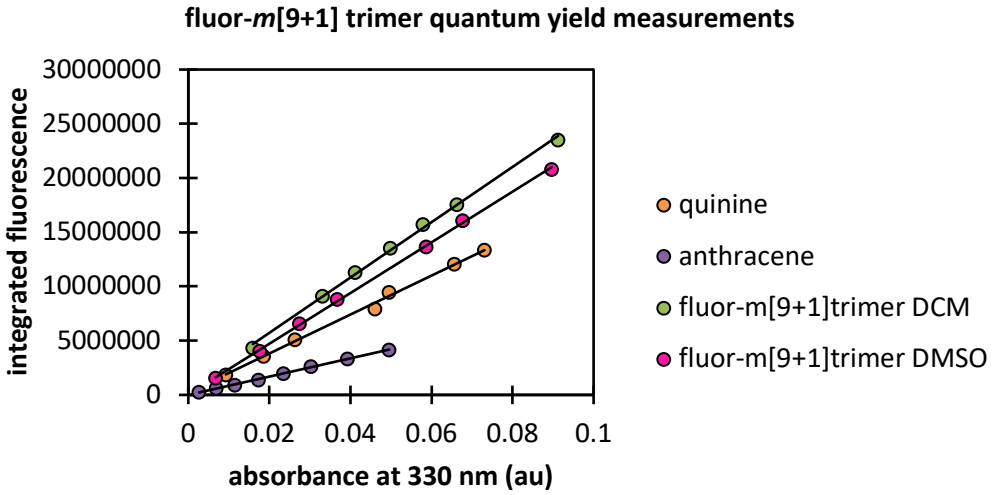

Figure S30. Quantum yield plot for **m-fluor[9+1]trimer**.

Table S6: Quantum yield data for **m-fluor[9+1]trimer**.

compound	**solvent**	**slope**	**Φ w.r.t. quinine**	**Φ w.r.t. anthracene**	**avg. Φ**	**std. dev.**
quinine	0.1 M H_2SO_4 (*aq*)	1.79 x 10^8	0.54 (lit)	0.55	0.55	0.008
anthracene	ethanol	8.43 x	0.26	0.27 (lit)	0.27	0.004

		10^7				
fluor-*m*[9+1] tri.	DCM	2.55 x 10^8	0.88	0.89	0.88	0.013
fluor-*m*[9+1] tri.	DMSO	2.34 x 10^8	0.87	0.88	0.88	0.013

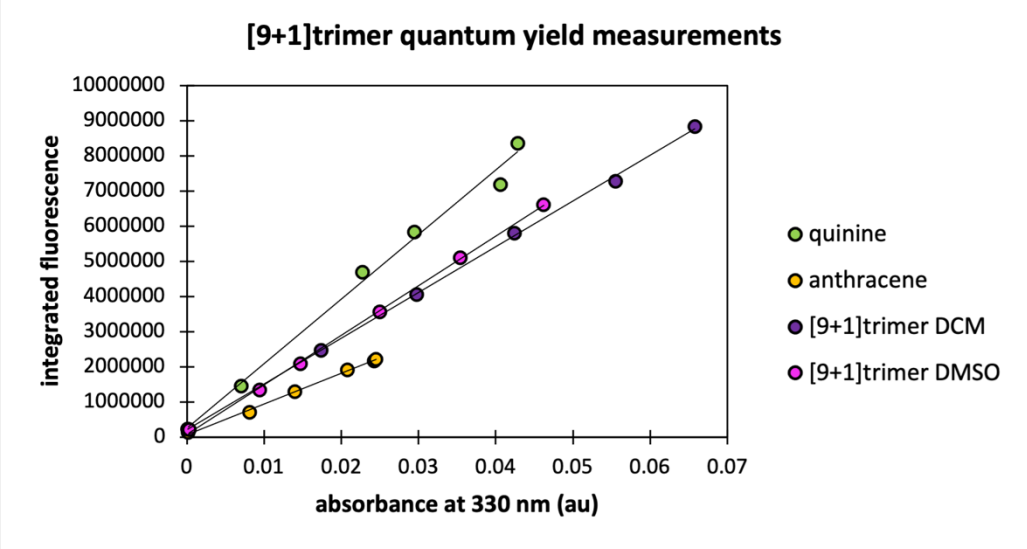

Figure S31. Quantum yield plot for **[9+1] trimer**.

Table S7: Quantum yield data for **[9+1] trimer**.

compound	**solvent**	**slope**	**Φ w.r.t. quinine**	**Φ w.r.t. anthracene**	**avg. Φ**	**std. dev.**
quinine	0.1 M H_2SO_4 (*aq*)	1.83 x 10^8	0.54 (lit)	0.56	0.55	0.008
anthracene	ethanol	8.72 x 10^7	0.26	0.27 (lit)	0.27	0.005

[9+1] trimer	DCM	1.30 x 10^8	0.41	0.42	0.42	0.005
[9+1] trimer	DMSO	1.41 x 10^8	0.46	0.48	0.47	0.008

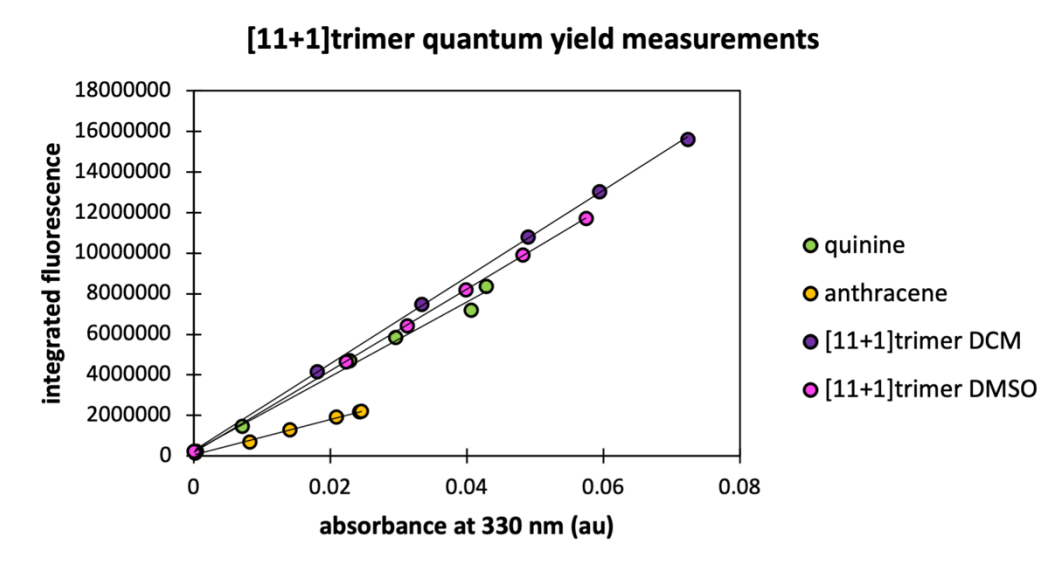

Figure S32. Quantum yield plot for **[11+1] trimer**.

Table S8: Quantum yield data for **[11+1] trimer**.

compound	**solvent**	**slope**	**Φ w.r.t. quinine**	**Φ w.r.t. anthracene**	**avg. Φ**	**std. dev.**
quinine	0.1 M H_2SO_4 (*aq*)	1.83 x 10^8	0.54 (lit)	0.56	0.55	0.008
anthracene	ethanol	8.72 x 10^7	0.26	0.27 (lit)	0.27	0.005
[11+1]	DCM	2.14 x	0.68	0.69	0.69	0.005

trimer		10^8				
[11+1] **trimer**	DMSO	2.01 x 10^8	0.66	0.68	0.67	0.008

Table S9: Calculated absorption transitions for **5**

No.	Energy (cm-1)	Wavelength (nm)	Osc. Strength	Symmetry	Major contribution
1	25186.27515	397.0416403	0.0053	Singlet-A	H-2->L+1 (22%), H-1->LUMO (26%), HOMO->L+2 (31%)
2	25247.57329	396.0776699	0.4858	Singlet-A	H-2->L+1 (11%), H-1->LUMO (10%), H-1->L+2 (29%), HOMO->LUMO (26%)
3	25254.02573	395.9764716	0.4859	Singlet-A	H-2->LUMO (12%), H-2->L+2 (31%), H-1->L+1 (10%), HOMO->L+1 (23%)
4	27891.45871	358.5327001	0.3709	Singlet-A	H-2->L+1 (12%), H-1->LUMO (14%), HOMO->LUMO (23%), HOMO->L+1 (22%)
5	27895.49148	358.480868	0.3652	Singlet-A	H-2->LUMO (13%), H-1->L+1 (14%), HOMO->LUMO (19%), HOMO->L+1 (22%)
6	27976.95348	357.43706	0.0024	Singlet-A	H-2->LUMO (38%), H-2->L+1 (10%), H-1->L+1 (36%)
7	28195.52973	354.6661508	0.0001	Singlet-A	H-2->L+1 (14%), H-1->LUMO (15%), HOMO->L+2 (64%)
8	28224.56569	354.3012888	0.0538	Singlet-A	H-2->L+1 (10%), H-2->L+2 (23%), H-1->L+2 (42%), HOMO->LUMO (14%)
9	28226.1788	354.2810407	0.0502	Singlet-A	H-2->L+2 (41%), H-1->L+2 (24%), HOMO->L+1 (13%)
10	28596.38728	349.6945227	1.6851	Singlet-A	H-1->L+5 (15%), HOMO->L+3 (34%)
11	28601.22661	349.6353544	1.7006	Singlet-A	H-2->L+4 (10%), H-2->L+5 (15%), H-1->L+3 (10%), HOMO->L+4 (30%)
12	28817.38319	347.0127712	0.0226	Singlet-A	H-2->L+4 (35%), H-1->L+3 (34%), HOMO->L+5 (17%)

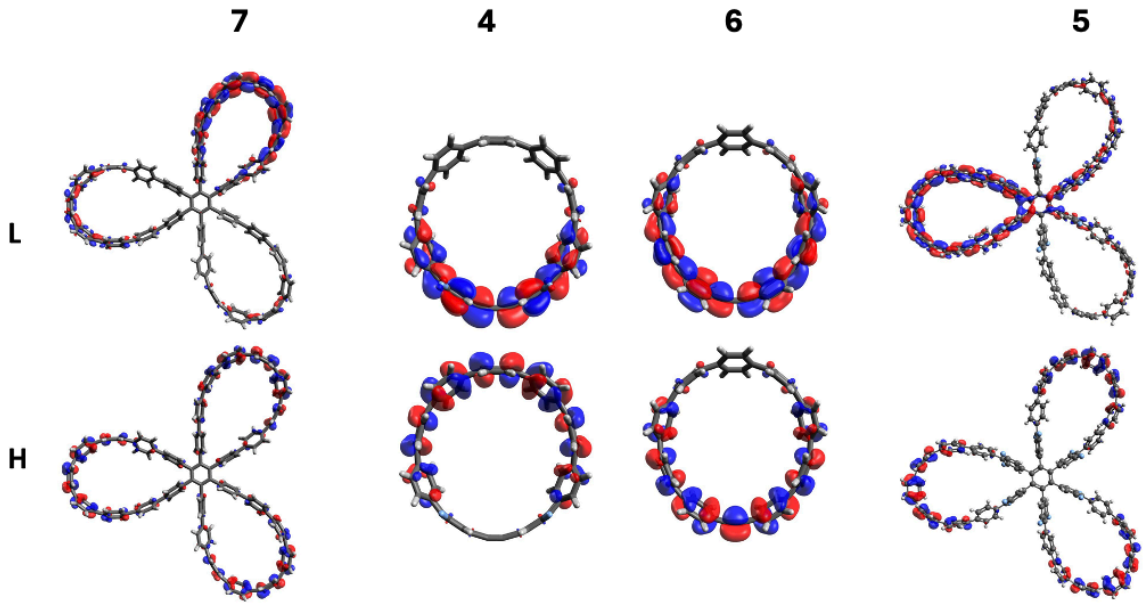

Figure S33. Calculated excited state orbital distribution of all hydrocarbon (6,7) and fluorinated (4,5) internal-alkyne CPPs and resulting trimers.

4.4.6. StrainViz calculations

All Gaussian output files for stationary points are available via Figshare with the following link, https://figshare.com/s/a9a9e03f19998b572ca7.

Computations were performed using Gaussian09[48] at the B3LYP/6-31G(d) level of theory. Keywords "Opt=(rfo,NoSymm)" were added to account for the fragments with an alkyne and to ensure minimal negative energies in the case of the trimer fragments. The alkyne piece was present in one fragment for the **fluor-*m*[9+1]CPP** StrainViz analysis because of the error associated with optimizing fragments with a 180° angle. Outputs from individual StrainViz calculations were submitted with the maximum bond energy set as the highest strained bond between all molecules (**fluor-*m*[9+1]CPP**) to generate a relative strain scale. This setting recolors each bond to generate a comparative heat map. Replacing the "max(norm_values)" on line 171 in the "bond_scripts.py" with the max bond strain in the "total_bond.tcl" file, a recolored output is generated by rerunning the StrainViz script for each molecule. All fragment geometries are available for download. See our previous publication[32] for fragment geometries of **[9+1]CPP**, **[11+1]CPP**, **[9+1] trimer**, and **[11+1] trimer**.

4.5 REFERENCES

(1) Scott, L. T.; Bronstein, H. E.; Preda, D. V.; Ansems, R. B. M.; Bratcher, M. S.; Hagen, S. Geodesic Polyarenes with Exposed Concave Surfaces. *Pure Appl Chem* **1999**, *71* (2), 209–219. https://doi.org/10.1351/pac199971020209.

(2) Bheemireddy, S. R.; Ubaldo, P. C.; Finke, A. D.; Wang, L.; Plunkett, K. N. Contorted Aromatics via a Palladium-Catalyzed Cyclopentannulation Strategy. *J Mater Chem C* **2016**, *4* (18), 3963–3969. https://doi.org/10.1039/C5TC02305J.

(3) Xu, Y.; Kaur, R.; Wang, B.; Minameyer, M. B.; Gsänger, S.; Meyer, B.; Drewello, T.; Guldi, D. M.; von Delius, M. Concave–Convex π–π Template Approach Enables the Synthesis of [10]Cycloparaphenylene–Fullerene [2]Rotaxanes. *J. Am. Chem. Soc.* **2018**, *140* (41), 13413–13420. https://doi.org/10.1021/jacs.8b08244.

(4) Ball, M.; Zhong, Y.; Fowler, B.; Zhang, B.; Li, P.; Etkin, G.; Paley, D. W.; Decatur, J.; Dalsania, A. K.; Li, H.; Xiao, S.; Ng, F.; Steigerwald, M. L.; Nuckolls, C. Macrocyclization in the Design of Organic N-Type Electronic Materials. *J. Am. Chem. Soc.* **2016**, *138* (39), 12861–12867. https://doi.org/10.1021/jacs.6b05474.

(5) Iijima, S. Helical Microtubules of Graphitic Carbon. *Nature* **1991**, *354* (6348), 56–58. https://doi.org/10.1038/354056a0.

(6) Kroto, H. W.; Heath, J. R.; O'Brien, S. C.; Curl, R. F.; Smalley, R. E. C60: Buckminsterfullerene. *Nature* **1985**, *318* (6042), 162–163. https://doi.org/10.1038/318162a0.

(7) Majewski, M. A.; Stępień, M. Bowls, Hoops, and Saddles: Synthetic Approaches to Curved Aromatic Molecules. *Angew. Chem. Int. Ed.* **2019**, *58* (1), 86–116. https://doi.org/10.1002/anie.201807004.

(8) Lewis, S. E. Cycloparaphenylenes and Related Nanohoops. *Chem. Soc. Rev.* **2015**, *44* (8), 2221–2304. https://doi.org/10.1039/C4CS00366G.

(9) Wu, D.; Cheng, W.; Ban, X.; Xia, J. Cycloparaphenylenes (CPPs): An Overview of Synthesis, Properties, and Potential Applications. *Asian J. Org. Chem.* **2018**, *7* (11), 2161–2181. https://doi.org/10.1002/ajoc.201800397.

(10) Yamago, S.; Kayahara, E. Synthesis and Reactions of Carbon Nanohoop. *J. Synth. Org. Chem. Jpn.* **2019**, *77* (11), 1147–1158. https://doi.org/10.5059/yukigoseikyokaishi.77.1147.

(11) Xu, Y.; von Delius, M. The Supramolecular Chemistry of Strained Carbon Nanohoops. *Angew. Chem. Int. Ed.* **2020**, *59* (2), 559–573. https://doi.org/10.1002/anie.201906069.

(12) Li, Y.; Kono, H.; Maekawa, T.; Segawa, Y.; Yagi, A.; Itami, K. Chemical Synthesis of Carbon Nanorings and Nanobelts. *Acc. Mater. Res.* **2021**, *2* (8), 681–691. https://doi.org/10.1021/accountsmr.1c00105.

(13) Hermann, M.; Wassy, D.; Esser, B. Conjugated Nanohoops Incorporating Donor, Acceptor, Hetero- or Polycyclic Aromatics. *Angew. Chem. Int. Ed.* **2021**, *60* (29), 15743–15766. https://doi.org/10.1002/anie.202007024.

(14) Jasti, R.; Bhattacharjee, J.; Neaton, J. B.; Bertozzi, C. R. Synthesis, Characterization, and Theory of [9]-, [12]-, and [18]Cycloparaphenylene: Carbon Nanohoop Structures. *J. Am. Chem. Soc.* **2008**, *130* (52), 17646–17647. https://doi.org/10.1021/ja807126u.

(15) Darzi, E. R.; Jasti, R. The Dynamic, Size-Dependent Properties of [5]–[12]Cycloparaphenylenes. *Chem. Soc. Rev.* **2015**, *44* (18), 6401–6410. https://doi.org/10.1039/C5CS00143A.

(16) Darzi, E. R.; Hirst, E. S.; Weber, C. D.; Zakharov, L. N.; Lonergan, M. C.; Jasti, R. Synthesis, Properties, and Design Principles of Donor–Acceptor Nanohoops. *ACS Cent. Sci.* **2015**, *1* (6), 335–342. https://doi.org/10.1021/acscentsci.5b00269.
(17) Van Raden, J. M.; Darzi, E. R.; Zakharov, L. N.; Jasti, R. Synthesis and Characterization of a Highly Strained Donor–Acceptor Nanohoop. *Org. Biomol. Chem.* **2016**, *14* (24), 5721–5727. https://doi.org/10.1039/C6OB00133E.
(18) Narita, N.; Kurita, Y.; Osakada, K.; Ide, T.; Kawai, H.; Tsuchido, Y. A Dodecamethoxy[6]Cycloparaphenylene Consisting Entirely of Hydroquinone Ethers: Unveiling in-Plane Aromaticity through a Rotaxane Structure. *Nat. Commun.* **2023**, *14* (1), 8091. https://doi.org/10.1038/s41467-023-43907-7.
(19) Leonhardt, E. J.; Jasti, R. Emerging Applications of Carbon Nanohoops. *Nat. Rev. Chem.* **2019**, *3* (12), 672–686. https://doi.org/10.1038/s41570-019-0140-0.
(20) Li, K.; Xu, Z.; Deng, H.; Zhou, Z.; Dang, Y.; Sun, Z. Dimeric Cycloparaphenylenes with a Rigid Aromatic Linker. *Angew. Chem. Int. Ed.* **2021**, *60* (14), 7649–7653. https://doi.org/10.1002/anie.202016995.
(21) Yang, Y.; Blacque, O.; Sato, S.; Juríček, M. Cycloparaphenylene–Phenalenyl Radical and Its Dimeric Double Nanohoop. *Angew. Chem. Int. Ed.* **2021**, *60* (24), 13529–13535. https://doi.org/10.1002/anie.202101792.
(22) May, J. H.; Fehr, J. M.; Lorenz, J. C.; Zakharov, L.; Jasti, R. A High-Yielding Active Template Click Reaction (AT-CuAAC) for the Synthesis of Mechanically Interlocked Nanohoops. *Angew. Chem. Int. Ed. n/a* (n/a), e202401823. https://doi.org/10.1002/anie.202401823.
(23) Zhao, C.; Meng, H.; Nie, M.; Wang, X.; Cai, Z.; Chen, T.; Wang, D.; Wang, C.; Wang, T. Supramolecular Complexes of C80-Based Metallofullerenes with [12]Cycloparaphenylene Nanoring and Altered Property in a Confined Space. *J. Phys. Chem. C* **2019**, *123* (19), 12514–12520. https://doi.org/10.1021/acs.jpcc.9b02451.
(24) Maust, R. L.; Li, P.; Shao, B.; Zeitler, S. M.; Sun, P. B.; Reid, H. W.; Zakharov, L. N.; Golder, M. R.; Jasti, R. Controlled Polymerization of Norbornene Cycloparaphenylenes Expands Carbon Nanomaterials Design Space. *ACS Cent. Sci.* **2021**, *7* (6), 1056–1065. https://doi.org/10.1021/acscentsci.1c00345.
(25) Kayahara, E.; Iwamoto, T.; Takaya, H.; Suzuki, T.; Fujitsuka, M.; Majima, T.; Yasuda, N.; Matsuyama, N.; Seki, S.; Yamago, S. Synthesis and Physical Properties of a Ball-like Three-Dimensional π-Conjugated Molecule. *Nat. Commun.* **2013**, *4* (1), 2694. https://doi.org/10.1038/ncomms3694.
(26) Hayase, N.; Nogami, J.; Shibata, Y.; Tanaka, K. Synthesis of a Strained Spherical Carbon Nanocage by Regioselective Alkyne Cyclotrimerization. *Angew. Chem. Int. Ed.* **2019**, *58* (28), 9439–9442. https://doi.org/10.1002/anie.201903422.
(27) Matsui, K.; Segawa, Y.; Namikawa, T.; Kamada, K.; Itami, K. Synthesis and Properties of All-Benzene Carbon Nanocages: A Junction Unit of Branched Carbon Nanotubes. *Chem. Sci.* **2012**, *4* (1), 84–88. https://doi.org/10.1039/C2SC21322B.
(28) Matsui, K.; Segawa, Y.; Itami, K. All-Benzene Carbon Nanocages: Size-Selective Synthesis, Photophysical Properties, and Crystal Structure. *J. Am. Chem. Soc.* **2014**, *136* (46), 16452–16458. https://doi.org/10.1021/ja509880v.
(29) Senthilkumar, K.; Kondratowicz, M.; Lis, T.; Chmielewski, P. J.; Cybińska, J.; Zafra, J. L.; Casado, J.; Vives, T.; Crassous, J.; Favereau, L.; Stępień, M. Lemniscular

[16]Cycloparaphenylene: A Radially Conjugated Figure-Eight Aromatic Molecule. *J. Am. Chem. Soc.* **2019**, *141* (18), 7421–7427. https://doi.org/10.1021/jacs.9b01797.
(30) Zhou, Q.; Xu, Z.; Li, K.; Tian, X.; Ye, L.; Sun, Z. Synthesis and Properties of a Strained Triple Nanohoop. *Chem. – Asian J.* **2024**, *19* (15), e202301131. https://doi.org/10.1002/asia.202301131.
(31) Schaub, T. A.; Margraf, J. T.; Zakharov, L.; Reuter, K.; Jasti, R. Strain-Promoted Reactivity of Alkyne-Containing Cycloparaphenylenes. *Angew. Chem. Int. Ed.* **2018**, *57* (50), 16348–16353. https://doi.org/10.1002/anie.201808611.
(32) Fehr, J. M.; Myrthil, N.; Garrison, A. L.; Price, T. W.; Lopez, S. A.; Jasti, R. Experimental and Theoretical Elucidation of SPAAC Kinetics for Strained Alkyne-Containing Cycloparaphenylenes. *Chem. Sci.* **2023**, *14* (11), 2839–2848. https://doi.org/10.1039/D2SC06816H.
(33) Schaub, T. A.; Zieleniewska, A.; Kaur, R.; Minameyer, M.; Yang, W.; Schüßlbauer, C. M.; Zhang, L.; Freiberger, M.; Zakharov, L. N.; Drewello, T.; Dral, P. O.; Guldi, D. M.; Jasti, R. Tunable Macrocyclic Polyparaphenylene Nanolassos via Copper-Free Click Chemistry. *Chem. – Eur. J.* **2023**, *29* (33), e202300668. https://doi.org/10.1002/chem.202300668.
(34) Reppe, W.; Schlichting, O.; Klager, K.; Toepel, T. Cyclisierende Polymerisation von Acetylen I Über Cyclooctatetraen. *Justus Liebigs Ann. Chem.* **1948**, *560* (1), 1–92. https://doi.org/10.1002/jlac.19485600102.
(35) Kotha, S.; Brahmachary, E.; Lahiri, K. Transition Metal Catalyzed [2+2+2] Cycloaddition and Application in Organic Synthesis. *Eur. J. Org. Chem.* **2005**, *2005* (22), 4741–4767. https://doi.org/10.1002/ejoc.200500411.
(36) Peña, D.; Escudero, S.; Pérez, D.; Guitián, E.; Castedo, L. Efficient Palladium-Catalyzed Cyclotrimerization of Arynes: Synthesis of Triphenylenes. *Angew. Chem. Int. Ed.* **1998**, *37* (19), 2659–2661. https://doi.org/10.1002/(SICI)1521-3773(19981016)37:19<2659::AID-ANIE2659>3.0.CO;2-4.
(37) Radhakrishnan, K. V.; Yoshikawa, E.; Yamamoto, Y. Palladium Catalyzed Co-Trimerization of Benzyne with Alkynes. A Facile Method for the Synthesis of Phenanthrene Derivatives. *Tetrahedron Lett.* **1999**, *40* (42), 7533–7535. https://doi.org/10.1016/S0040-4039(99)01526-9.
(38) Peña, D.; Pérez, D.; Guitián, E. Cyclotrimerization Reactions of Arynes and Strained Cycloalkynes. *Chem. Rec.* **2007**, *7* (6), 326–333. https://doi.org/10.1002/tcr.20132.
(39) Vij, V.; Bhalla, V.; Kumar, M. Hexaarylbenzene: Evolution of Properties and Applications of Multitalented Scaffold. *Chem. Rev.* **2016**, *116* (16), 9565–9627. https://doi.org/10.1021/acs.chemrev.6b00144.
(40) Tanaka, K. Rhodium-Mediated [2 + 2 + 2] Cycloaddition. In *Transition-Metal-Mediated Aromatic Ring Construction*; John Wiley & Sons, Ltd, 2013; pp 127–160. https://doi.org/10.1002/9781118629871.ch4.
(41) Pla-Quintana, A.; Roglans, A. The Choice of Rhodium Catalysts in [2+2+2] Cycloaddition Reaction: A Personal Account. *Molecules* **2022**, *27* (4), 1332. https://doi.org/10.3390/molecules27041332.
(42) Kumar, P.; Louie, J. Nickel-Mediated [2 + 2 + 2] Cycloaddition. In *Transition-Metal-Mediated Aromatic Ring Construction*; John Wiley & Sons, Ltd, 2013; pp 37–70. https://doi.org/10.1002/9781118629871.ch2.

(43) Stará, I. G.; Starý, I.; Kollárovič, A.; Teplý, F.; Vyskočil, Š.; Šaman, D. Transition Metal Catalysed Synthesis of Tetrahydro Derivatives of [5]-, [6]- and [7]Helicene. *Tetrahedron Lett.* **1999**, *40* (10), 1993–1996. https://doi.org/10.1016/S0040-4039(99)00099-4.
(44) Teplý, F.; Stará, I. G.; Starý, I.; Kollárovič, A.; Šaman, D.; Rulíšek, L.; Fiedler, P. Synthesis of [5]-, [6]-, and [7]Helicene via Ni(0)- or Co(I)-Catalyzed Isomerization of Aromatic Cis,Cis-Dienetriynes. *J. Am. Chem. Soc.* **2002**, *124* (31), 9175–9180. https://doi.org/10.1021/ja0259584.
(45) Kotha, S.; Brahmachary, E.; Lahiri, K. Transition Metal Catalyzed [2+2+2] Cycloaddition and Application in Organic Synthesis. *Eur. J. Org. Chem.* **2005**, *2005* (22), 4741–4767. https://doi.org/10.1002/ejoc.200500411.
(46) Bennett, M. A.; Schwemlein, H. P. Metal Complexes of Small Cycloalkynes and Arynes. *Angew. Chem. Int. Ed. Engl.* **1989**, *28* (10), 1296–1320. https://doi.org/10.1002/anie.198912961.
(47) Colwell, C. E.; Price, T. W.; Stauch, T.; Jasti, R. Strain Visualization for Strained Macrocycles. *Chem. Sci.* **2020**, *11* (15), 3923–3930. https://doi.org/10.1039/D0SC00629G.
(48) *Gaussian 09 Citation | Gaussian.com*. https://gaussian.com/g09citation/ (accessed 2022-10-28).
(49) Adamska, L.; Nayyar, I.; Chen, H.; Swan, A. K.; Oldani, N.; Fernandez-Alberti, S.; Golder, M. R.; Jasti, R.; Doorn, S. K.; Tretiak, S. Self-Trapping of Excitons, Violation of Condon Approximation, and Efficient Fluorescence in Conjugated Cycloparaphenylenes. *Nano Lett.* **2014**, *14* (11), 6539–6546. https://doi.org/10.1021/nl503133e.
(50) Leonhardt, E. J.; Van Raden, J. M.; Miller, D.; Zakharov, L. N.; Alemán, B.; Jasti, R. A Bottom-Up Approach to Solution-Processed, Atomically Precise Graphitic Cylinders on Graphite. *Nano Lett.* **2018**, *18* (12), 7991–7997. https://doi.org/10.1021/acs.nanolett.8b03979.
(51) Van Raden, J. M.; Leonhardt, E. J.; Zakharov, L. N.; Pérez-Guardiola, A.; Pérez-Jiménez, A. J.; Marshall, C. R.; Brozek, C. K.; Sancho-García, J. C.; Jasti, R. Precision Nanotube Mimics via Self-Assembly of Programmed Carbon Nanohoops. *J. Org. Chem.* **2020**, *85* (1), 129–141. https://doi.org/10.1021/acs.joc.9b02340.
(52) Lovell, T. C.; Colwell, C. E.; Zakharov, L. N.; Jasti, R. Symmetry Breaking and the Turn-on Fluorescence of Small, Highly Strained Carbon Nanohoops. *Chem. Sci.* **2019**, *10* (13), 3786–3790. https://doi.org/10.1039/C9SC00169G.
(53) Chen, D.; Wada, Y.; Kusakabe, Y.; Sun, L.; Kayahara, E.; Suzuki, K.; Tanaka, H.; Yamago, S.; Kaji, H.; Zysman-Colman, E. A Donor–Acceptor 10-Cycloparaphenylene and Its Use as an Emitter in an Organic Light-Emitting Diode. *Org. Lett.* **2023**, *25* (6), 998–1002. https://doi.org/10.1021/acs.orglett.3c00127.
(54) Kuwabara, T.; Orii, J.; Segawa, Y.; Itami, K. Curved Oligophenylenes as Donors in Shape-Persistent Donor–Acceptor Macrocycles with Solvatofluorochromic Properties. *Angew. Chem. Int. Ed.* **2015**, *54* (33), 9646–9649. https://doi.org/10.1002/anie.201503397.
(55) Lovell, T. C.; Garrison, Z. R.; Jasti, R. Synthesis, Characterization, and Computational Investigation of Bright Orange-Emitting Benzothiadiazole [10]Cycloparaphenylene. *Angew. Chem. Int. Ed.* **2020**, *59* (34), 14363–14367. https://doi.org/10.1002/anie.202006350.
(56) Pedersen, V. B. R.; Price, T. W.; Kofod, N.; Zakharov, L. N.; Laursen, B. W.; Jasti, R.; Brøndsted Nielsen, M. Synthesis and Properties of Fluorenone-Containing

Cycloparaphenylenes and Their Late-Stage Transformation. *Chem. – Eur. J.* **2024**, *30* (5), e202303490. https://doi.org/10.1002/chem.202303490.
(57) Barnsley, J. E.; Shillito, G. E.; Mapley, J. I.; Larsen, C. B.; Lucas, N. T.; Gordon, K. C. Walking the Emission Tightrope: Spectral and Computational Analysis of Some Dual-Emitting Benzothiadiazole Donor–Acceptor Dyes. *J. Phys. Chem. A* **2018**, *122* (40), 7991–8006. https://doi.org/10.1021/acs.jpca.8b05361.
(58) Caspar, J. V.; Meyer, T. J. Application of the Energy Gap Law to Nonradiative, Excited-State Decay. *J. Phys. Chem.* **1983**, *87* (6), 952–957. https://doi.org/10.1021/j100229a010.
(59) Bruno, N. C.; Tudge, M. T.; Buchwald, S. L. Design and Preparation of New Palladium Precatalysts for C–C and C–N Cross-Coupling Reactions. *Chem. Sci.* **2013**, *4* (3), 916–920. https://doi.org/10.1039/C2SC20903A.
(60) Pangborn, A. B.; Giardello, M. A.; Grubbs, R. H.; Rosen, R. K.; Timmers, F. J. Safe and Convenient Procedure for Solvent Purification. *Organometallics* **1996**, *15* (5), 1518–1520. https://doi.org/10.1021/om9503712.
(61) Horiba, J. Y. A Guide to Recording Fluorescence Quantum Yields. https://static.horiba.com/fileadmin/Horiba/Application/Materials/Material_Research/Quantum_Dots/quantumyieldstrad.pdf (accessed 2022-10-28).

CHAPTER V

CONCLUDING REMARKS

The chemistry of non-planar carbon nanomaterials is a rapidly growing and highly interdisciplinary field. Molecules and materials in this family show promise for a diverse range of applications. To better investigate desirable properties such as tunable optical, electronic, and supramolecular capabilities, we need to overcome limitations in current synthetic methodology. The work presented in this dissertation builds upon classic, versatile, and well-studied reactions that have been used to transform linear aromatic systems but have not been investigated as strain-amenable late-stage transformations on the CPP scaffold. We anticipate that this research will help inform suitable transformations of curved nanomaterials and diversify the types of nanoarchitectures available.